



**Università
degli Studi
di Ferrara**

**DOCTORAL COURSE IN
CHEMICAL SCIENCES**

CYCLE XXXII

DIRECTOR Prof. Alberto Cavazzini

**NANOTECHNOLOGICAL STRATEGIES
FOR TOPICAL ADMINISTRATION OF
ACTIVE COMPOUNDS**

Scientific/Disciplinary Sector (SDS) CHIM/09

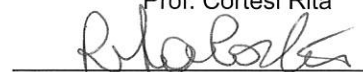
Candidate

Dott. Sguizzato Maddalena


(signature)

Supervisor

Prof. Cortesi Rita


(signature)

Years 2016/2019

CONTENTS

1. INTRODUCTION	1
1.1. SKIN STRUCTURE AND FUNCTIONS	1
1.1.1. The epidermis	2
1.1.2. The dermis	3
1.1.3. The hypodermis	3
1.1.4. The appendages	3
1.1.5. The mucosa	4
1.2. ROUTES OF SKIN PENETRATION	4
1.3. TOPICAL ADMINISTRATION OF DRUGS	6
1.4. LIPID-BASED DELIVERY SYSTEMS	8
1.4.1. Lipospheres	9
1.4.2. Solid Lipid Nanoparticles (SLN) and Nanostructured Lipid Carriers (NLC)	10
1.4.3. Ethosomes	12
1.5. GELS	13
1.5.1. Poloxamer gels	14
1.6. AIMS AND ORGANIZATION OF THE THESIS	16
2. MATERIALS	18
3. METHODS	19
3.1. NANOSYSTEMS PRODUCTION	19
3.1.1. Liposphere Production	19
3.1.2. Lipid Nanoparticles	19
- Ultrasound homogenization (UH) method	20
- High pressure homogenization (HPH) method	20
3.1.3. Ethosomes production	20
3.1.4. Gels production	20
- Xanthan gum gel production	20
- Hyaluronic Acid gel production	21
- Poloxamer gel production	21
- Production of viscous LN dispersions	21
3.2. NANOSYSTEMS CHARACTERIZATION	22
3.2.1. Variable-pressure scanning electron microscopy (VPSEM)	22
3.2.2. Photon correlation spectroscopy (PCS)	22
3.2.3. Cryogenic Transmission Electron Microscopy (Cryo-TEM)	22
3.2.4. X-ray diffraction measurements	23

3.2.5.	Small-angle X-ray scattering (SAXS) measurements	23
3.2.6.	Fourier Transform Infrared (FTIR) Spectroscopic Analysis	24
3.2.7.	Viscosity test	24
3.2.8.	Rheological measurements	24
3.2.9.	Spreadability studies	25
3.2.10.	Gel leakage and adhesion test	25
3.3.	DRUG CONTENT	26
3.3.1.	Encapsulation efficiency (EE) and loading capacity (LC)	26
3.3.2.	Prediction of Long-Term Stability	27
3.3.3.	High performance liquid chromatography (HPLC) analysis	27
3.4.	<i>IN VITRO</i> TECHNOLOGICAL STUDIES	29
3.4.1.	<i>In vitro</i> release studies	29
3.4.2.	<i>In vitro</i> diffusion studies	30
3.5.	<i>IN VITRO</i> BIOLOGICAL STUDIES	31
3.5.1.	Anticandidal activity study	31
3.5.2.	Cell culture and treatments	32
3.5.3.	Cytotoxicity studies	33
-	LDH assay	33
-	MTT assay	33
-	Trypan blue exclusion assay	34
3.5.4.	Wound healing assay	34
3.5.5.	Transmission electron microscopy (TEM)	34
3.5.6.	Immunocytochemistry	34
3.5.7.	Cell migration assay	35
3.6.	<i>EX-VIVO</i> TESTS	36
3.6.1.	Human skin explants (HSE) culture	36
3.6.2.	Cigarette smoke (CS) exposure	36
3.6.3.	Protein extraction	36
3.6.4.	Western blot analysis	36
3.7.	<i>IN VIVO</i> TESTS	37
3.7.1.	Tape stripping	37
3.7.2.	<i>In vivo</i> skin adhesion study	38
4.	PRODUCTION AND CHARACTERIZATION OF A CLOTRIMAZOLE LIPOSPHERE GEL FOR CANDIDIASIS TREATMENT	39
4.1.	INTRODUCTION	39
4.2.	RESULTS AND DISCUSSION	41
4.2.1.	Liposphere production and characterization	41
4.2.2.	Anticandidal activity study	44
4.2.3.	Production and characterization of Liposphere Gels	45
i)	Gel Viscosity	46
ii)	Gel Spreadability	46
iii)	Gel Leakage	47

iv) Gel Adhesion	49
4.2.4. <i>In Vitro</i> CLO Release Kinetics	50
5. PROGESTERONE LIPID NANOPARTICLES: SCALING UP AND <i>IN VIVO</i> HUMAN STUDY	52
5.1. INTRODUCTION	52
5.2. RESULTS AND DISCUSSION	54
5.2.1. Effect of experimental set up on lipid nanoparticles	54
5.2.2. Nanoparticles characterization	56
5.2.3. Morphological analyses of lipid nanoparticles	57
5.2.4. Stability studies	59
5.2.5. <i>In vitro</i> PRG release kinetics	61
5.2.6. <i>In vitro</i> skin permeability of nanoparticles	62
5.2.7. Tape-stripping experiments	63
6. PRODUCTION AND CHARACTERIZATION OF NANOPARTICLE BASED HYALURONATE GEL CONTAINING RETINYL PALMITATE FOR WOUND HEALING	66
6.1. INTRODUCTION	66
6.2. RESULTS AND DISCUSSION	68
6.2.1. Preparation and characterization of lipid nanoparticles	68
6.2.2. Preparation and characterization of nanoparticulate gel	72
6.2.3. RP Diffusion Study	75
6.2.4. Cytotoxicity	76
6.2.5. Wound healing assay	77
7. LIPID NANOSTRUCTURES FOR α-TOCOPHEROL DELIVERY: A PREFORMULATION STUDY	79
7.1. INTRODUCTION	79
7.2. RESULTS AND DISCUSSION	82
7.2.1. Effect of lipid composition on nanoparticle macrostructure	82
7.2.2. Effect of lipid composition on size distribution of nanoparticles	83
7.2.3. Production and characterization of NLC containing TOC	86
7.2.4. Encapsulation of TOC in NLC	89
7.2.5. Cytotoxicity of NLC containing TOC	90
7.2.6. Antioxidant effect of NLC containing TOC	91
8. LIPID BASED NANOPARTICLES FOR THE DELIVERY OF UBIQUINONE	94
8.1. INTRODUCTION	94
8.2. RESULTS AND DISCUSSION	96
8.2.1. Preparation and characterization of lipid nanoparticles containing Ub-O	96

8.2.2.	Encapsulation of Ub-O in NLC	97
8.2.3.	Cytotoxicity of NLC containing Ub-O	98
8.2.4.	Preparation and characterization of ethosomes	101
8.2.5.	Encapsulation of Ub-O in ETHO	103
8.2.6.	Cytotoxicity of ETHO containing Ub-O	103
8.2.7.	ETHO uptake in fibroblasts detected by TEM	105
8.2.8.	Evaluation of 4HNE protein adducts levels in fibroblasts treated with ETHO Ub-O by Immunocytochemistry analysis	106
9. GALLIC ACID LOADED POLOXAMER GELS AS A NEW ADJUVANT STRATEGY FOR MELANOMA: A PRELIMINARY STUDY		109
9.1.	INTRODUCTION	109
9.2.	RESULTS AND DISCUSSION	111
9.2.1.	Gel preparation and characterization	111
i)	Rheological study	112
ii)	Spreadability study	114
9.2.2	GA stability in poloxamer gels	115
9.2.3	<i>In vitro</i> GA diffusion kinetics	115
i)	Selection of membrane system	115
ii)	Study of GA diffusion from gels	119
9.2.4	Biological activity studies	122
i)	MTT assay	122
ii)	Wound healing assay	122
iii)	Migration assay	124
10. POLOXAMER-HYALURONIC ACID BASED GELS FOR THE DELIVERY OF CAFFEIC ACID		126
10.1.	INTRODUCTION	126
10.2.	RESULTS AND DISCUSSION	128
10.2.1.	Gel preparation and characterization	128
10.2.2.	Rheological study	129
10.2.3.	Spreadability study	130
10.2.4.	Skin Adhesion study	131
10.2.5.	<i>In vitro</i> CA diffusion kinetics	132
10.2.6.	Cytotoxicity study	133
11. CONCLUSIONS		135
12. BIBLIOGRAPHY		139

1. INTRODUCTION

1.1. SKIN STRUCTURE AND FUNCTIONS

The skin is the largest organ in the human body, both in weight and in surface area, acting as a defense barrier against outdoor environment (Esposito et al., 2019). Hence, as a barrier organ, skin is exposed to different external factors, that contribute to skin aging, such as radiations (ultraviolet radiation, visible light and infrared radiation), air pollution, cigarette smoke, nutrition and other miscellaneous factors (stress and sleep deprivation) (Krutmann et al., 2017). Besides this protective effect, skin safeguards the internal organs and it performs many varied functions, such as stabilization of blood pressure and temperature, water retention and mediation of sensations of heat, cold, touch and pain.

The human skin is a stratified structure comprised of three main layers, as shown in *Figure 1*: (i) the superficial part, the epidermis, (ii) the connective tissue, the dermis and (iii) the subcutaneous fat, the hypodermis (Kim et al., 2016). Furthermore, the appendages (e.g., hair follicles, apocrine and eccrine glands) can offer a potential route for drug delivery, despite the relatively small area that they occupy. The human body is also composed of mucosal barrier, which provides protection against immunological, chemical and mechanical stresses in specific districts (Iqbal and Dilnawaz, 2019).

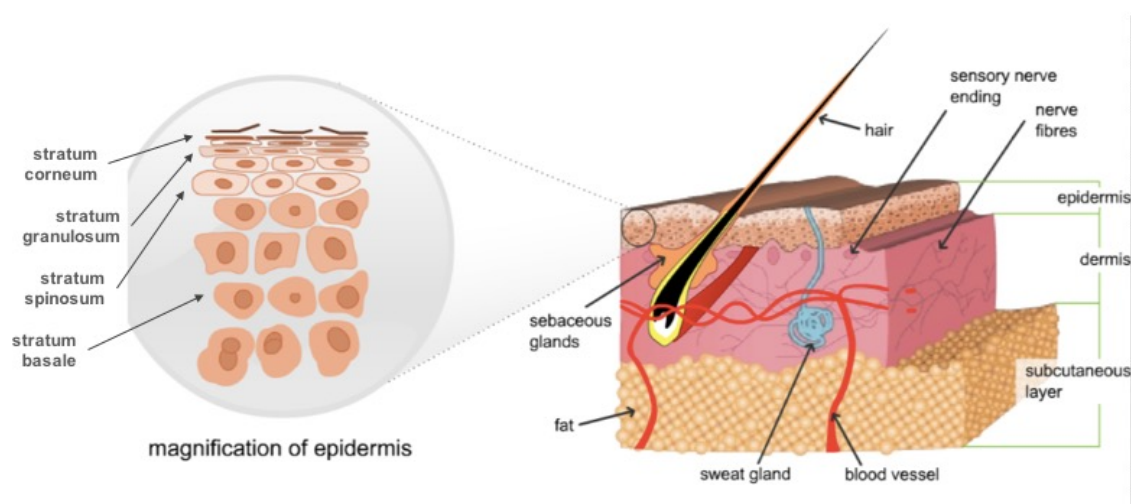


Figure 1: Schematic representation of the different skin layers (Geerligs, 2006)

1.1.1. The epidermis

The epidermis is the outermost layer of the skin, it is approximately 75-150 μm in thickness and can be divided into four different layers: stratum corneum (SC), stratum granulosum (SG), stratum spinosum (SS), and stratum basale (SB). The formation of this layered structure is due to the presence of many cells types including keratinocytes, melanocytes and Langerhans cells.

The stratum corneum is the outmost epidermal layer and, thanks to its functional features, it is predominantly responsible of the protective effect exerted by epidermis. SC is composed of physically dead keratinocytes called corneocytes, held together by a protein matrix (e.g., keratin) coated with a layer of lipids (e.g., ceramides, fatty acids and cholesterol). This “brick and mortar” structure, where the corneocytes act as the brick and the layered lipids as a mortar, gives rise to the rigidity and barrier function of SC and it limits substance passage into and through the skin (Palmer and DeLouise, 2016).

The stratum granulosum consists of granular cells containing keratohyalin granules generating a highly hydrophobic layer binding SC, that is on the contrary impermeable to hydrophilic drugs and molecules over 500kDa.

By deeper proceeding, the stratum spinosum presents the keratinocytes differentiated, that generate eight to ten layers, and they begin the synthesis of keratin. Moreover, in SS dendritic cells named Langerhans cells act as a macrophage by phagocytizing bacteria, foreign particles and damaged cells that pass through this layer.

The lowermost epidermal layer called stratum basale is characterized by proliferative keratinocytes. This type of cells generates the upper layers described by differentiating and migrating outwards, while melanocytes, also present in SB, have the function of producing melanin, a pigment responsible of the skin protection from solar radiation.

The epidermis, being an epithelial tissue, is not vascularized and receives nutrients through diffusion. Hence, the metabolic activity as well as the thermoregulation and the delivery of oxygen and nutrients, is given by the dermis, composed of blood and lymphatic vessels (Palmer and DeLouise, 2016).

1.1.2. The dermis

The dermis is the major component of the skin, being 1-4 mm in thickness and mainly consisting of connective tissue composed of fibrous proteins, namely collagen and elastin, embedded in a mucopolysaccharide gel. Collagen and elastin are secreted by fibroblasts, that are the main type of cells formed in this layer. It also contains the appendages, such as eccrine and apocrine sweat glands, hair follicles and nerve fibers. The blood and lymphatic vessels create an extensive vasculature in the dermis, which being metabolically active, is able to control the regulation of body temperature and the wound repair, to deliver oxygen and nutrients to the tissue and to remove waste products (Aulton and Taylor, 2018). The blood supply reaches the dermis-epidermis limit, thus the topically applied drugs, capable to pass through the SC epidermal barrier, rapidly diffuse into the systemic circulation.

1.1.3. The hypodermis

The hypodermis, or subcutaneous fat, is the lowermost layer of the skin, typically several millimeters thick over the myofascia, and it consists of adipose tissue.

The adipocytes are the main cells in the adipose tissue, which are held in a framework of collagen fibers. They provide a storage of high-energy molecules, mechanical protection against physical shock and thermal insulation, which depends on the thickness of the fat layer. The hypodermis is also highly vascularized and nourished, carrying the main blood vessels and nerves to the skin (Geerligs, 2006).

1.1.4. The appendages

The skin appendages are embedded in the dermis and, crossing the whole skin with a heterogeneous distribution, they can provide an easy access for the molecules into the systemic circulation (Carter et al., 2019).

The eccrine glands are distributed over most of the body surface and they are involved in sweat secretion, when the body is exposed to heat or emotional stress. The apocrine glands, however, are much less numerous than eccrine glands and they are found at specific body sites, as the axillae.

The hair follicles are the largest appendages of the skin and one of their function is to secrete sebum by sebaceous glands. Both sweat and sebum have a pH around 5, but the sweat is a dilute salt solution responsible of thermoregulation, while the sebum is composed of fatty acid, waxes and tryglicerides (Aulton and Taylor, 2018). Moreover, the sebum on the skin surface is usually emulsified with the aqueous solution coming from sweat, and the resulting emulsion coats the skin surface. These secondary structures can be exploited for transdermal drug delivery, working in a distinguishing skin penetration pathway, namely follicular route.

1.1.5. The mucosa

The mucosa is a non-keratinized epithelium covering the surface of different organs. Particularly, it possesses different anatomical and physiological properties depending on the system involved, namely gastrointestinal, respiratory, urinary, genital, ocular (Elsner, 2011).

The mucous membranes are characterized by a multilayered structure completely coated by an aqueous dispersion of proteins, such as mucin, namely mucous.

The mucosae close to the skin, being highly hydrated, are more permeable to exogenous substances and they present a different reactivity compared to the adjacent keratinized epithelium.

Thanks to this composition, the mucosal surface gives rise to an alternative approach for both local and systemic drug delivery.

1.2. ROUTES OF SKIN PENETRATION

The delivery of a drug molecule into the systemic circulation when topically applied is a complex process. The different layers of the human skin represent a series of barriers to a molecule traversing the tissue. For this reason, there are different pathways for skin penetration, graphically represented in *Figure 2*: (i) *intercellular* route, (ii) *intracellular* or *transcellular* route and (iii) *follicular* route.

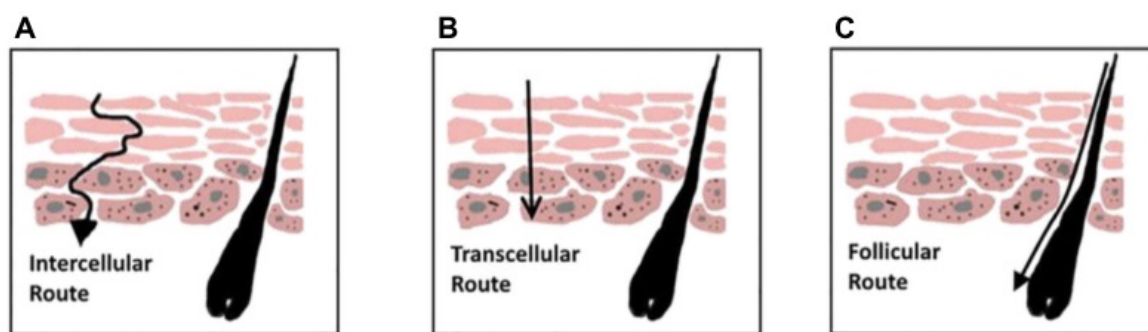


Figure 2: The pathways for percutaneous absorption of drugs: intercellular route (A), transcellular route (B) and follicular route (C) (Carter et al., 2019)

The drug delivery through the *intercellular* route involves the extracellular matrix between the corneocytes. According to the arrangement of these cells in SC, the diffusion of the molecules proceeds in a tortuous route, following the mortar in the “brick wall” structure (Figure 2 A). The lipid head of the molecules enables the penetration through the lipid fraction (Carter et al., 2019). The limiting factor of this route is the extracellular matrix acting as hydrophobic barrier. According to its nature, a strong lipophilic molecule easily pass through the SC, but its penetration into the hydrophilic portion of the skin is crucial. Hence, this is the typical route for lipophilic or amphiphilic molecules.

The second transport pathway is the *transcellular* route, where the molecules pass through the skin barrier crossing the corneocytes (Figure 2 B). During its travel, the molecule need to pass through alternate hydrophilic and hydrophobic regions, thus the partition of the drug between these areas could lead to the accumulation of the drug within corneocytes before reaching the deepest layers.

The last potential pathway of transport is the *follicular* route, exploiting the appendages of the skin (Figure 2 C). Since these dermal structures of the skin have polar characteristics, this is the usual route for the hydrophilic drugs. Nevertheless, the follicular orifice area on the skin surface is only about 0.1% of the total surface area, thus the percutaneous absorption with this pathway depends on the difference in density of follicles in various parts of the body (Zhou et al., 2018).

Furthermore, in this route, the systemic circulation can be provided thanks to the proximity of these organs to the capillary vessels and their capability to act as a reservoir into the skin, promoting the controlled release of the drug.

Even if the molecules can cross the skin through the three different ways above described, it should be noticed that these three routes operate for any sort of

permeant, and their physicochemical properties are responsible of the proportion of molecules involved in each pathway (Aulton and Taylor, 2018).

1.3. TOPICAL ADMINISTRATION OF DRUGS

The skin is an important site for absorption of numerous molecules where they may exert their efficacy or pass through reaching the blood stream. The topical administration of drugs is indeed an attractive way for the treatment of many diseases, being favorable to treat both local and systemic pathologies. Actually, after application of a formulation to the skin, dermal drug delivery could be involved to treat a local disorder in a specific area of interest or to reach the underlying tissue. Furthermore, transdermal formulations could deliver a drug across the skin layers for systemic therapeutic action, when not just skin illness are involved (Aulton and Taylor, 2018).

The most common oral and parenteral administration routes could have a limited interest for the treatment of many skin disorders, because of the low drug amount in the skin tissue or the generation of severe systemic side effects. Compared to these traditional administration routes, the topical one possesses many advantages (Esposito et al., 2019), such as:

- Increased patient compliance
- Avoidance of first-pass effect metabolism
- Decreased drug side effects
- Reduction of fluctuations of drug plasma levels after repeated administrations
- Faster clinical effect
- Direct dispensing on the site of action
- Non-invasive application

The efficacy of topical delivery depends on multiple factors. Above all, delivery is controlled by the presence of multiple biological barriers (or skin layers), which exert a protective function against the outside environment and selectively limit the absorption of active substances. The SC of epidermis is the first barrier of the body to cross in order to enable the penetration of active compounds. Its hydrophobic nature limits the types of molecules that can enter into the skin, promoting the penetration of lipid soluble compounds, as compared to the water-soluble ones.

Furthermore, the skin age and metabolism, the type of application modality, the composition of vehicle and the possibility of local irritation could interfere with absorption of the actives and the effectiveness of this administration route (Alexander et al., 2012).

With the aim of overcoming these limitations, several strategies were tested over the last years. As mentioned above, the SC of the skin is the most critical barrier for the permeation of molecules and chemical and physical methods have been designed respectively to increase the skin permeability or to generate a driving force imposing the drug passage. In the first case, the use of penetration enhancers, such as dimethylsulphoxyde, is involved, while high-voltage electrical pulsing, iontophoresis, electroporation, ultrasounds are exploited to disrupt the corneal layer (Esposito et al., 2019; Sala et al., 2018).

Besides the efficiency of these types of approaches, it should be noted that these advanced methods could be invasive and lead to skin irritation and pain.

The conventional topical preparations, such as ointments, creams, gels, oils, pastes, are often unspecific and intended for a local rather than a systemic action. Moreover, the delivery efficiency and therapeutic effect of the active mainly depend on drug diffusion and interaction between the formulation excipients and membrane components.

In order to avoid these issues, the dermal and transdermal drug delivery could be enhanced by some formulation strategies, such as the encapsulation of the active compounds into specific drug delivery systems which appear very promising to overcome the skin barrier. In this view, during the last decades, considerable attention has been focused on the development of novel carriers characterized by micro and nano dimensions, aimed to obtained sustained release and to shield the substances from degradation (Gupta et al., 2012). Numerous advantages have been achieved with the development of these new delivery technologies; among them the main is the targeted drug delivery to the site of disease. As far as skin targeting is concerned, the selected drug delivery systems allow to reach the site of action or deeper layers, also in view of systemic effect.

As shown in *Figure 3*, several novel drug delivery systems have been widely explored, differing in composition, formulation method and drug loading. Focusing on the topical administration route, the interaction of these systems with the skin and the subsequent crossing of the loaded drug through the skin layers, represent a crucial point still under investigation and the use of biocompatible materials in the

formulation offer interesting features. Particularly, lipid-based delivery systems due to their complete biodegradability, low toxicity and easy manufacturing handling, promote the dermal and transdermal drug delivery.

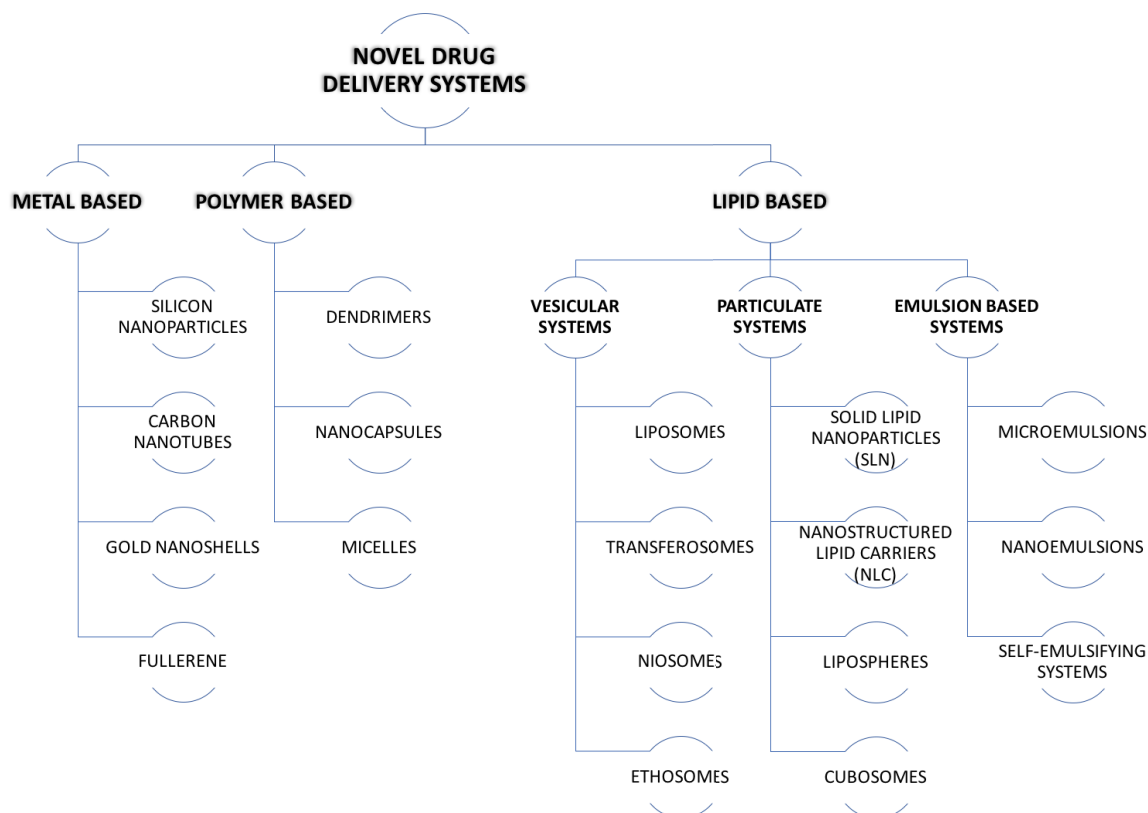


Figure 3: Overview of novel drug delivery systems

1.4. LIPID-BASED DELIVERY SYSTEMS

The structural similarities of lipids composing epidermis and in particular SC, with those of lipid-based delivery systems (LBDS) make these latter promising tools for topical administration of drugs. Thanks to this peculiarity and their biocompatibility, LBDS enable the skin penetration and achieve drug targeting by different mechanisms. Moreover, they might adhere to the skin surface and consequently increase skin hydration leading to looseness of the structure, fluidization, lipid exchange within the intercellular domain and polarity alteration (Sala et al., 2018). As mentioned above, many types of lipid-based systems can be produced modifying either their constituents and production method. Indeed, different particulate and vesicular lipid systems have been investigated in this doctorate project.

1.4.1. Lipospheres

Lipid microspheres, commonly called lipospheres (LS), represent a new type of lipid-based encapsulation system of drug delivery, developed to overcome the drawbacks associated with polymeric microparticles or liposomes. They are solid microparticles with a mean diameter comprised between 0.2 and 500 μm , composed of a solid hydrophobic fat matrix, where the bioactive compound(s) is dissolved or dispersed (*Figure 4*) (Cortesi et al., 2002). The common lipid compounds used to establish the lipid core are triglycerides, monoglycerides or fatty acid derivatives, which increase the entrapment and bioavailability of poorly water-soluble drugs.

Lipospheres offer well controlled delivery to a variety of drug candidates, thanks to their several advantages. They are characterized by good physical stability, biocompatible and non-toxic components, controlled particle size, high drug load and ease of preparation and scaling-up. Moreover, they promote the protection of both hydrophilic and hydrophobic molecules from degradation and hydrolysis, and they improve their bioavailability and shelf life (Yalavarthi et al., 2014).

The methods employed to produce lipospheres are based on melt dispersion, solvent evaporation and water/oil/water (w/o/w) double-emulsion. The technical parameters involved in the experimental method influence the morphology and the dimensions of the lipospheres, as well as the lipid mixtures and the types of selected stabilizer (Nastruzzi, 2005).

The bioadhesive properties of lipospheres make them ideal candidates to control the residence time and delivery of drugs topically administered, in particular for mucosal target.

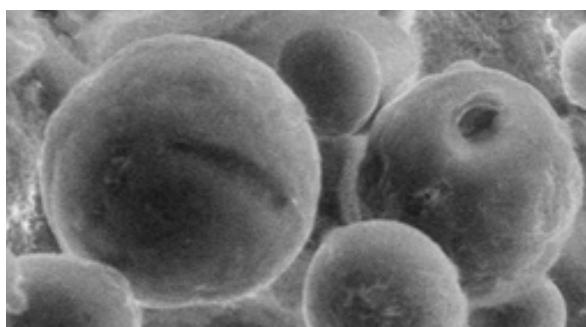


Figure 4: Microscopic image of Lipospheres

1.4.2. Solid Lipid Nanoparticles (SLN) and Nanostructured Lipid Carriers (NLC)

Solid Lipid Nanoparticles (SLN) were introduced at the beginning of the 1990s as an attracting delivery system compared to the pre-existing liposomes and synthetic polymeric nanoparticles. They represent the first-generation of particulate drug delivery system in nanoscale range able to overcome the drawbacks related to the previous formulations, such as the short stability or irritating effects.

SLN consist in a lipid matrix composed of a solid lipid or a mixture of solid lipids dispersed in an aqueous medium. The lipids typically used in this formulation can be triglycerides, complex glyceride mixtures, fatty acids or waxes and their content ranges from 0.1% (w/w) to 30% (w/w). Additionally, surfactants and emulsifiers due to their amphiphilic nature are employed with a concentration ranging between 0.5% (w/w) and 5% (w/w), in order to ensure the stability of the aqueous dispersion and to prevent particles agglomeration (Pardeike et al., 2009).

SLN display many advantages as biocompatibility, non-toxicity, preservation of drug from degradation and controlled release of encapsulated drug. Moreover, the production methods are cost effective, reproducible and scalable. The excellent tolerability of SLN as well as their small size between 10 and 1000 nm make them suitable for long-term topical administration, promoting drug penetration into deeper skin layer (Esposito et al., 2019).

Besides the numerous advantages described above, the limited drug loading, the decreased stability due to the polymorphic transition of lipid core and the consequent uncontrolled drug expulsion during storage represent some drawbacks of SLN. These limitations gave rise to the development of the second-generation of lipid nanoparticles, namely Nanostructured Lipid Carriers (NLC).

NLC are composed of a mixture of both solid and liquid lipids in a usual ratio of 70:30 up to 90:10. The presence of the liquid lipid in the composition generates an imperfect and disordered inner structure which offer more space to drug inclusion. Consequently, the drug-loading rate as well as the stability increased, reducing the leakage of drugs in storage (Carter et al., 2019).

Furthermore, the combination of solid and liquid lipids allows the formation of three different NLC patterns, namely imperfect, amorphous and multiple type. By avoiding crystallization, using special mixture of lipids and modifying the concentration of

components more imperfections are obtained to better accommodate the drug, compared to the perfect crystal structure of SLN (Gupta, 2020).

Figure 5 graphically represents the composition of SLN and NLC.

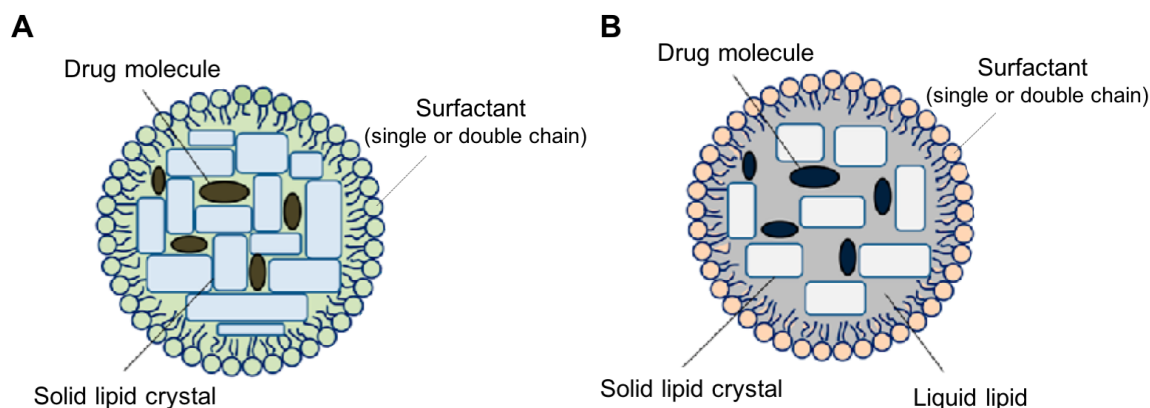


Figure 5: Schematic representation of SLN (A) and NLC (B) (Chuang et al., 2018)

Different methods are involved in the production of SLN and NLC, being similar in composition. The most common are high shear homogenization, ultrasonication, high-pressure homogenization, solvent dispersion, microemulsion and supercritical fluid method. Depending on the characteristics of the formulation, it is possible to select the adequate technique, in order to produce nanoparticles in large-scale, to avoid organic solvents or to encapsulate hydrophilic or lipophilic drugs.

Concerning the topical administration of SLN and NLC, it should be underlined that the interaction with the skin represent an important challenge for the permeation of active molecules. In fact, the lipid formulation when applied onto the skin adheres as a hydrophobic monolayer producing an occlusive effect and reducing moisture loss. The resulting disruption of corneocytes organization promotes the drug penetration up to the deeper skin layers. Moreover, the smaller the nanoparticles size, the easier the passage *via* follicular way (Esposito et al., 2019). Other studies consider the formation of drug reservoir in the SC when SLN are applied onto the skin and this behavior is responsible of the prolonged effect of the formulation (Üner et al., 2014).

1.4.3. Ethosomes

Ethosomes (ETHO) are lipid vesicular nano-systems characterized by aqueous dispersions of phosphatidylcholine previously solubilized in ethanol (Esposito et al., 2019). They represent the second generation of liposomes and they were first developed and described by Touitou in 2000 (Touitou et al., 2000).

The large amount of ethanol (20-50%) in the formulation is responsible of various advantages. On one hand, ethanol confers a softer and more malleable nature to vesicles, while on the other, it reduces their size and gives a negative surface charge, increasing the stability over time. Moreover, acting as penetration enhancer, it promotes the passage through the SC allowing to reach the deepest layers of the skin up to the dermis. Particularly, this ability is a consequence of the synergistic interaction between phospholipid and ethanol each other and with the skin barrier. Disturbing the organization of SC lipids, ethanol generates the decrease of intercellular lipid domains density. Then, the vesicles thanks to their flexibility and fluidity pass across the disturbed SC creating their own pathways (Sala et al., 2018). In a general way, the higher the ethanol content, the greater the permeation flux (Esposito et al., 2004).

The effectiveness of ethosomes as carriers for topical administration is found both in non-occlusive and occlusive conditions. Furthermore, they can carry either highly hydrophobic and highly hydrophilic drugs (*Figure 6*) and prolong their physical stability (Carter et al., 2019).

Compared to liposomes, the easy and cost effective manufacture method, based on the mixing of ethanolic solution of phosphatidylcholine and water under stirring, increases their suitable use for transdermal application.

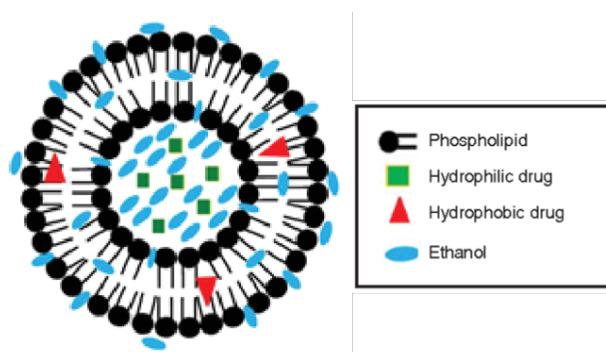


Figure 6: Schematic representation of ethosomes and their components (Kapoor et al., 2017)

1.5. GELS

The lipid-based delivery systems above described are characterized by poor viscosity and low lipid content, consequently they possess a scarce feasibility for topical administration. Indeed, SLN, NLC and ethosomes, being aqueous dispersions, are liquid after production, while lipospheres, being solids, scarcely adhere to skin or mucosa surface. With the aim of producing formulations suitable for dermal and transdermal application, the lipid-based systems need to be thickened. At this regard, their incorporation into vehicles, such as ointments, creams and gels could be proposed. Furthermore, the use of surfactant free vehicles, such as hydrogel, appears the best strategy, in order to reduce the possibility of interaction between surfactants and supramolecular structure of lipid nanoparticles (Esposito et al., 2019).

According to the definition, gels are semisolid systems, typically formed from a liquid phase that has been thickened with other components. The liquid forms a continuous phase, with the thickening agent enhancing viscosity by providing the porous scaffold of the gel (Aulton and Taylor, 2018). It is possible to classify hydrophobic or hydrophilic gels depending on the nature of continuous phase.

Hydrophilic gels, commonly called hydrogels, are composed of a network of hydrophilic polymer chains and they are capable of holding large amounts of water by swelling in aqueous media (Chai et al., 2017).

In this doctorate project, two different approaches were employed to incorporate the produced delivery systems into hydrogels. In the first one, the final viscosized product was obtained by dilution of vehicle with the nanoparticles, ethosomes or lipospheres, while in the second one, the thickening agent is directly added into the produced systems (Bhaskar et al., 2009; Esposito et al., 2013).

Numerous polymers are commonly employed as gelling agents. Particularly, natural polymers, such as xanthan gum and hyaluronic acid were used to obtain gelled micro and nano-systems with adhesive properties, exploiting the aqueous phase of the nanoparticle dispersion.

Furthermore, a synthetic polymer, namely Poloxamer, was employed to formulate “smart gels” able to self-assemble in water, leading to micelle formation and promoting the solubilization of lipophilic molecules.

1.5.1. Poloxamer gels

The non-ionic poly(oxyethylene)poly(oxypropylene) (PEO-PPO) block copolymer Poloxamer, also known as Pluronic[®], is an amphiphilic molecule that behaves as surfactant (*Figure 7A*). The amphiphilic character, based on the hydrophilicity of PEO and the hydrophobicity of PPO, is responsible of block segregation, giving rise to interesting and useful nanostructures, which self-assemble in solution (Bodratti and Alexandridis, 2018).

Poloxamers are available in a broad range of molecular weights and PPO/PEO ratios. These parameters as well as temperature and solvent type influence the micellization, leading to gels with final properties suitable for a wide range of applications (Mayol et al., 2008).

The micellization process is influenced by two key parameters, the critical micellization concentration (CMC) and critical micellization temperature (CMT). The micelles are generated in two conditions: when the PEO-PPO block copolymer concentration in solution reaches the CMC at a fixed temperature and increasing the temperature up to CMT at a fixed PEO-PPO block copolymer concentration (*Figure 7B*). In particular, the increased temperature leads to a decreased solubility of PEO-PPO portions which blocks in water. The resulting closely packed cubic micellar system generates a stiff hydrogel with thermo-sensitive properties (Bodratti and Alexandridis, 2018).

Poloxamer 407 (PEO₉₈PPO₆₇PEO₉₈, Pluronic[®] F127), selected in this doctorate project, at low concentrations around 15-25% w/w can generate hydrogels affected by thermo-reversible sol-gel transition phenomenon. This peculiar thermo-reversible character makes the poloxamer gels suitable for topical administration, passing from a low viscosity to a clear viscous gel at body temperature. Moreover, their effectiveness for the delivery of both lipophilic and hydrophilic drugs, makes them widely exploited in pharmaceutical fields.

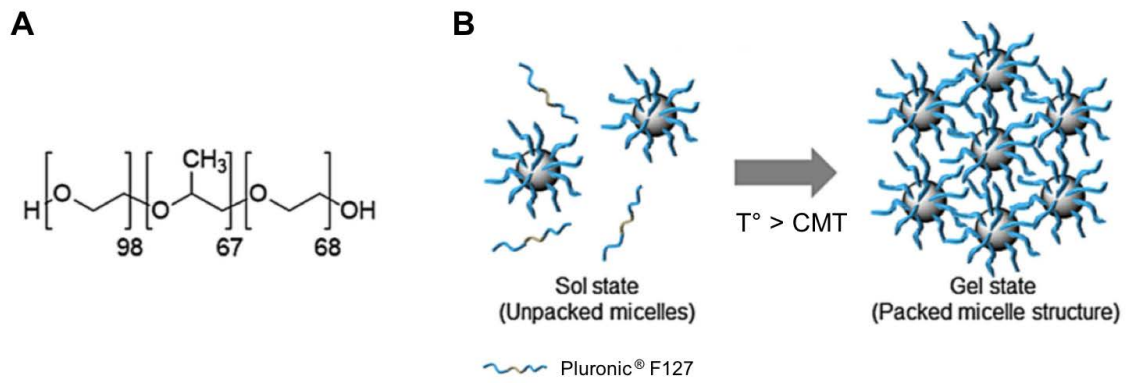


Figure 7: Chemical structure of Pluronic® F127 (**A**) and micellization process above $T_{\text{sol-gel}}$ (**B**) (Jung et al., 2017)

The development of drug delivery systems composed of biodegradable matrixes represent a “green” approach for topical administration. The several categories of formulations allow a deep interaction with the skin layers, controlling the release and the efficacy of the loaded drugs with local or systemic effects.

1.6. AIMS AND ORGANIZATION OF THE THESIS

In this doctorate project, Lipospheres (LS), Solid Lipid Nanoparticles (SLN), Nanostructured Lipid Carriers (NLC), Ethosomes (ETHO), and Poloxamer Gels have been proposed as new carrier systems for the topical administration of different active substances.

The thesis consists in eleven main chapters, describing the delivery systems, the active compounds and the application of the selected formulations.

The *first* chapter describes an introduction on skin and topical drug delivery systems, focusing on limits, advantages and innovative approaches to ameliorate the administration of drugs onto the skin.

The *second* and *third* chapters describe the materials and methods used in this work, respectively.

From the fourth to the tenth chapter, several drug delivery systems are investigated and their characterization is reported in detail. Moreover, in each study the *in vitro* technological and biological analysis, *ex vivo* or *in vivo* experiments are described in order to examine the efficiency of the formulations.

Particularly, in the *fourth* chapter Lipospheres Gel containing Clotrimazole are described for the treatment of *Candida albicans*. The production method and the characterization in terms of size, morphology, encapsulation efficiency, viscosity and adhesion have been realized. Finally, *in vitro* anticandidal activity studies and release studies have been performed.

The *fifth* chapter describes a scaling up study focused on the production of Progesterone containing nanoparticles in a pilot scale. Two different methods are developed and compared in order to obtain formulations in industrial scale. The study of dimension, morphology, encapsulation efficiency and stability of the produced nanoparticles has been realized. Furthermore, the *in vitro* release and skin permeation studies have been performed by dialysis and Franz cells methods respectively, and the *in vivo* experiments have been conducted by tape stripping.

The *sixth* chapter describes the production of nanoparticle based gel for wound healing treatment designed to deliver Hyaluronic Acid and Retinyl Palmitate onto the skin. After characterization of the nanoparticles containing Retinyl Palmitate, Hyaluronic Acid has been added to the dispersion with the aim of generating a

nanoparticulate gel suitable for cutaneous administration. Finally, *in vitro* scratch wound assay have been performed on a 2D cell model in order to study the improvement of the drug activity when delivered by nanoparticulate gel.

In the *seventh* chapter, the production of lipid nanoparticles for α -tocopherol delivery is described with the aim of protecting human skin against pollutants, as cigarette smoke. Firstly, a preformulation study has been conducted in order to select the optimal nanoparticles composition to encapsulate the drug. Then, the antioxidant effect of encapsulated α -tocopherol has been investigated through *ex vivo* experiments on human skin explants.

In the *eighth* chapter, the production and characterization of NLC and ETHO containing Ubiquinone have been developed and compared, with the aim of develop a novel strategy in the treatment of Rett syndrome. After a preformulation study based on the production of NLC-containing Ubiquinone, the lack of stability suggested the development of drug-loaded ETHO, resulting as promising lipid-based delivery systems. *In vitro* experiments revealed the uptake of ETHO into human fibroblasts and the effect of Ubiquinone in protecting cells against oxidative insults.

The *ninth* and *tenth* chapters describe the production and characterization of Poloxamer Gel for the delivery of the antioxidants Gallic Acid and Caffeic Acid. The gels have been analyzed through rheological and spreadability assays, then *in vitro* tests have been performed to study the diffusion of the drug from the gels and the activity on cells.

The *last* chapter contains the conclusions of the work, considering the obtained results.

2. MATERIALS

The copolymers poly (ethylene oxide) (a) – poly (propylene oxide) (b) (poloxamer 188 a=80, b=27 and poloxamer 407 a=98, b= 67) were obtained from BASF (Ludwigshafen, Germany).

Miglyol 812 N, caprylic/capric triglycerides (TRIC, miglyol) was a gift of Cremer Oleo Division (Witten, Germany).

C12-C13 alkyl lactate, Cosmacol ELI (AL) was from Sasol (Milan, Italy).

PrimalHyal 50 (HA₅₀) and PrimalHyal 300 (HA₃₀₀), hydrolyzed HA with MW 20-50 kDa and 100-300kDa respectively, were gifts of Soliance (Pleumeur-Bodou, France). Hyacare sodium hyaluronate MW 800 kDa was a gift of Evonik (Darmstadt, Germany).

The soybean lecithin (PC) (90% phosphatidylcholine) was Epikuron 200 from Lucas Meyer, (Hamburg, Germany).

Strat-M[®] was a kind gift of Merck Millipore (KGaA, Darmstadt, Germany).

Dulbecco's modified Eagle's medium (DMEM) High Glucose and Low Glucose, Minimum Essential Medium Eagle with Earle's BSS (EMEM) fetal bovine serum (FBS), antibiotic agent (penicillin–streptomycin) and trypsin-EDTA were purchased from Lonza Group (Milan, Italy).

Glyceryl distearate (precirol ATO5, precirol), glyceryl dibehenate (compritol 888ATO, compritol) and mono-, di-, tri-glyceride esters of fatty acids (C10-C18) (suppocire AM, suppocire) were kind gifts of Gattefossè (Milan, Italy).

Tristearin, Stearic triglyceride (TRIST), xanthan gum (x-gum), clotrimazole (CLO), agar, progesterone (PRG), retinyl palmitate (RP), LDH kit, Methylthiazolyldiphenyl-tetrazolium bromide (MTT), Trypan Blue, α -tocopherol (TOC), Ubiquinone (Ub-O), Gallic acid (GA), Caffeic acid (CA), mixed esters cellulose, polycarbonate, polyvinylidene fluoride, polytetrafluoroethylene, nylon membranes, hydrogen peroxide (H₂O₂, 30% solution), all other reagents and HPLC solvents were purchased from Sigma-Aldrich, Merck (Darmstadt, Germany).

3. METHODS

3.1. NANOSYSTEMS PRODUCTION

3.1.1. Liposphere Production

Lipospheres (LS) were produced by the melt-dispersion technique and the detailed composition is reported in *Table 8* (Cortesi et al., 2002). Briefly, 1 g of tristearin or a lipidic mixture, in the absence or in the presence of 20 mg of clotrimazole (CLO), was melted at 75°C and emulsified with 150 ml of an aqueous phase containing poloxamer 188 (5%, w/w).

The emulsion was stirred for 1 h at 2000 rpm using a mechanical stirrer Eurostar Digital (IKA Labortechnik, Staufen, Germany) equipped with a three-blade rotor impeller with a diameter of 55 mm. The milky formulation was then rapidly cooled to about 20°C under stirring in an ice bath, yielding a uniform dispersion of LS. The obtained LS were then washed with water and isolated by filtration through a paper filter. LS were left to dry overnight at 25°C and weighed.

LS yield was calculated as follows (Cortesi et al., 2002):

% Yield = $\text{LS weight} \times 100 / \text{Total weight of lipids employed for LS preparation}$

3.1.2. Lipid Nanoparticles

Lipid Nanoparticles (LN) were prepared by hot homogenization technique based on ultrasound or high pressure method. In both methods, the lipid phase (5% or 10% by weight with respect to the whole weight of the dispersion) was constituted of solid lipids in the case of SLN preparation or a mixture of solid and liquid lipids in the case of NLC preparation, while the aqueous phase was a poloxamer 188 solution (2.5% w/w).

The detailed composition of SLN and NLC for each project is described in the correspondent chapters. For both methods, in the case of drug loaded nanoparticles, the drug was added to the fused lipid phase before emulsification step.

- **Ultrasound homogenization (UH) method**

The lipid phase was melted at 80°C and the aqueous phase was heated at the same temperature. Afterwards, the aqueous phase was dispersed in the fused lipid phase using a high-speed homogenizer (Ultra Turrax - Janke and Kunkle, Ika-Werk, Sardo, Italy) at 15,000 rpm for 1 minute. The resultant emulsion was subjected to ultrasonication (Microson™, Ultrasonic cell Disruptor - XL MISONIX®) at 7 kHz for 15 minutes and then cooled down to room temperature. LN dispersions were stored at room temperature (Esposito et al., 2017b).

- **High pressure homogenization (HPH) method**

As first step, the aqueous phase heated at 80°C was added to the molten lipid phase and subjected to stirring at 15,000 rpm, 80°C for 1, 2 or 3 min. The emulsion was homogenized using high pressure homogenizer for 1–3 cycles at 100 MPa (Panda Plus2000/GEA Niro Soavi, Parma, Italy) to form o/w nanoemulsion. The nanoemulsion was then cooled by a coil employed as heat exchanger directly connected to the instrument for solidification and formation of lipid nanoparticles. LN dispersions were stored at room temperature.

3.1.3. Ethosomes production

For the preparation of ethosomes (ETHO), PC (30 mg/ml) was first dissolved in ethanol. Afterwards, bidistilled water was slowly added to the ethanolic solution (30 % v/v) under continuous magnetic stirring at 700 rpm for 30 min at room temperature in the dark (Esposito et al., 2016b).

In the case of Ub-O containing ETHO (ETHO Ub-O), Ub-O (1 mg/ml) was solubilized into PC ethanol solution before addition of water. *Table 29* reports the ETHO composition.

3.1.4. Gels production

- **Xanthan gum gel production**

A weighed amount of xanthan gum (x-gum) (0.5% w/w) was gradually added to citrate buffer 5 mM, pH 4 (prepared by dissolving citric acid monohydrate and trisodium citrate dihydrate in distilled water) and then mixed for 15 min (Aka-Any-Grah et al., 2010). The gel was left to stand at 25°C overnight for complete swelling,

afterwards LS (5% w/w), CLO (0.1% w/w), or AL (0.05% w/w) were alternatively added and manually mixed until homogeneous dispersion (gel names and compositions are reported in *Table 11*). Particularly, for the preparation of Gel L_{STRIST}-CLO and Gel L_{STRIST/AL1}-CLO, L_{STRIST}-CLO and L_{STRIST/AL1}-CLO were respectively added into the xanthan gum gel, while Gel-CLO and Gel_{AL1}-CLO, employed as controls, were obtained by directly adding free CLO and AL into the xanthan gum gel.

- **Hyaluronic Acid gel production**

Hyaluronic Acid (HA) gel were prepared by direct addition of HA 50, 300, 800 kDa (named HA₅₀, HA₃₀₀ and HA₈₀₀ respectively) into water and stirring by an orbital shaker at 150 rpm for 12 h at room temperature. The concentration employed in each formulation is reported in chapters 6 and 10.

- **Poloxamer gel production**

Poloxamer gel was prepared according to the “cold technique” (Esposito et al., 1996). A weighed amount of poloxamer 407 was gradually added to cold water (5-10°C) under magnetic stirring. The container was sealed and left in a refrigerator overnight at 5°C.

In the case of drug loaded gels, the drug powder was added to the produced gel under vortex motion at 30 Hz.

The composition of the formulated gels is described in chapters 9 (*Table 32*) and 10 (*Table 35*).

- **Production of viscous LN dispersions**

X-gum and HA were considered as viscosizing agents for LN dispersions.

For PRG containing LN, SLN and NLC viscosity has been improved by adding x-gum (1%, w/w) directly into the dispersion and by slowly stirring for 1 h followed by hand mixing, until complete dispersion of the gum. The obtained viscous nanoparticle formulations have been named SLN-PRG/G and NLC-PRG/G.

For RP containing NLC, Nanoparticle based gels were prepared by direct addition of HA into the preformed nanoparticle dispersions, particularly HA₅₀, HA₃₀₀ and HA₈₀₀ were alternatively employed. NLC-HA gel were obtained adding HA (0.5% w/w) into NLC (with or without RP), afterwards the systems were left to swell under stirring by an orbital shaker at 150 rpm for 12 h at room temperature.

3.2. NANOSYSTEMS CHARACTERIZATION

3.2.1. Variable-pressure scanning electron microscopy (VPSEM)

The morphology of LS was evaluated by variable-pressure scanning electron microscopy (VPSEM) (Zeiss Evo 40XPV, Carl Zeiss AG, Oberkochen, Germany). Briefly, 10 mg of LS were directly put on a stub without any recoat and observed under variable pressure (Griffin, 2007). To analyze the internal morphology, dried LS were sectioned with a long stainless steel blade, under a binocular microscope. LS size distributions were determined measuring at least 300 LS/sample. The analyses were conducted by the group of the Electron Microscopy Center of the University of Ferrara (Italy).

3.2.2. Photon correlation spectroscopy (PCS)

Submicron particle size analysis was performed using a Zetasizer Nano S90 (Malvern Instr., Malvern, England) equipped with a 5-mW helium neon laser with a wavelength output of 633 nm. Glassware was cleaned of dust by washing with detergent and rinsing twice with water for injections. Measurements were made in triplicate at 25 °C at an angle of 90 °, data were interpreted using the “CONTIN” method (Pecora, 2000). Each experimental value results from three independent experiments were performed in triplicate.

3.2.3. Cryogenic Transmission Electron Microscopy (Cryo-TEM)

Samples were vitrified as previously described (Esposito et al., 2008). The vitrified specimen was transferred to a Zeiss EM922Omega transmission electron microscope for imaging using a cryoholder (CT3500, Gatan). The temperature of the sample was kept below -175°C throughout the examination. Specimens were examined with doses of about 1000-2000 e/nm² at 200 kV. Images were recorded digitally by a CCD camera (Ultrascan 1000, Gatan) using an image processing system (GMS 1.9 software, Gatan). In addition, size distribution of nanoparticles was performed by measuring 1000 nanoparticles for each cryo-TEM image by the digital analyzer ImageJ 1.48v.

The analyses were conducted by Dr. Markus Drechsler of the University of Bayreuth

(Germany).

3.2.4. X-ray diffraction measurements

X-ray diffraction experiments were performed using a 3.5 kW Philips PW 1830 X-ray generator (Amsterdam, Netherlands) equipped with a Guinier-type focusing camera (homemade design and construction, Ancona, Italy) operating with a bent quartz crystal monochromator ($\lambda = 1.54 \text{ \AA}$). Diffraction patterns were recorded on GNR Analytical Instruments Imaging Plate system (Novara, Italy). Samples were held in a tight vacuum cylindrical cell provided with thin mylar windows. Diffraction data were collected at 37° . In each experiment, Bragg peaks were detected. The few peaks in the low-angle region were indexed considering the different symmetries commonly observed in lipidic phases (Luzzati et al., 1997) and the unit cell dimension of the phase, a , calculated from the averaged spacing of the observed peaks. Peaks in the wide-angle x-ray scattering region relate to the lateral organization of the hydrocarbon chains: from their positions, the subcell structure of the nanoparticles was determined.

The experiments were performed by the group of Prof. Mariani of Università Politecnica delle Marche (Italy).

3.2.5. Small-angle X-ray scattering (SAXS) measurements

Small-Angle X-ray scattering (SAXS) experiments were performed at the SAXS BM29 Beamline of the European Synchrotron (ESRF) in Grenoble, France. NLC samples were filled in glass capillaries. The experiments were performed at 30 and 37°C , both in the presence and in the absence of drug. The wavelength used was 0.99 \AA and the investigated Q-range ($Q = 4\pi \sin\theta / \lambda$, where 2θ is the scattering angle and λ is the x-ray wavelength) was from 0.01 to 0.5 \AA^{-1} . The sample exposure time was 160 s, which ensured enough statistical accuracy without degrading the samples by radiation. The Bragg peaks eventually observed were indexed considering the possible symmetries commonly observed in lipid systems (lamellar, hexagonal or cubic) (Kulkarni, 2012). Accordingly, from the averaged spacing of the observed peaks the unit cell dimension of the phase was calculated.

The experiments were performed by the group of Prof. Mariani of Università Politecnica delle Marche (Italy).

3.2.6. Fourier Transform Infrared (FTIR) Spectroscopic Analysis

The FTIR spectra of pure RP, HA₃₀₀, the physical mixtures of RP, HA₃₀₀, tristearin and miglyol, poloxamer 188 solution, NLC-RP and NLC-RP-HA gel were recorded by FTIR spectrophotometer (Spectrum 100 FT-IR spectrometer, Perkin Elmer, Monza, Italy) in the range of 4000–650 cm⁻¹ using Transmittance Mode during 8 scans. The FTIR spectra were normalized and major vibration bands were associated with chemical groups (Esposito et al., 2018a).

3.2.7. Viscosity test

Rheology measurements were performed by a Viscolead ADV, Fungilab viscometer (Fungilab, Barcelona, Spain). Gels were poured into a 250-ml beaker, where they were tested at 25°C. The spindle was immersed to its immersion mark in the different areas of the beaker, for each trial. Viscosity was measured at different speed, comprised between 1 and 100 r.p.m. (Esposito et al., 2018b).

3.2.8. Rheological measurements

Rheological measurements were performed with an AR-G2 controlled-stress rotational rheometer (TA Instruments, USA). The geometry used was an aluminum cone-plate with a diameter of 40 mm, an angle of 1° and a truncation of 28 μm, equipped with a solvent trap in order to prevent solvent evaporation during the experiments. The viscoelastic properties of the gels (elastic modulus G' and viscous modulus G'') were assessed in oscillation mode. Oscillation frequency was set at 1 Hz and the deformations applied were all in the linear regime. Temperature ramps from 5°C to 50°C were obtained at a temperature rate of 1°C/min and were controlled by a Peltier plate. Before starting the experiments, a 2-min conditioning time at 5°C was applied (Sguizzato et al., 2020). Measurements were performed in triplicate at least for each sample, to ensure reproducibility.

The experiments were performed by the group of Prof. Nicolas Huang of the Institut Galien Paris-Sud (University of Paris-Sud) (France).

3.2.9. Spreadability studies

The spreading capacity was evaluated 48 h from preparation. Precisely, 100 mg of gel were placed on a Petri dish (3 cm diameter) and then subjected to pressure by a glass dish carrying a 50- to 500-g mass. The time taken by the gel to fill the entire dish was measured.

Spreadability test was performed three times and the mean values \pm standard deviations were calculated using the following equation:

$$S = m \times l / t \quad (1)$$

where S is the spreadability of the gel formulation, m is the weight (g) tied on the upper plate, l is the diameter (cm) of the glass plates, and t is the time (s) taken for the gel to fill the entire diameter (Esposito et al., 2018b).

3.2.10. Gel leakage and adhesion test

To test leakage and adhesion of formulations, pH 4.5 citrate buffer and simulated vaginal fluid (SVF) were prepared (Aka-Any-Grah et al., 2010). Briefly, to prepare SVF pH 4.5, NaCl, KOH, Ca(OH)₂, bovine serum albumin, lactic acid, acetic acid, glycerol, urea and glucose were dissolved in distilled water (Aka-Any-Grah et al., 2010). Agar (1.5 % w/w) was added to citrate buffer or SVF and stirred at 95°C until solubilization. The gels obtained after cooling were then cut to obtain rectangular agar slide.

Gel LS_{TRIST/AL1}-CLO and Gel_{AL1}-CLO were colored for leakage test by dissolving rhodamine (0.05 % w/w) in the gels before adding LS_{TRIST/AL1}-CLO or AL and CLO. For leakage test, 50 mg of colored gels or 2.5 mg of dry LS_{TRIST/AL1}-CLO were placed onto one end of a citrate buffer or SVF agar slide. The agar slide was vertically put at an angle of 90° on one of the inner walls of a transparent box, maintained at 37°C \pm 1°C. The running distance of the gel along the slide was measured 1 and 10 min after formulation placement. Gel leakage was measured three times, the mean values \pm standard deviations were calculated.

For adhesion test, 200 mg of Gel_{AL1}-CLO, Gel LS_{TRIST/AL1}-CLO or 10 mg of dry LS_{TRIST/AL1}-CLO were placed at the center of citrate buffer and SVF agar slides. The agar slides were respectively immersed in 10 ml of citrate buffer or SVF at 37°C \pm 1°C for 2 hs. Gel or LS residence time on slides (adhesion time) was visually compared (Witczak, 1997). The tests were performed three times.

3.3. DRUG CONTENT

3.3.1. Encapsulation efficiency (EE) and loading capacity (LC)

The amount of encapsulated CLO per mg of dry LS was determined by disintegrating 50 mg of LS in 5 ml of ethanol under stirring (300 r.p.m.) at 60°C for 2 h.

Samples were filtered (nylon membrane filters, 0.2 µm pore size, Merck Millipore, Italy) and analyzed by high performance liquid chromatography (HPLC) (Esposito et al., 2013).

The encapsulation efficiency (EE) and loading capacity (LC) of PRG, RP, TOC in LN were determined as previously described (Puglia et al., 2010). Half milliliter aliquot of each LN batch was loaded in a centrifugal filter (Microcon centrifugal filter unit YM-10 membrane, NMWCO 10 kDa, Sigma Aldrich, St Louis, MO, USA) and centrifuged (Spectrafuge™ 24D Digital Microcentrifuge, Woodbridge NJ, USA) at 8,000 rpm for 20 min. The amount of drug was determined after dissolving the lipid phase with a known amount of methanol (1:10, v/v) for 2 h under stirring. The dispersion sample was filtered through nylon filter (0.2 µm).

The EE of Ub-O in ETHO was determined by dissolving ETHO Ub-O with a known amount of mobile phase (1:10, v/v) for 30 min under stirring. The dispersion sample was filtered through nylon filter (0.2 µm).

GA chemical stability was evaluated by determining its content by dissolving the gel with a known amount of water (1:20, v/v). The obtained dispersion was maintained in an ice bath under magnetic stirring for 30 min. A dispersion sample was filtered through nylon filter (0.45 µm).

The content of CLO, PRG, RP, TOC, Ub-O and GA was determined by HPLC.

The analyses were conducted in triplicate. EE and LC were determined using equations (2) and (3):

$$EE = L / T \times 100 \quad (2)$$

$$LC = L / T_{\text{lipid phase}} \times 100 \quad (3)$$

where L is the amount of drug effectively present within the delivery system, T stands for the total amount of drug initially added to the lipid phase and $T_{\text{lipid phase}}$ is the total weight of lipid phase in the formulation. Determinations were performed in six times in independent experiments and the mean values ± standard deviations were calculated.

3.3.2. Prediction of Long-Term Stability

The stability of PRG and RP in LN kept at room temperature was assessed in time, determining drug content by HPLC analyses. To calculate shelf life values \log (drug residual content, %) was plotted against time (Esposito et al., 2013). The slopes (m) calculated by linear regression were substituted into the following equation for the determination of k values:

$$k = m \times 2.303 \quad (4)$$

As reported by Wells (Wells, 1988), shelf life values, i.e. t_{90} , the time for 10% loss, and $t_{1/2}$, the time for 50% loss, were then calculated by the following equations:

$$t_{90} = 0.105/k \quad (5)$$

$$t_{1/2} = 0.693/k \quad (6)$$

3.3.3. High performance liquid chromatography (HPLC) analysis

HPLC determinations were performed using a HPLC system (1200 Series, Agilent Technologies, USA) equipped with an isocratic pump, an UV-detector and a 7125 Rheodyne injection valve with a 50 μ l loop.

Each injection was performed in triplicate ($n=3$) and compared with standards of known concentration.

Details of HPLC conditions for each drug studied are below reported in *Tables 1 to 7*.

Table 1: HPLC analysis method for CLO

Specification	Details - CLO
Column	C ₁₈ RP-column (Alltech® - Hypersil BSD (5 μ m) 4.6 x 150 mm)
Mobile phase	Methanol : Water 80:20 v/v
Flow	0.8 ml/min
Injection	50 μ l
Wavelength	210 nm

Table 2: HPLC analysis method for PRG

Specification	Details - PRG
Column	C ₁₈ RP-column (Agilent® - Zorbax Eclipse XBD (5 mm) 4.6 x 150 mm)
Mobile phase	Methanol : Water 80:20 v/v
Flow	1.0 ml/min
Injection	50 µl
Wavelength	220 nm

Table 3: HPLC analysis method for RP

Specification	Details - RP
Column	C ₁₈ RP-column (Agilent® - Zorbax Eclipse XBD (5 mm) 4.6 x 150 mm)
Mobile phase	Methanol : Water 70:30 v/v
Flow	1.0 ml/min
Injection	50 µl
Wavelength	350 nm

Table 4: HPLC analysis method for TOC

Specification	Details - TOC
Column	C ₁₈ RP-column (Kinetex® (5 µm) 4.6 x 150 mm)
Mobile phase	Methanol 100
Flow	1.0 ml/min
Injection	50 µl
Wavelength	225 nm

Table 5: HPLC analysis method for Ub-O

Specification	Details - Ub-O
Column	C ₁₈ RP-column (Kinetex® (5 µm) 4.6 x 150 mm)
Mobile phase	Acetonitrile : Tetrahydrofuran : Water 55:40:5 v/v/v
Flow	1.0 ml/min
Injection	50 µl
Wavelength	275 nm

Table 6: HPLC analysis method for GA

Specification	Details - GA
Column	C ₁₈ RP-column (Grace® - Platinum (5 µm) 4.6 x 150 mm)
Mobile phase	Phosphoric acid : Methanol : Water 0.1:20:80 v/v/v
Flow	0.5 ml/min
Injection	50 µl
Wavelength	273 nm

Table 7: HPLC analysis method for CA

Specification	Details - CA
Column	C ₁₈ RP-column (Grace® - Platinum (5 µm) 4.6 x 150 mm)
Mobile phase	Water : Acetonitrile (pH 2.5) 80:20 v/v
Flow	0.7 ml/min
Injection	50 µl
Wavelength	325 nm

3.4. IN VITRO TECHNOLOGICAL STUDIES

3.4.1. *In vitro* release studies

The *in vitro* release studies were performed by dialysis on CLO alternatively included in LS_{TRIST/AL1}-CLO, LS_{TRIST}-CLO, Gel LS_{TRIST/AL1}-CLO, Gel LS_{TRIST}-CLO, and Gel_{AL1}-CLO, and on PRG alternatively solubilized in SLN-PRG, NLC-PRG or suspended in poloxamer 188 solution (2.5% w/w) (Cortesi et al., 2002).

Briefly, samples were placed into a dialysis tube (6 cm) (molecular weight cut-off 10,000–12,000; Medi Cell International, London, UK), then placed into a specific volume of a receiving phase and shaken in a horizontal shaker (MS1, Minishaker, IKA) at 175 r.p.m. at 37°C.

Particularly, for CLO 200 mg of LS or 4 g of gel were used and the release kinetics of free CLO were investigated placing in dialysis tubes 2 mg of CLO dispersed in 4 ml of distilled water or in 4 g of xanthan gum gel. In addition, 40 ml of SVF and ethanol (80:20, v/v) were used as receiving phase. For PRG 2 ml of SLN, NLC or

poloxamer 188 solution were used and 30 ml of phosphate buffer (10 mM, pH 4.7) and ethanol (70:30, v/v) were selected as receiving phase.

Samples of receiving phase were withdrawn at regular time intervals and analyzed by HPLC, as described above. Fresh receiving phase was added to maintain a constant volume. The drug concentrations were determined six times in independent experiments and the mean values \pm standard deviations were calculated.

3.4.2. *In vitro* diffusion studies

In vitro diffusion studies were performed using Franz-type diffusion cells supplied by Vetrotecnica (Padua, Italy) associated to different membranes.

Samples of dried membranes were rehydrated by immersion in distilled water at room temperature for 1 h before being mounted in Franz cells. Namely stratum corneum epidermis (SCE), cellulose, polycarbonate, polyvinylidene fluoride, polytetrafluoroethylene, nylon, Strat-M[®] (polyethersulfone / polyolefin) or sandwich (cellulose / polytetrafluoroethylene / cellulose) membrane systems were alternatively employed (Esposito et al., 2017c). SCE membranes were obtained from breast reduction operations. Briefly, subcutaneous fat was carefully trimmed and the skin was immersed in distilled water at $60 \pm 1^\circ\text{C}$ for 2 min, after which SCE was removed from the dermis using a dull scalpel blade. SCE membranes were dried in a desiccator at ~25% relative humidity. The dried samples were wrapped in aluminum foil and stored at $4 \pm 1^\circ\text{C}$ until use (Esposito et al., 2017d; Puglia et al., 2010). SCE membranes were kindly supplied by Prof. Carmelo Puglia of the University of Catania.

The exposed membrane surface area was 0.78 cm² area (1 cm diameter orifice). The receptor compartment contained 5 ml of phosphate buffer (10 mM, pH 4.7) and ethanol (50:50, v/v) in the case of PRG and RP, or 5 ml of bidistilled water in the case of GA and CA. This solution was stirred at 500 rpm with the help of a magnetic bar and thermostated at $32 \pm 1^\circ\text{C}$ during all the experiments (Siewert et al., 2003). Approximately 1 g of each formulation was placed on the membrane surface in the donor compartment and the latter was sealed to avoid evaporation. At predetermined time intervals comprised between 1 and 24 h, samples (0.15 ml) of receptor phase were withdrawn and the drug concentration in the receptor phase was measured using HPLC. Each removed sample was replaced with an equal

volume of simple receptor phase. The drug concentrations were determined six times in independent experiments and the mean values \pm standard deviations were calculated. The mean values were then plotted as a function of time. The diffusion coefficients were computed from the linear portion of the accumulation curve and expressed as normalized fluxes by dividing by drug concentration in the analyzed form, expressed in mg/ml.

In the case of PRG, after 6 and 24 h of permeation studies, to determine skin uptake, SCE portions (4.52 cm² area) were removed from the diffusion cell, rinsed with water and immersed in 5 ml of methanol, homogenized in vortex for 2 min, filtered by nylon membranes (200 nm diameter pores) and analyzed by HPLC.

The data were analyzed using Student's t-test, considering $p < 0.05$ as the minimum level of significance.

3.5. IN VITRO BIOLOGICAL STUDIES

3.5.1. Anticandidal activity study

Antifungal activity was studied against *Candida albicans* (ATCC 10231). The experiment was performed based on standardized protocol M27-A2, CLSI. Mother cultures of *C. albicans* strain has been set up starting from 1.5 ml of liquid nitrogen stored inoculum put in 250 ml sterile flasks containing 98.5 ml of liquid YEPD medium (yeast extract 0.5%, bactopectone 1%, glucose 2%; Oxoid, Italy) placed at 37°C on an orbital shaker (110 r.p.m.). The inocula were performed after growth (48 h/35°C) on Sabouraud dextrose agar. The colonies were suspended in 0.85% sterile saline and this suspension was homogenized in a vortex mixer for 15 s; after that, cell density was set in a spectrophotometer and transmittance ($\lambda=530$ nm) was adjusted to match standard 0.5 on the McFarland scale (1×10^6 to 5×10^6 yeast/ml). In the sequence, a 1:50 dilution in RPMI 1640 MOPS buffered medium was performed, resulting in a final concentration of $1.5 \pm 1.0 \times 10^3$ yeasts/ml.

The microdilution technique (Jahn et al., 1995; Rex and Clinical and Laboratory Standards Institute, 2008) was performed in 96-wells polystyrene sterile plates; the culture medium was RPMI1640-MOPS buffered broth. The tested samples were: LS_{TRIST}-CLO, LS_{TRIST/AL1}-CLO, LS_{TRIST}, LS_{TRIST/AL1} and CLO methanolic solution. Namely, 25 mg of the dry formulation was weighed and suspended in 200 μ l of the

culture medium in the first well, then two-fold serial dilutions were performed in wells from 1 to 10. For CLO methanolic solution, 100 µl of CLO twice more concentrated than the desired final concentrations were diluted with 100 µl of culture medium in the first well.

To each well microdilution plate were added 100 µl of the standardized inoculum. Experiments were run in triplicate. The plates were incubated at 35°C for 48 h, afterwards 10 µl of 0.5% 2,3,5-triphenyltetrazolium chloride and 10 µl containing menadione 1 mM were added to all wells (Jenning et al., 2000), the plates were then reincubated at 35°C for 120 min. After addition of 0.1 ml of acid isopropanol (isopropanol / HCl 1 N, 95:5, v/v), the plates were placed on a shaker for 5 min to dissolve formazan crystals. Measurements were performed with a microplate reader at 550 nm and the minimal inhibitory concentration (MIC) was determined. Statistical analysis was conducted by t-Student test.

The experiment was carried out at the Faculty of Pharmacy (Antiparasitic Chemotherapy-CNRS 8076) of University of Paris-Sud (France).

3.5.2. Cell culture and treatments

In vitro assays on cell culture were carried out using human cells, namely immortalized keratinocytes (HaCaT), primary dermal fibroblasts isolated from skin biopsy of a healthy control subject and human melanoma cells (Sk-Mel 28).

HaCaT cells were grown in Dulbecco's modified Eagle's medium (DMEM) High Glucose, supplemented with 10% FBS (fetal bovine serum), 100 U/ml penicillin, 100 µg/ml streptomycin and 2 mM L-glutamine. Cells were incubated at 37°C for 24 h in 95% air/5% CO₂ until 80% confluence.

Fibroblast cells were grown in Dulbecco's modified Eagle's medium (DMEM) Low Glucose, supplemented with 10% FBS, 100 U/ml penicillin, 100 µg/ml streptomycin and 2 mM L-glutamine. Cells were incubated at 37°C for 24 h in 95% air/5% CO₂ until 80% confluence.

Sk-Mel 28 cells were grown in Minimum Essential Medium Eagle with Earle's BSS (EMEM), supplemented with 10% FBS (fetal bovine serum), 100 U/ml penicillin, 100 µg/ml streptomycin and 2 mM L-glutamine. Cells were incubated at 37°C for 24 h in 95% air/5% CO₂ until 80% confluence.

For cell treatments, the different vehicles were initially dissolved in cell culture medium.

For RP cell treatment studies, stock solutions containing 500 µg/ml HA and 70 µg/ml RP were further diluted to reach the final concentration of HA 25 µg/ml and RP 3.5 µg/ml for each vehicle.

For TOC cell treatment studies, stock solutions containing TOC 500 µM were further diluted to reach the final concentrations ranging from 25 to 200 µM.

For Ub-O cell treatment studies, stock solutions containing Ub-O 500 µM were further diluted to reach the final concentrations ranging from 1 to 41.3 µM.

For GA cell treatment studies, stock solutions containing GA 500 µM were further diluted to reach the final concentrations ranging from 1 to 200 µM.

For CA cell treatment studies, stock solutions containing CA 500 µM were further diluted to reach the final concentrations ranging from 5 to 200 µM.

3.5.3. Cytotoxicity studies

All tests were performed in triplicate and assay was repeated three times independently with similar results.

- LDH assay

Seeded cells were treated for 24 h with the different vehicles at various concentrations. Cytotoxicity was evaluated by spectrophotometric quantification of the LDH released in culture medium, using a commercial kit (Sigma-Aldrich, Merck, Darmstadt, Germany), as previously described (Esposito et al., 2015b; Valacchi et al., 2015).

- MTT assay

Seeded cells were exposed to the selected formulations for 24 h, afterwards the treatment was completely removed and 50 µl of serum-free media and 50 µl MTT (0.5 mg/ml) were added and incubated for 3 h. The MTT is reduced in living cells, forming insoluble purple formazan crystals that were then dissolved in 100 µl of DMSO at 37°C for 15 minutes. After shaking, the solution absorbance, being proportional to the number of living cells, was measured using a spectrophotometer at 590 nm using 670 nm as a reference wavelength, thus converted into percentage of viability (Sguizzato et al., 2020).

- **Trypan blue exclusion assay**

Seeded cells were treated for 24 h with the different vehicles at various concentrations. Afterwards, detached cells were diluted 1:1 with Trypan blue (0.5% solution), then 10 µl of cell suspension were applied on a Bürker Chamber for counting the living cells with an inverted microscope. The results were reported in number of viable cells and the percentage was calculated in relation to non-treated cells, used as control (100% viability).

3.5.4. Wound healing assay

Cells were grown to confluent monolayer on 24-well plates, then cells were mechanically scratched with a 200 µl sterile pipette tip (Valacchi et al., 2009). After washing in PBS to remove cellular debris, cells were immediately treated with the different vehicles at the concentrations selected based on the cytotoxicity data, followed by incubation at 37°C. Images of the scratches for each sample were recorded at different time points (i.e. 0, 12, 18, 24 and 36 h post-scratch). The width of the scratches was analyzed with ImageJ software (National Institutes of Health, Bethesda, MD, USA) and compared to the wound area at 0 h, which was arbitrarily set as 100.

3.5.5. Transmission electron microscopy (TEM)

Cells treated with ETHO for 24 h and non-treated cells, used as control, were grown to confluent monolayer on 10 cm Petri dish. Cells were fixed in 2.5% glutaraldehyde in cacodylate buffer for 3 h at 4°C. Then cells were post-fixed in 1% osmium tetroxide for 2 h at 4°C, dehydrated in a graded series of alcohol, embedded in Araldite resins, and polymerized in oven for 48 h at 60°C. Ultrathin sections of 60 nm were cut with an ultramicrotome (Ultratome Reichert SuperNova Leica, Wien, Austria), stained with uranyl acetate and lead citrate and examined in a Philips CM100 transmission electron microscope (Pecorelli et al., 2016c).

3.5.6. Immunocytochemistry

Cells were grown on coverslips at a density of 1×10^5 cells/ml and, after 24 h of treatment with the different vehicles (ETHO, ETHO Ub-O), cells were exposed to 50

$\mu\text{M H}_2\text{O}_2$ for 1 h. After H_2O_2 exposure, the medium was changed with fresh medium and the cells were analyzed at two different time points (i.e. 2 and 6 h post exposure).

Afterwards, cells were fixed in 4% paraformaldehyde for 10min at room temperature (RT). Cells were then permeabilized for 5 min at RT with PBS containing 0.2% Triton X-100, then the coverslips were blocked in PBS containing 1% BSA at RT for 1 hr. Cells were then incubated with primary antibody for 4HNE (AB5605; Millipore Corporation) (1:200) in PBS containing 0.5% BSA at 4°C overnight. After washing, coverslips were incubated with appropriate secondary antibody (1:100) for 1 hr at RT. Nuclei were stained with 1 $\mu\text{g/ml}$ DAPI (Sigma–Aldrich) for 1 min. Coverslips were mounted onto glass slides using anti-fade mounting medium 1,4 diazabicyclooctane (DABCO) in glycerin and examined by the Leica light microscope equipped with epifluorescence at 20X magnification. Negative controls for the immunostaining experiments were performed by omitting primary antibody. Images were acquired and analyzed with Leica software (Canella et al., 2018).

3.5.7. Cell migration assay

Cell migration assay was performed in 8 μm -pore size transwells (QCMTM 24-well Colorimetric Cell Migration Assay kit, Millipore, CA, USA) coated with 0.15 mg/ml bovine collagen IV. The lower chamber was filled with DMEM supplemented with 10% FBS and 1×10^4 cells were seeded in culture medium without FBS in the upper transwell containing treatment and incubated for 6 h. At each time point, transwell inserts were stained with Coomassie Blue Cell Stain solution for 15 min at RT, then rinsed with double-distilled H_2O . Cells in the upper compartment were removed with cotton swabs and pictures of five random fields were recorded using microscope. Number of cells migrated was quantified from images using the Analyze Particle tool in ImageJ.

The *in vitro* experiments were carried out in collaboration with Prof. Giuseppe Valacchi at the University of Ferrara and at the Plants for Human Health Institute of the North Carolina State University (USA), during my visiting research period.

3.6. EX-VIVO TESTS

3.6.1. Human skin explants (HSE) culture

Skin explants were prepared from the superfluous skin of healthy adult donors (18-60 years old). Breast or abdominal tissue specimens were obtained from patients undergoing plastic surgery. Skin biopsies (12 mm punches) were cultured into standard 6-well plates in contact with culture medium at 37°C in 5% CO₂ humidified air. The culture medium was Dulbecco's Modified Eagle Medium (DMEM) with 1% antibiotic-antimycotic solution (10.000 units penicillin, 10 mg streptomycin and 25 µg amphotericin B - Sigma-Aldrich, Germany) and 1% L-glutamine (Sigma-Aldrich, Germany) (Esposito et al., 2015b). After 1 day in culture, the medium was changed and HSE were topically treated with 50 µl of NLC T10 and NLC T10-TOC for 24h.

3.6.2. Cigarette smoke (CS) exposure

After 24h of treatment, the HSE were exposed for 30 minutes to CS generated by burning one research cigarette (12 mg tar, 1.1 mg nicotine) using a vacuum pump, as previously described (Muresan et al., 2018b). Control HSE were exposed to filtered air. After exposure, the explants were incubated in fresh media at 37°C in a humidified 5% CO₂ atmosphere for 24h.

3.6.3. Protein extraction

Samples for Western blot analysis were washed in PBS and frozen in liquid nitrogen. The biopsies were extracted in ice-cold using a tissue protein extraction reagent (T-PER buffer, Thermo Fisher Scientific, MA, USA) added of protease and phosphatase inhibitor cocktails (Sigma, Milan, Italy), using a bead-based homogenizer at 12400 rpm at 4°C for 15 min. Protein concentration was measured by Bradford method (BioRad, CA, USA) (Kulkarni, 2012).

3.6.4. Western blot analysis

Samples (25 µg protein) were loaded onto 10% sodium dodecyl sulfate polyacrylamide gel (SDS-PAGE) and then transferred onto nitrocellulose

membranes. Blots were blocked in PBS containing 0.5% Tween 20 and 5% not-fat milk (BioRad). Membranes were incubated overnight at 4°C with the appropriate primary antibody HO-1 (Abcam, Cambridge, UK). The membranes were then incubated with horseradish peroxidase-conjugated secondary antibody for 1 h at RT, and the bound antibodies were detected in a chemiluminescent reaction (ECL, BioRad). Chemiluminescence was detected on ChemiDoc imager (BioRad) (Muresan et al., 2018a). Blots were re-probed with β -actin as the loading control. Images of the bands were digitized, and the densitometry of the bands was performed using ImageJ software (Valacchi et al., 2017a).

The *ex-vivo* experiments were carried out at the Plants for Human Health Institute of the North Carolina State University (USA), collaborating with Prof. Giuseppe Valacchi during my visiting research period.

3.7. IN VIVO TESTS

3.7.1. Tape stripping

In vivo experiments were conducted in accordance with The Code of Ethics of the World Medical Association (Helsinki Declaration 1964) and its later amendments for experiments involving humans and was approved by the Ethics Committee of the University of Ferrara, Italy (study number: 161,087). The volunteers were of both sexes in the age range 25–55 years and recruited after medical screening, including the filling of a health questionnaire followed by physical examination of the application sites. Informed consent was obtained from all individual participants included in the study. The participants did not suffer from any ailment and were not on any medication at the time of the study. They were rested for 15 min prior to the experiments and room conditions were set at $22 \pm 2^\circ\text{C}$ and 40–50% relative humidity. For each volunteer, six sites on the ventral surface of forearms were defined using a rectangular template (2 cm²) and marked with permanent ink. Three sites were treated with 200 mg of SLN-PRG/G and three with 200 mg of NLC-PRG/G. The preparations were spread uniformly by means of a plastic spatula and then the sites were occluded for 6 h. After the occlusion period, the residual formulations were removed by gently wiping with clean cotton balls.

Eleven individual 2 cm² squares of adhesive tape (Scotch Book Tape 845, 3M) were utilized to sequentially tape-strip the stratum corneum on the application sites. The first tape strip was discarded and not analyzed, since it may still contain some formulation residue not removed by the skin cleaning. The stratum corneum was collected in the treated sites at 1 h (t 1), 3 h (t 3) and 6 h (t 6) from the formulation removal (Esposito et al., 2014). The presence of stratum corneum on the adhesive tapes was routinely checked by light microscopy using a Nikon E800, 40x magnification.

After stripping, all tapes from the same site were placed in a vial containing 2 ml of the HPLC mobile phase methanol:water (80:20 v/v) and vortexed for 1 min. The PRG present in the samples was then quantified by HPLC. The amount of PRG found in stratum corneum was plotted versus time and the area under the curve (AUC) was computed using the trapezoidal rule for comparison purposes. The employed software was Prism 5.0, Graph Pad Software Inc. (La Jolla, CA -304 USA), $p < 0.05$ was considered the minimum level of significance.

3.7.2. *In vivo* skin adhesion study

One healthy volunteer was enrolled to compare the skin adhesion of P15-CA and P15-HA2-CA. Briefly, 30 μ l of each formulation were applied on the ventral surface forearm. After application, the forearm was rotated about 90 degrees and held in a vertical position for about 10 seconds. The permanence of the gels in relation to the area of application was visually evaluated (Anirudhan et al., 2016).

4. PRODUCTION AND CHARACTERIZATION OF A CLOTRIMAZOLE LIOSPHERE GEL FOR CANDIDIASIS TREATMENT

4.1. INTRODUCTION

Candida albicans is a fungus able to locate in different host mucosal surfaces, standing both as a member of the normal microflora (yeast form) and a potential opportunistic pathogen (pseudohyphal form) (Mukaremera et al., 2017; Noverr and Huffnagle, 2004). The potential of *Candida albicans* to colonize various mucosal surfaces highly depends on the composition of the normal bacterial microflora. Particularly, the fatty acid environment produced by the host and bacterial microflora can influence and regulate germination of *Candida albicans* at mucosal surfaces (Ferrer, 2000; Zhu and Filler, 2010; Ravani et al., 2013). The proliferation of *Candida albicans* can generate symptomatic infections, such as vulvovaginal candidiasis, experienced at least once by 75% of women and repeatedly by 6-9% of women (Foxman et al., 2013).

Since local treatment is the first line of choice in cases of acute vaginal yeast infection, a variety of topical preparations are on the market, mainly containing azole fungistatic agents such as ketoconazole, miconazole and clotrimazole (CLO) (Figure 8) (Kyle and Dahl, 2004).

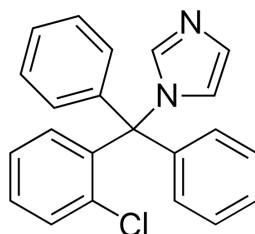


Figure 8: Chemical structure of Clotrimazole

However, the vaginal administration of these drugs as creams, gels, ovules and pessaries is often related to some drawbacks, such as leakage of the formulation and low residence time at the vaginal cavity (A. O. Andrade et al., 2014).

To solve these problems, a bioadhesive formulation should be able to increase the residence time of the dosage form and/or to enhance local bioavailability (Aka-Any-Grah et al., 2010; Santos et al., 2013). In addition, the inclusion of the antifungal agent into a solid microparticulate system could control its residence time and delivery. Among microparticulate systems, lipospheres (LS) represent an interesting choice. Being constituted of lipids, LS possess attractive properties such as biocompatibility and capacity to increase entrapment and bioavailability of poorly water-soluble drug.

In this part of my investigation, LS were especially designed for CLO delivery on vaginal mucosa to treat *Candida albicans* infection. CLO is widely employed to treat fungal infections topically, indeed oral administration of this active is not convenient, due to short half-life and side effects (Haller, 1985). Since CLO is a poorly water soluble drug, it requires a proper vehicle to rise effective right levels of topical absorption (Esposito et al., 2013). The lipid phase of LS was based on stearic triglyceride namely tristearin (TRIST), a solid lipid commonly employed in foods, and caprylic/capric triglyceride (TRIC) or the lactic acid derivative C₁₂-C₁₃ alkyl lactate (AL). These liquid auxiliary components have been employed in mixture with TRIST to possibly modulate and disorganize the ordered and compact solid LS microstructure. Indeed, it has been demonstrated that lipid carriers based on mixtures of solid and liquid lipids can encapsulate considerable amounts of drug, controlling its release and expulsion (Jenning et al., 2000; Nastruzzi, 2005). In addition, AL was chosen due the peculiar antimicrobial activity of lactic acid derivatives which can exert antifungal effect based on their ability to reduce pH of the milieu (Lind et al., 2005). To obtain adhesive formulations with suitable viscosity for vaginal application, lipospheres have been added to a hydrophilic gel constituted of the biopolymer xanthan gum, an anionic polysaccharide commercially obtained by bacterial fermentation (Witczak, 1997). Spreadability, leakage and adhesion were investigated *in vitro* to verify the suitability of the liposphere gel for vaginal administration.

The present results have been the object of the published paper: "Production and Characterization of a Clotrimazole Liposphere Gel for Candidiasis Treatment" [Esposito E., **Sguizzato M.**, Bories C., Nastruzzi C., and Cortesi R.. "Production and Characterization of a Clotrimazole Liposphere Gel for Candidiasis Treatment." *Polymers* 10, no. 2 (2018): 160. <https://doi.org/10.3390/polym10020160>].

4.2. RESULTS AND DISCUSSION

4.2.1. Liposphere production and characterization

A preformulation study was performed to investigate the effect of lipid composition on LS produced by melt dispersion technique (Cortesi et al., 2002). Particularly LS matrix was constituted of sole TRIST, or TRIST in mixture with the liquid auxiliary components TRIC and AL, as in *Table 8*.

Table 8: Composition of produced lipospheres in the preformulative study

Formulation	Composition (% w/w)			
	tristearin	caprylic/capric triglyceride	alkyl lactate	clotrimazole
LS _{TRIST}	100.00		-	-
LS _{TRIST/TRIC}	70.00	30.00	-	-
LS _{TRIST/AL30}	70.00	-	30.00	-
LS _{TRIST/AL15}	85.00	-	15.00	-
LS _{TRIST/AL10}	90.00	-	10.00	-
LS _{TRIST/AL1}	99.00	-	1.00	-
LS _{TRIST-CLO}	98.04		-	1.96
LS _{TRIST/TRIC-CLO}	68.69	29.35	-	1.96
LS _{TRIST/AL30-CLO}	68.69	29.35	-	1.96
LS _{TRIST/AL15-CLO}	83.34	-	14.70	1.96
LS _{TRIST/AL10-CLO}	88.24	-	9.80	1.96
LS _{TRIST/AL1-CLO}	97.06	-	0.98	1.96

The optimal AL concentration selected for LS production was 1% (w/w). Higher amounts of AL namely 10-30% w/w hindered LS formation, resulting in collapsed and aggregated particles. The aggregation phenomena could be attributed to interchain bonds between the AL alkyl chains located on the surface of these LS. Contrarily the presence of TRIC led to more regular and structured LS, probably due to the affinity between TRIC and TRIST.

Generally, recovery yields ranged between 80 and 97% w/w as compared to the total amount of lipid used for LS preparation, as described in *Table 9*.

Table 9: Liposphere mean diameter, recovery yield and clotrimazole encapsulation efficiency

Formulation	mean diameter (μm)	Yield (%) ^a	CLO EE (%) ^b
LS _{TRIST}	50 \pm 28	92.0 \pm 1	-
LS _{TRIST/TRIC}	6.3 \pm 8	88.3 \pm 2	-
LS _{TRIST/AL30}	n.d.*	80.0 \pm 1	-
LS _{TRIST/AL15}	n.d.*	86.0 \pm 2	-
LS _{TRIST/AL10}	n.d.	89.7 \pm 3	-
LS _{TRIST/AL1}	54.2 \pm 30	93.3 \pm 2	-
LS _{TRIST-CLO}	55.2 \pm 10	87.0 \pm 8	85 \pm 7
LS _{TRIST/AL10-CLO}	48.2 \pm 7	88.2 \pm 5	98 \pm 2
LS _{TRIST/AL1-CLO}	63.4 \pm 9	97.8 \pm 2	90 \pm 8

a: LS weight x 100/ total weight of lipids employed for LS preparation; b: amount of CLO detected by HPLC x 100 / total amount of CLO employed; *not determined

Regarding CLO encapsulation efficiency (EE), values ranged between 85 and 98% as compared to the total amount of CLO used (*Table 9*). As expected, AL presence permitted to increase CLO encapsulation in LS. Indeed it has been demonstrated that a binary mixture of two spatially different lipid matrices, i.e. a solid lipid and a liquid lipid (or oil) results in the formation of structured lipid carriers able to solubilize and encapsulate higher amount of drug with respect to the use of a single solid lipid (Jenning et al., 2000; Nastruzzi, 2005; Iqbal et al., 2012). The highest CLO EE value was achieved in the case of LS_{TRIST/AL10-CLO} (98%), nevertheless this type of LS was discharged because of aggregate formation.

Figure 9 SEM visualization enabled to observe that LS morphology is characterized by a spheroidal shape and mean diameters comprised between 6 and 75 μm . Moreover, the presence of aggregated LS is detectable.

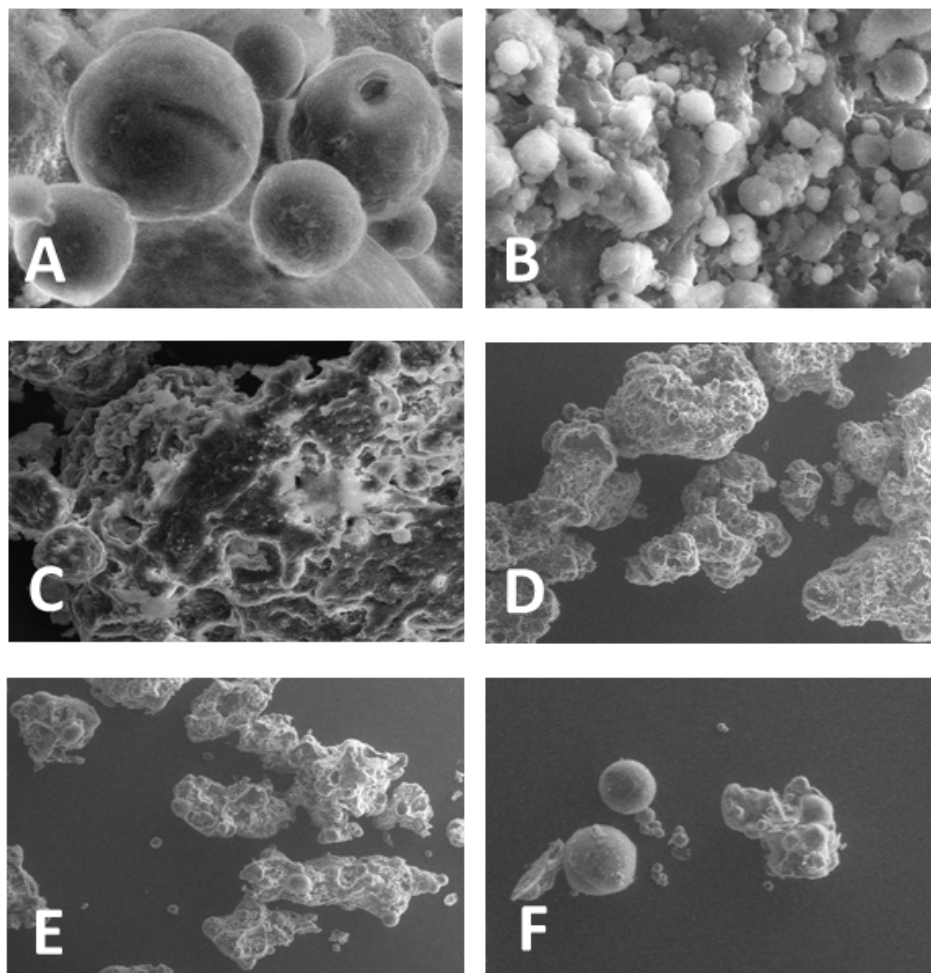


Figure 9: Scanning electron microscopy images of LS_{TRIST} (A), $LS_{TRIST/TRIC}$ (B), $LS_{TRIST/AL30}$ (C), $LS_{TRIST/AL15}$ (D), $LS_{TRIST/AL10}$ (E) and $LS_{TRIST/AL1}$ (F). Bar represents 20 μm in panels A, B and 50 μm in panels C-F

Particularly, LS_{TRIST} were spherical, with 50 μm mean diameter (Table 9 and Figure 9 A). The presence of TRIC (30% w/w) in mixture with TRIST ($LS_{TRIST/TRIC}$) maintained the LS spherical shape (Figure 9 B) and involved a drastic decrease of LS mean diameter (Table 9). Instead the addition of AL (30, 15 and 10 % w/w) to TRIST resulted in formation of collapsed and aggregated LS, with mean diameters difficult to measure (Figure 9 C-E, Table 9). On the other hand, a lower amount of AL (1% w/w) ($LS_{TRIST/AL1}$) allowed the formation of spherical LS with 54 μm mean diameter and few aggregates (Figure 9F, Table 9).

LS constituted of TRIST or TRIST/AL mixture (AL 1 and 10% w/w) were produced in the presence of CLO. Shape and mean diameter of $LS_{TRIST-CLO}$ and $LS_{TRIST/AL1-CLO}$ were almost unaffected by the presence of CLO (Figure 10 A, C and D, Table

9) showing spherical shape and mean diameters around 50 μm , while $\text{LS}_{\text{TRIST/AL10-CLO}}$ were in large part aggregated (*Figure 10 B*).

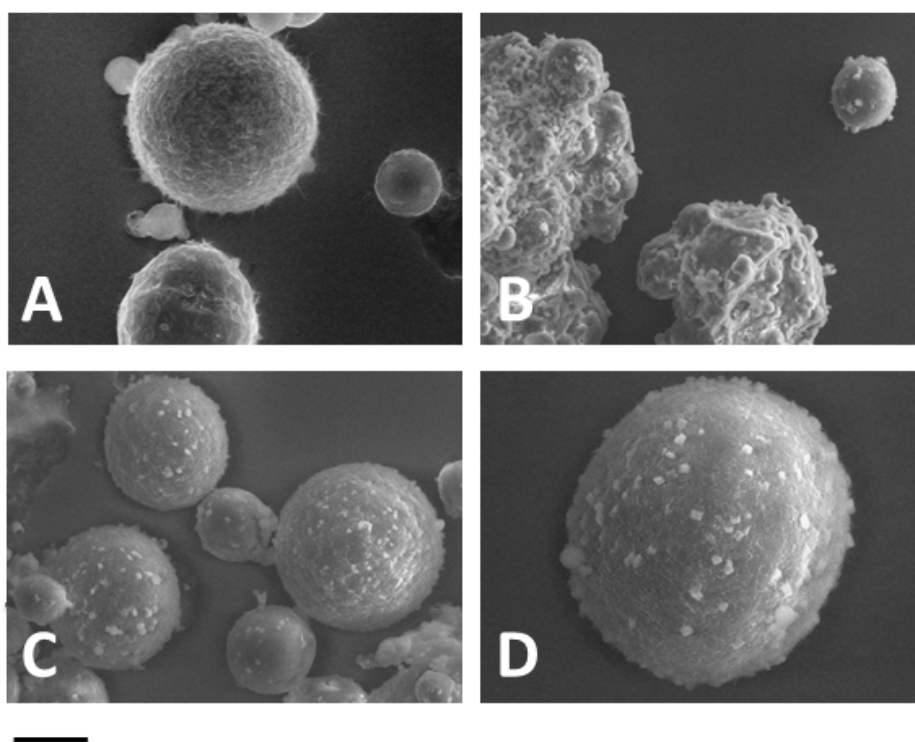


Figure 10: Scanning electron microscopy images of $\text{LS}_{\text{TRIST-CLO}}$ (**A**), $\text{LS}_{\text{TRIST/AL10-CLO}}$ (**B**) and $\text{LS}_{\text{TRIST/AL1-CLO}}$ (**C, D**). Bar represents 25, 50, 60 and 15 μm in panels A, B, C and D respectively

4.2.2. Anticandidal activity study

$\text{LS}_{\text{TRIST-CLO}}$, $\text{LS}_{\text{TRIST/AL1-CLO}}$ and the corresponding LS produced in the absence of CLO have been assayed against *Candida albicans* and the obtained minimum inhibitory concentration values (MIC) are summarized in *Table 10*.

Table 10: Minimum inhibitory concentration values (MIC, ng/mL) of clotrimazole-loaded lipospheres against *Candida albicans* ATCC 10231 strain

Formulation	MIC (ng/ml) \pm sd
$\text{LS}_{\text{TRIST-CLO}}$	23 \pm 1.6
$\text{LS}_{\text{TRIST/AL1-CLO}}$	17 \pm 1.4
LS_{TRIST}	no activity
$\text{LS}_{\text{TRIST/AL1}}$	no activity
CLO	32 \pm 2.3

A methanol solution of CLO has been employed as control. CLO containing LS displayed lower MIC values with respect to CLO solution, namely 1.4 and 1.9-lower than CLO for LS_{TRIST}-CLO and LS_{TRIST/AL1}-CLO respectively. In addition, in the case of LS_{TRIST/AL1}-CLO, MIC values were lower with respect to LS_{TRIST}-CLO. As expected, empty LS did not display anticandidal activity, confirming that LS did not exert intrinsic antifungal activity (Haller, 1985; Murgia et al., 2010; Garcia-Bennett, 2011). The differences between MIC values were statistically significant in the case of LS_{TRIST}-CLO versus LS_{TRIST/AL1}-CLO ($p < 0.05$) and high significant when both LS were compared to CLO ($p < 0.01$).

Summarizing, the encapsulation of CLO in LS improved its activity and on the other hand the combination of CLO and AL in LS further increased the anticandidal activity of CLO, supporting our hypothesis.

4.2.3. Production and characterization of Liposphere Gels

Since LS in their dry form can not be easily applied on mucosae, we firstly included them in a xanthan gum gel to obtain viscous formulations and then verified their suitability for vaginal administration. In *Table 11* the composition of the used gels is reported.

Table 11: Gel composition

Formulation	Gel components (% w/w)				
	tristearin	alkyl lactate	clotrimazole	xanthan gum	water
Gel LS _{TRIST} -CLO	4.902	-	0.098	0.500	94.500
Gel LS _{TRIST/AL1} -CLO	4.853	0.049	0.098	0.500	94.500
Gel-CLO	-	-	0.098	0.500	99.402
Gel _{AL1} -CLO	-	0.049	0.098	0.500	99.353

Taking into account the physiological vaginal pH (A. O. Andrade et al., 2014), we made choice to use citrate buffer pH 4 for dissolving xanthan gum with the aim to prevent pH variation of activity and applicability formulations. Moreover, the transparency of the obtained gel formulations enabled to verify the homogeneous distribution of LS within the gel.

i) Gel Viscosity

Formulation consistency is one of the most key features for application onto mucosae or skin, thus the gel viscosity plays a key role in drug permeation control (Karadzovska et al., 2013). The viscosities as a function of rotational speed of Gel LS_{TRIST/AL1}-CLO and Gel_{AL1}-CLO, are displayed in *Figure 11*. The behavior of Gel LS_{TRIST/AL1}-CLO and Gel_{AL1}-CLO was non-Newtonian shear thinning, indeed their viscosity decreased as the shear rate increased.

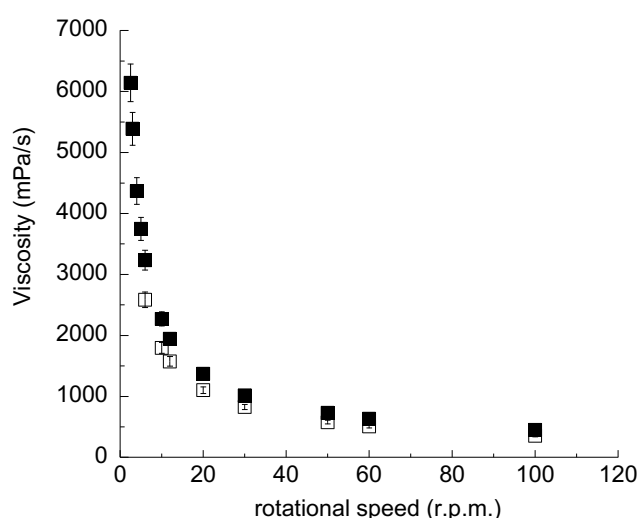


Figure 11: Viscosity of Gel LS_{TRIST/AL1}-CLO (■) and Gel_{AL1}-CLO (□) as a function of rotational speed. Data are the mean of three experiments and error bars represent standard deviation

This behavior suggests low flow resistance when applied at high shear conditions. The curves obtained for plain and LS containing gels were almost superimposable, indicating that the presence of LS slightly affected gel viscosity behavior.

This result suggests that the gel can be handled and, more importantly, it can easily coat the vaginal cavity, remaining in the application site without draining (A. O. Andrade et al., 2014; das Neves and Bahia, 2006), as demonstrated by the leakage experiment.

ii) Gel Spreadability

Spreadability is an important parameter for topical forms since it affects patient compliance, extrudability from the package, uniform application on skin or mucosae,

dosage transfer and finally therapeutic efficacy of the active molecule (Garg et al., 2002). As expected, LS presence in Gel LS_{TRIST/AL1}-CLO slightly decreased gel spreadability with respect to Gel_{AL1}-CLO, as shown in *Figure 12*. Namely, the spreadability ratio of Gel_{AL1}-CLO to Gel LS_{TRIST/AL1}-CLO was 1.4:1.

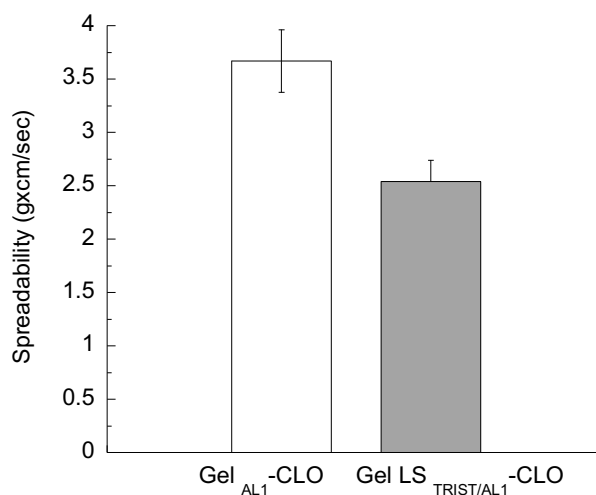


Figure 12: Spreadability behavior of the indicated gels

iii) Gel Leakage

Gel leakage potential from the vagina was explored. Indeed, it is known that a vaginal formulation should display a minimal leakage from the vaginal walls, thus a short running distance over the vertical plane, to assure a prolonged action (A. O. Andrade et al., 2014). Particularly, the running distance of Gel LS_{TRIST/AL1}-CLO, Gel_{AL1}-CLO and LS_{TRIST/AL1}-CLO are compared 1 min and 10 min after their application on vertical pH 4.5 agar slides based on SVF or citrate buffer.

The former slides have been especially designed to mimic pH and composition of the vaginal cavity, while the latter simulated only the vaginal pH. *Figure 13* shows the results of leakage test performed on agar slides and its quantification.

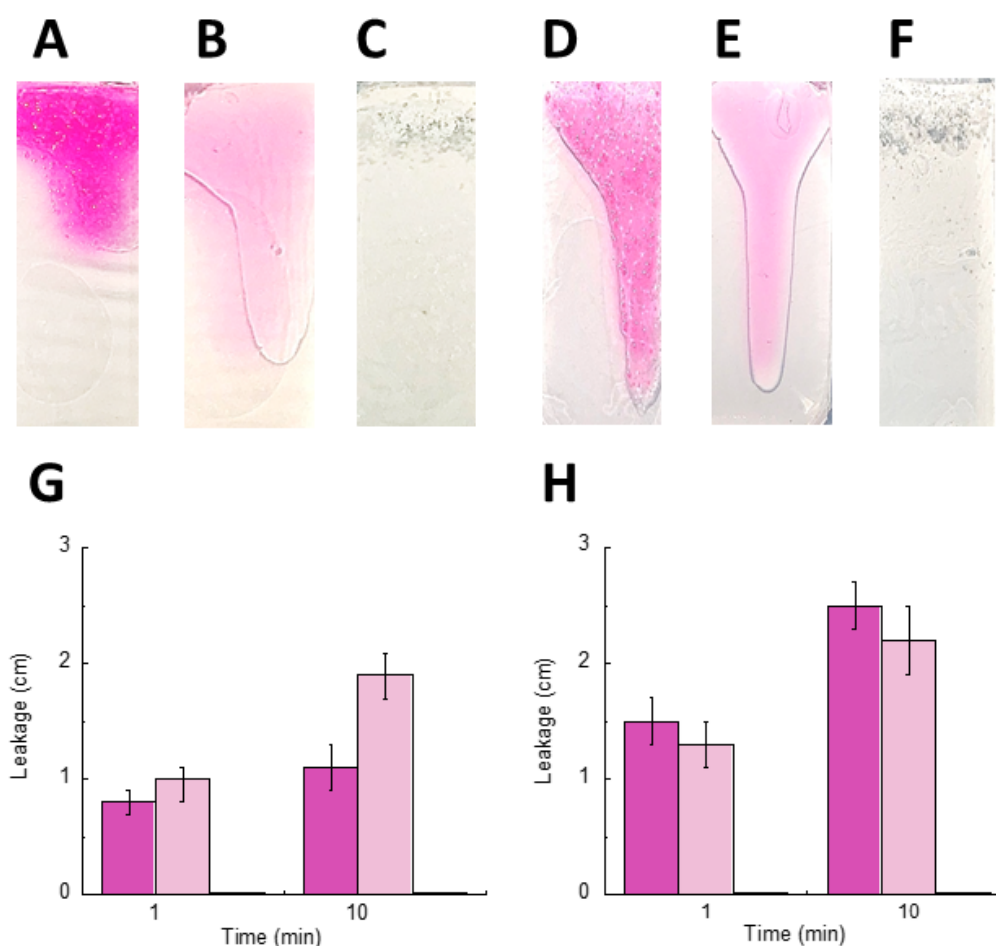


Figure 13: Comparative leakage test performed on formulations coloured by rhodamine for imaging. Namely Gel LS_{TRIST/AL1}-CLO (A, D), Gel_{AL1}-CLO (B, E) and LS_{TRIST/AL1}-CLO (C, F) were placed on pH 4.5 SVF (A-C) or citrate buffer (D-F) agar slides. Leakage distance was measured 1 and 10 min after application of Gel LS_{TRIST/AL1}-CLO (pink), Gel_{AL1}-CLO (light pink) and LS_{TRIST/AL1}-CLO on pH 4.5 SVF (G) or citrate buffer (H) agar slides. A-F images were taken 1 h after placing formulation on slides

In the case of application on SVF slides, the running distance of Gel LS_{TRIST/AL1}-CLO was minor than Gel_{AL1}-CLO, while, in the case of application on citrate buffer slides, the leakage trend was opposite. Namely, the leakage distance of Gel LS_{TRIST/AL1}-CLO applied on citrate buffer slides was almost double with respect to SVF ones. This behavior suggests an affinity of Gel LS_{TRIST/AL1}-CLO for SVF slides and thus for vaginal fluid composition, allowing us to conclude that the sole pH value is not enough to guarantee the permanence on vaginal mucosa. Dry LS remained fixed in the applied site on both type of slides even after 1 hour from placement, suggesting a high affinity for both pH and SVF composition.

iv) Gel Adhesion

Adhesion can be defined as the capability of a material to adhere to a mucosal surface. A high adhesion is required to accomplish retention of a pharmaceutical dosage form on the mucous membrane (Aka-Any-Grah et al., 2010; Boddupalli et al., 2010; A. O. Andrade et al., 2014). After testing gel leakage, the adhesion of Gel_{AL1}-CLO, Gel LS_{TRIST/AL1}-CLO or dry LS_{TRIST/AL1}-CLO was evaluated by comparing their residence time on agar slides immersed in pH 4.5 SVF or citrate buffer for predetermined length of time (*Figure 14*).

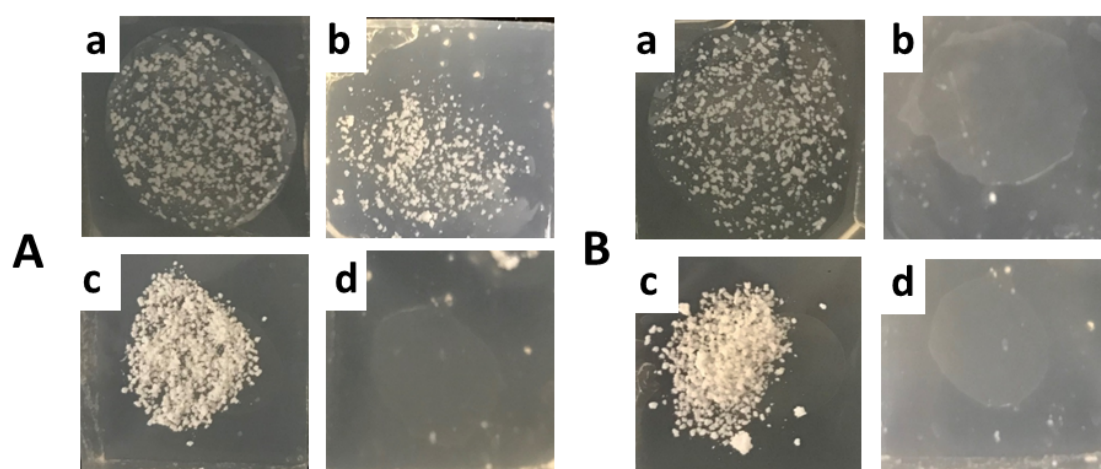


Figure 14: Comparative adhesion test performed on pH 4.5 SVF (**A**) or citrate buffer (**B**) agar plates immersed for 2 h in 10 ml of SVF or citrate buffer respectively. Images were taken 1 (a, c) or 120 (b, d) min after application of Gel LS_{TRIST/AL1}-CLO (a, b) and LS_{TRIST/AL1}-CLO (c, d)

After 2 h from immersion, the presence of LS was clearly detectable only in the case of Gel LS_{TRIST/AL1}-CLO applied on SVF agar slide (*Figure 14 A, panel b*). Indeed, only few LS were detectable in the case of citrate buffer agar slide (*Figure 14 B, panel b*), confirming the suitability of Gel LS_{TRIST/AL1}-CLO for vaginal application and contact with vaginal fluids. Two hours after placement of dry LS on SVF and citrate buffer agar slides, LS_{TRIST/AL1}-CLO were almost absent (*panels d of Figures 14 A and 14 B*), suggesting that the inclusion of LS in the gel is required to assure their adhesion. Images of Gel_{AL1}-CLO are not reported because the gel instantaneously dissolved after immersion in SVF or citrate buffer, indicating that LS presence was essential to achieve gel adhesion.

Leakage and adhesion results were in good agreement, both demonstrating the suitability of Gel LS_{TRIST/AL1}-CLO for vaginal application. In fact, this gel exhibited a minimal leakage and a long adhesion time when applied on SVF agar plate, mimicking the vaginal cavity.

4.2.4. *In Vitro* CLO Release Kinetics

To investigate and compare the performance of Gel LS_{TRIST/AL1}-CLO, Gel LS_{TRIST}-CLO, LS_{TRIST/AL1}-CLO and LS_{TRIST}-CLO as delivery systems for CLO, release profiles were determined *in vitro* by a dialysis method (Cortesi et al., 2002). The release kinetics, reported in *Figure 15*, were in general characterized by a biphasic profile in which CLO was initially released linearly, followed by a slower phase, in which the remaining drug was released.

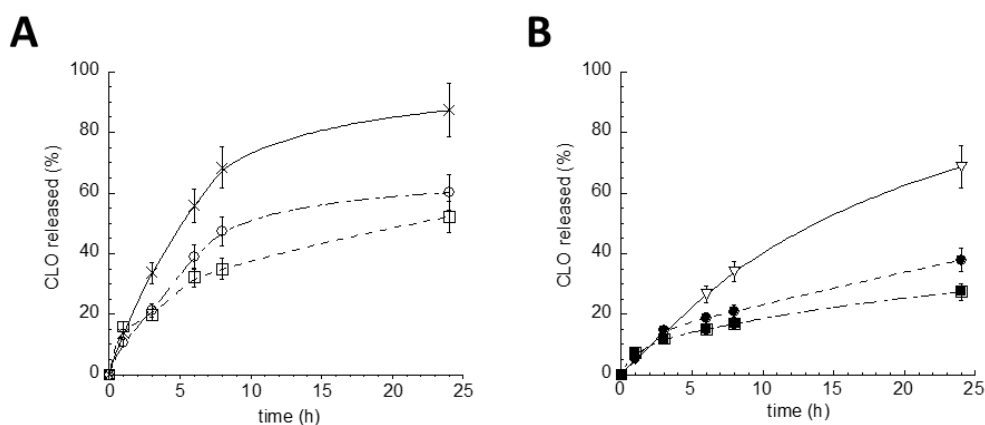


Figure 15: *In vitro* release kinetics of CLO from LS_{TRIST/AL1}-CLO (□), LS_{TRIST}-CLO (○) (A), Gel LS_{TRIST/AL1}-CLO (■), Gel LS_{TRIST}-CLO (●) (B). Experiments were performed by dialysis method. For comparison, the profiles obtained using CLO in aqueous (X) (A) or xanthan gum (▽) (B) dispersions are also reported. Data are the mean of 6 experiments ± sd

The encapsulation of CLO in LS or in gel enabled to slow down the drug release with respect to the aqueous dispersion (*Figure 15 A*) or the xanthan gum gel (*Figure 15 B*), employed as controls. As expected, the inclusion of LS_{TRIST/AL1}-CLO or LS_{TRIST}-CLO in gels delayed CLO release. In addition, the presence of AL (1% w/w) in the LS matrix enabled to better control CLO release, as can be noticed in the LS_{TRIST/AL1}-CLO and Gel LS_{TRIST/AL1}-CLO kinetics, with respect to their counterparts LS_{TRIST}-CLO and Gel LS_{TRIST}-CLO (*Figure 15 A,B*).

The control of CLO release should be attributed to (i) LS matrix, (ii) AL presence, and (iii) xanthan gum network, described by other authors as a biopolymer able to control drug release. Since LS are characterized by a matrix structure, as demonstrated by VPSEM observation, it can be hypothesized that a slow LS and gel dissolution in contact with vaginal fluids and a dissolution and diffusion of CLO first through LS and then through the gel network take place.

5. PROGESTERONE LIPID NANOPARTICLES: SCALING UP AND IN VIVO HUMAN STUDY

5.1. INTRODUCTION

Recent research efforts have demonstrated that nanotechnology achieves dramatic results in different scientific fields, including drug formulation and delivery. Particularly, the advantages of lipid based nanoparticles, namely solid lipid nanoparticles (SLN) and nanostructured lipid carriers (NLC), increase the ability to solubilize lipophilic drugs. Moreover, the variation of lipid composition offers the possibility to produce nanoparticles with different properties.

Hot homogenization technique is by far the most widely used nanoparticle production approach; the method is based on dispersion of a melted lipid phase in a hot aqueous surfactant solution under stirring by high-shear mixing device. The obtained emulsion is then submitted to hot homogenization and cooling, finally obtaining nanoparticles by re-crystallization of lipids (Dingler and Gohla, 2002; Müller et al., 2000).

The homogenization step is mandatory to reduce size of droplets constituting the inner oil phase of the initial emulsion. The homogenization can be achieved by ultrasound, or by high pressure. Ultrasound homogenization (UH) is based on the transmission of high power ultrasound waves in a liquid media by a probe.

High pressure homogenization (HPH) is an ongoing process widely used in pharmaceutical and food industry, based on reduction of droplet/particle size and uniformity under conditions of extreme pressure by a piston-gap homogenizer.

Notwithstanding its high cost, high-pressure homogenizer lab-scale and pilot-scale models can operate with limited sample volumes and produce the same results as large models, ensuring scalability of results. Thus, HPH enables to scale-up nanoparticle volume from lab to pilot and industrial scale (Das and Chaudhury, 2011; Uner, 2006).

Progesterone (PRG) (*Figure 16*) is a steroid hormone present in different medicines with various indications such as the control of habitual abortion, suppression and synchronization of oestrus, regulation of ovulation and menstruation (e.g. to treat amenorrhoea), treatment of infertility by luteal phase support and prevention of

endometrial hyperplasia (Lockwood et al., 2014; Tavaniotou et al., 2000). For these applications, PRG is typically administered orally, rectally, intramuscularly, subcutaneously or intravaginally (Lockwood et al., 2014; Tavaniotou et al., 2000). In addition, PRG is included in cutaneous formulations (i.e. gels and creams) to treat dermatological disorders such as acne and ageing (Burry et al., 1999; Holzer et al., 2005).

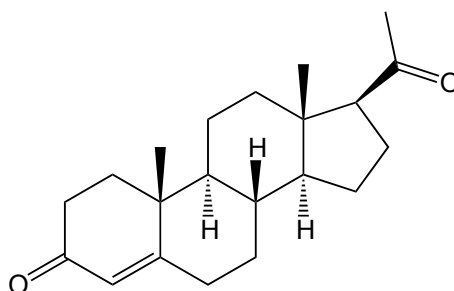


Figure 16: Chemical structure of Progesterone

In this respect, this investigation describes a scaling up study aimed at producing PRG containing nanoparticles in a pilot scale produced by UH and HPH methods. These two techniques have been investigated and compared, in order to produce nanoparticles without agglomerates, with smaller mean diameters, great stability and high encapsulation efficiency. Dialysis and Franz cell methods were performed to mimic subcutaneous and skin administration *in vitro*. The obtained nanoparticle suspensions were further viscosized by xanthan gum (x-gum) addition. A human *in vivo* study, based on tape stripping, has been conducted to compare the performances of SLN and NLC gels applied on skin. Particularly PRG amount in *stratum corneum* has been evaluated after cutaneous application of the different nanoparticulate gels.

The present results have been the object of the published paper: “Progesterone lipid nanoparticles: Scaling up and in vivo human study” [Esposito E., **Sguizzato M.**, Drechsler M., Mariani P., Carducci F., Nastruzzi C., and Cortesi R. “Progesterone Lipid Nanoparticles: Scaling up and in Vivo Human Study.” *European Journal of Pharmaceutics and Biopharmaceutics* 119 (2017): 437–46. <https://doi.org/10.1016/j.ejpb.2017.07.015>].

5.2. RESULTS AND DISCUSSION

5.2.1. Effect of experimental set up on lipid nanoparticles

Scalability of lipid nanoparticle production from bench to pilot and large scale represents an important challenge in view of industrial production (Paliwal et al., 2014). Since production methods and conditions affect physico-chemical characteristics of the nanoparticles, specific studies are needed to achieve the highest product quality.

In this respect in the current chapter we have evaluated the effect of HPH process parameters on nanoparticle characteristics.

Most of the experimental procedures for the preparation of lipid nanoparticles intended as solid lipid nanoparticles (SLN) or nanostructured lipid carriers (NLC) are characterized by small amount of lipid (80-250 mg) dispersed in a 5-50 ml water phase (Esposito et al., 2008; Pooja et al., 2015; Yuan et al., 2007). Particularly, HPH method was compared with UH protocol, that was previously studied by our research group (Esposito et al., 2017a, 2017b, 2016a, 2015a).

Therefore, SLN and NLC have been prepared by UH and HPH methods. The methods require two steps; the first one is common to both procedures and is represented by an emulsification conducted by high-shear mixing. In the second step, the obtained emulsion is treated by two alternative instruments, with the aim to reduce and uniform the droplet size: (a) in the UH method by a probe ultrasound generator and (b) in the HPH method by a high-pressure homogenizer.

The initial emulsion was obtained by dispersing the fused lipids in the aqueous surfactant solution under high speed stirring at 15000 r.p.m. for 1-3 min.

Varying the emulsification time (in the 1-3 min range) caused only marginal variations in mean diameter of the obtained particles (data not shown). Therefore, to shorten the preparation time and save energy in view of an industrial production, the high-shear emulsification step was limited to 1 min.

With respect to the UH step, the influence of the treatment length was investigated on particle size; SLN and NLC dimensions were determined after treatment of 5, 10 and 15 min (*Table 12*).

Table 12: Mean diameters of nanoparticles as a function of process parameters

Process parameters	Z average mean diameter (nm)	
	SLN	NLC
<i>Duration of UH (min)</i>		
5	200 ± 33	255 ± 45
10	180 ± 28	230 ± 33
15	147 ± 52	179 ± 55
<i>HPH (number of cycles)</i>		
1	68 ± 15	86 ± 18
2	88 ± 17	102 ± 20
3	99 ± 28	112 ± 14

Data are the mean of 4 determinations in independent experiments ± sd

In further experiments, the 15 min UH treatment was selected, since it allowed the production of the smallest nanoparticles (147 and 179 nm for SLN and NLC, respectively), as compared to the others length of UH treatment.

For the HPH method, the effect of number of homogenization cycles was investigated on nanoparticle size. As reported in *Table 12*, mean diameter of SLN and NLC was affected by the number of homogenization cycles. Surprisingly, the smallest dimensions were obtained using a single cycle, therefore in view of scaling up the production procedure, the single homogenization cycle was selected.

In the case of HPH method, the influence of pressure was also considered, namely the range 40-120 MPa was investigated (data not shown). Pressure level from 40 to 100 MPa decreased the size, while higher pressures, up to 120 MPa increased the particle dimension. This behavior was attributed to particle coalescence induced by high kinetic energy of particles. To limit this phenomenon, pressure was set at 100 MPa.

Taken together, the data obtained from the analysis of UH and HPH methods resulted in the selection of the set-up for both methods, summarized in *Table 13*.

It has to be underlined that, HPH method enabled to 20-fold increase production volume of nanoparticle with respect to UH. Indeed, by HPH it was possible to obtain 1 liter of nanoparticles dispersion corresponding to a lipid amount of 50 g.

Table 13: Experimental set-up for nanoparticle production

<i>method</i>	First step	Second step	
		<i>Duration</i>	<i>Energy input</i>
UH	1 min high shear homogenization	15 min	6.75 Hz
HPH	1 min high shear homogenization	1 cycle	100 MPa

5.2.2. Nanoparticles characterization

The effect of production method and of the presence of PRG has been evaluated with respect to nanoparticle dimensions, presence of agglomerates, EE and LC. All these data are summarized in *Table 14*.

Table 14: Dimensional characteristics and encapsulation parameters of nanoparticles produced by UH or HPH method

Nanoparticle type	UH				HPH			
	SLN	SLN-PRG	NLC	NLC-PRG	SLN	SLN-PRG	NLC	NLC-PRG
Z average (nm)	147 ± 52	216 ± 22	179 ± 55	125 ± 10	68 ± 15	181 ± 14	86 ± 18	137 ± 18
Dispersity	0.26	0.35	0.27	0.22	0.30	0.31	0.22	0.25
Agglomerate^a (%)	6 ± 3.5	8 ± 2.2	5 ± 3.8	7 ± 2.3	-	-	-	-
EE^b (%)	-	82 ± 4	-	88 ± 10	-	97 ± 2	-	99 ± 1
LC^c (%)	-	1.64	-	1.76	-	1.94	-	1.98

Data represent the mean ± sd of 6 independent experiments.

a: loss of lipids (lipid phase) due to the partial coalescence of the lipid phase during the formation of the O/W emulsion. After cooling the coalesced lipid phase appeared as a small flake floating on the surface of the NLC dispersion; b: percentage (w/w) of PRG with respect to the total amount used for the preparation; c: percentage (w/w) of PRG with respect to the amount of lipid used for the preparation

Dimensions were measured by PCS and expressed by Z average. Data reported in *Table 14* indicate that: (i) nanoparticles produced by HPH have consistently smaller dimensions than those produced by UH; indeed, the former are comprised between

68 and 181 nm while the latter span between 125 and 216 nm, (ii) the Z Average diameters of NLC-PRG are smaller than those of SLN-PRG, particularly in the case of nanoparticles produced by UH and (iii) the presence of PRG appears to have an important effect on nanoparticles size; both methods resulted in drug loaded nanoparticle with larger dimensions with respect to the empty counterparts.

Regarding agglomerates, SLN and NLC produced by UH method displayed a presence of 5-8 % agglomerate, on the contrary with the HPH method, no agglomerates were detected.

EE and LC values, reported in *Table 14*, revealed that both methods gave rise to high EE (higher than 82%) and LC (higher than 1.64%). For instance, PRG encapsulated in lipid nanoparticles produced by HPH was generally stable, even if NLC resulted in a superior stability with respect to SLN (Pardeike et al., 2009).

5.2.3. Morphological analyses of lipid nanoparticles

The morphology of SLN and NLC produced by HPH has been investigated by cryo-TEM and x-ray diffraction. It is important to underline that nanoparticles imaged by cryo-TEM visualizations appear different depending on their orientations. Generally, in the case of top view, both SLN and NLC display a low electron dense discoid structure; while in the case of edge-on view they appear as high electron-dense rod like structures (*Figure 17 A, B*). This feature is well detectable in the microphotographs relative to the SLN samples (*Figure 17 A, C*), in which the edge-on viewed nanoparticles have an electron dense rod-shape morphology, without any appreciable structured architecture (at least in the cryo-TEM analysis). On the contrary, NLC display a different internal organization; particularly in the edge-on view, they are characterized by the presence of stacked lamellae capped by semi-elliptical structures (*Figure 17 D*). Importantly, (a) the presence of the drug does not alter the morphology of both SLN and NLC (see insets in *Figure 17 C, D*) and (b) the general morphology of nanoparticles produced by HPH is almost identical to that of nanoparticles produced by UH (images not shown) (Esposito et al., 2017b).

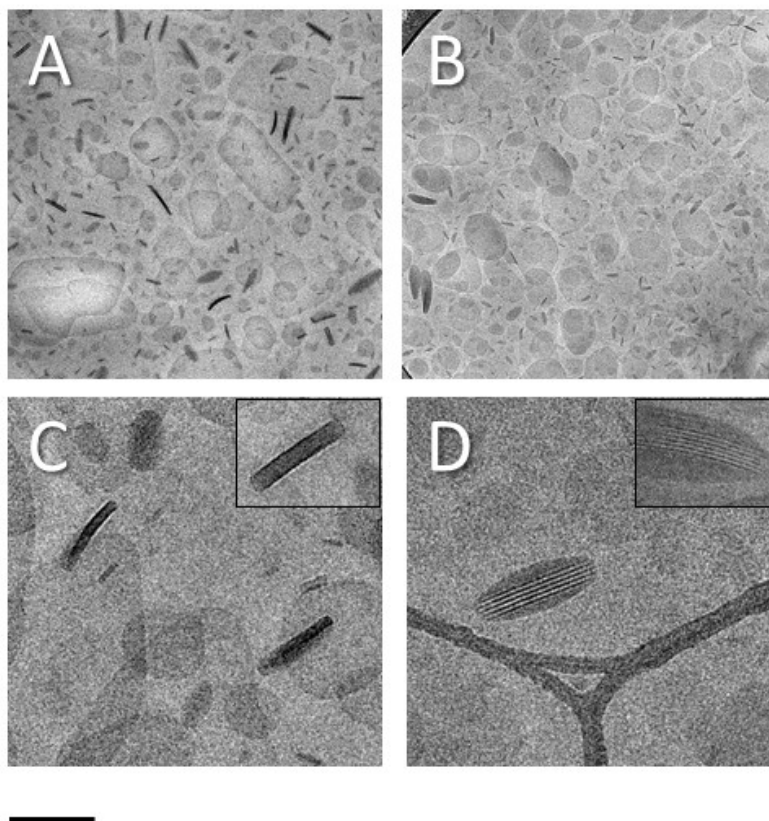


Figure 17: Cryo-TEM images of lipid nanoparticle produced by HPH method, containing PRG. SLN-PRG (**A, C**) and NLC-PRG (**B, D**) are imaged at low (**A, B**) or high magnification (**C, D**). For comparison in the insets of panels C and D the microphotographs relative to empty SLN and NLC are also reported. Bar corresponds to 300 nm in panels A and B and 150 nm in panels C and D

Nanoparticles produced by HPH have been further characterized by X-ray diffraction analyses. The low-angle region was considered to investigate the structure of SLN, NLC, SLN-PRG and NLC-PRG. The results are reported in *Figure 18*, showing that both SLN and NLC display an internal lamellar organization; the calculated unit cell values were 4.52, 4.6, 4.55 or 4.75 nm, for SLN, SLN-PRG, NLC and NLC-PRG respectively. Data indicate that the presence of PRG slightly increased the unit cell dimensions in both type of lipid nanoparticles.

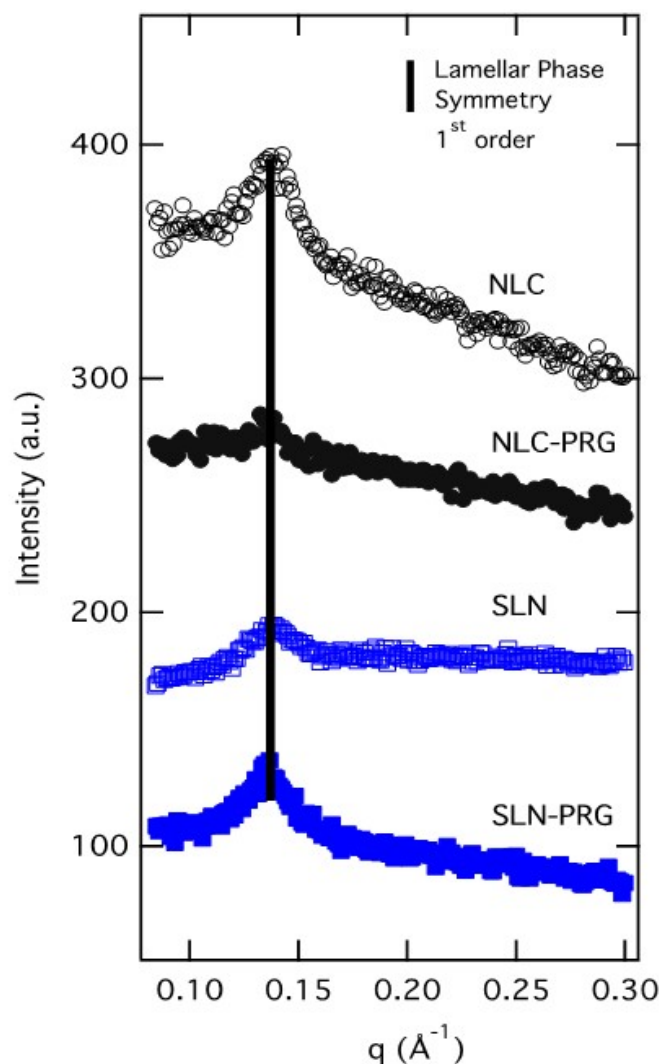


Figure 18: X-ray diffraction profiles observed for SLN and NLC, in the presence and absence of PRG. From the bottom: SLN-PRG, SLN, NLC-PRG and NLC. The vertical black line indicates the peak position of the first order of the Lamellar Phase Symmetry. Nanoparticles were produced by HPH method

5.2.4. Stability studies

In view of an industrial application, specific studies have been undertaken comparing nanoparticles produced by HPH and UH. Particularly, physico-chemical studies have been conducted, to determine the dimension (expressed as Z Average) and the stability of PRG up to 6 months from the production.

The dimensional results show that lipid nanoparticles were quite stable in term of size, since the formulations produced by both methods maintained their dimensions almost unvaried during the 6 months period analyzed (*Figure 19 A, B*).

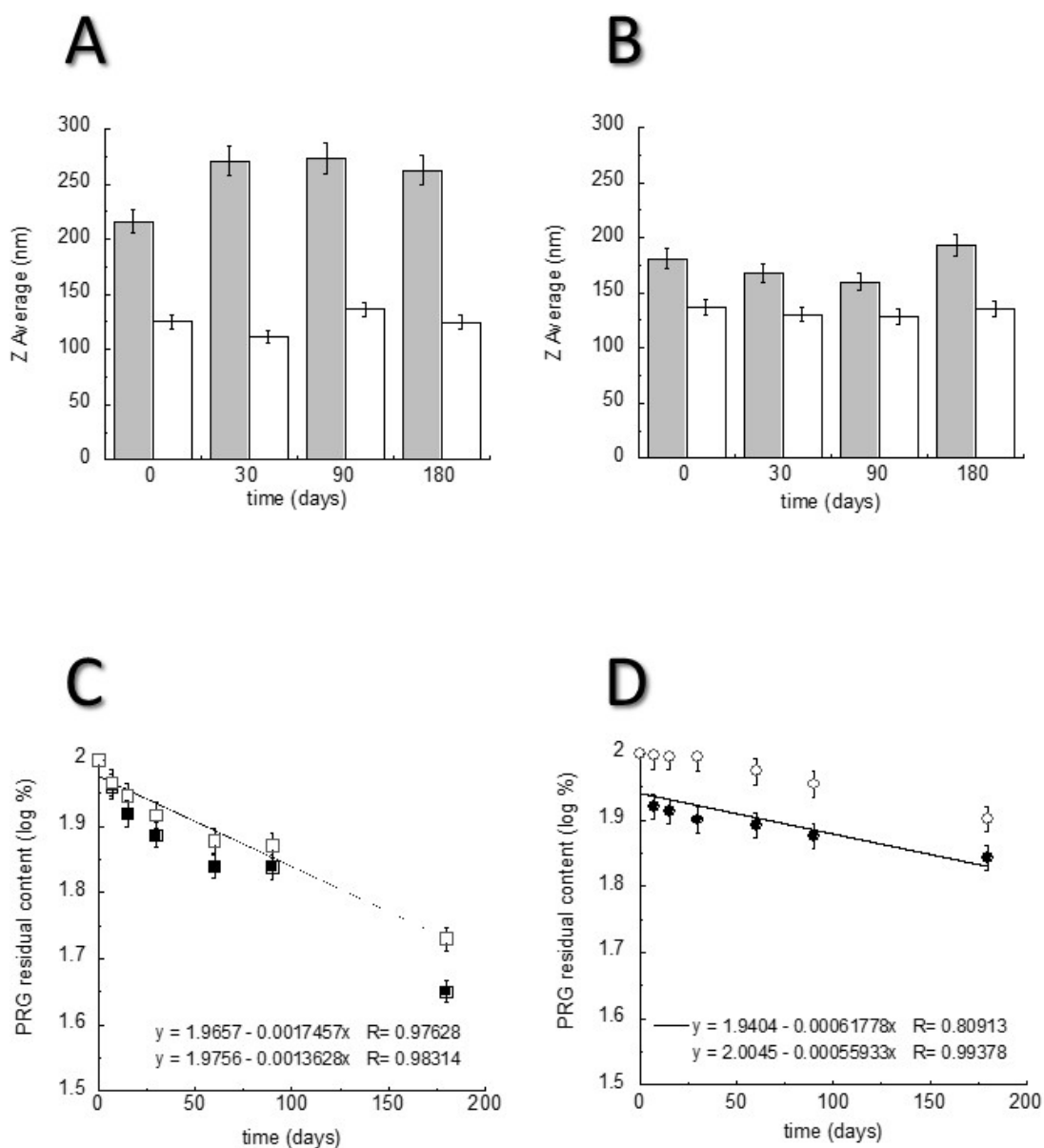


Figure 19: Effect of aging on Z Average (**A, B**) and PRG content (**C, D**) of lipid nanoparticles. SLN-PRG (filled symbols) and NLC-PRG (empty symbols) were produced by UH (**A, C**) or HPH (**B, D**) methods. The formulations were stored in glass containers at 25°C for 3 months. Data are the mean of 5 analyses on different batches of the same type of formulations

To investigate the stability of drug in nanoparticle formulations, PRG content has been determined as a function of time and expressed as percentage with respect to the total amount of drug loaded in the formulation. From the data reported in *Figure 19*, it is evident that the drug in NLC-PRG was more stable with respect to that in SLN-PRG. Regarding the production method, nanoparticles produced by HPH were quite stable than those produced by UH. Particularly, in the case of NLC-PRG

produced by HPH and UH, PRG residual content after 6 months was 80% and 66% respectively.

Table 15 reports shelf life (t_{90}) and half-life ($t_{1/2}$) values calculated by equations (5) and (6). The longest shelf life values were found in the case of NLC-PRG produced by HPH. Notably SLN-PRG and NLC-PRG produced by this method displayed t_{90} and $t_{1/2}$ values respectively 3-fold and 2.5-fold longer with respect to nanoparticles produced by UH method.

Table 15: Shelf life values of nanoparticles produced by UH method or HPH method

Parameter	Nanoparticles produced by UH		Nanoparticles produced by HPH	
	SLN-PRG	NLC-PRG	SLN-PRG	NLC-PRG
K	0.004	0.0031	0.0014	0.0012
t_{90} (days)^a	26.11	33.87	73.80	81.51
$t_{1/2}$ (days)^b	173.25	223.54	495.00	577.50

The reported results represent the average of 4 independent experiments \pm SD

a: Time at which the drug concentration has lost 10 % with respect to drug recovery at 0 day;

b: Time at which the drug concentration has lost 50 % with respect to drug recovery at 0 day

5.2.5. *In vitro* PRG release kinetics

PRG release profiles from nanoparticles produced by HPH were determined *in vitro* by a dialysis method. Namely SLN-PRG and NLC-PRG were compared; as reference a free drug formulation based on a suspension of the drug in poloxamer 188 (2.5 % w/w in water) was taken.

The release of PRG from the different formulations are reported in *Figure 20*. In all cases the obtained profiles are similar in term of general shape. They are characterized by an initial phase in which 50-60% of the PRG is released, afterwards PRG is released much more slowly. In addition, the obtained data indicate that PRG is more slowly released from NLC-PRG. All considering, in the case of SLN-PRG a fickian diffusive mechanism has been postulated, while a combination of dissolutive and diffusive mechanism has been supposed for NLC-PRG.

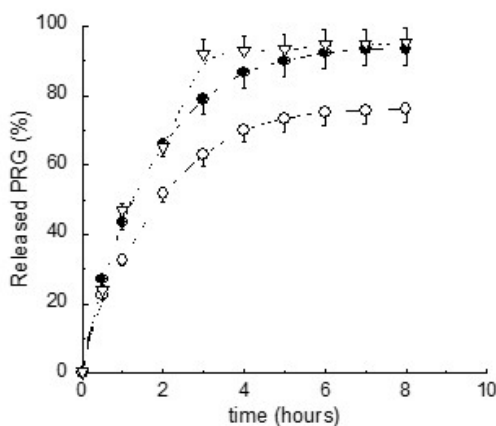


Figure 20: *In vitro* release kinetics of PRG from SLN-PRG (●), NLC-PRG (○) and poloxamer 188 suspension (2.5% w/w) (▽). Experiments were performed by dialysis method. Data are the mean of 6 experiments \pm S.D

5.2.6. $!(\%)^{*+,-}$ skin permeability of nanoparticles

In view of vaginal or cutaneous administration of nanoparticles, a thickened formulation would be required since the low viscosity of SLN and NLC aqueous suspensions do not allow the proper application. Therefore, to produce a semisolid formulation containing PRG nanoparticle, the aqueous nanoparticle suspensions were thickened by direct addition of x-gum powder (to a final 1% w/w concentration). X-gum enabled to rapidly obtain gelled formulations, named SLN-PRG/G and NLC-PRG/G.

The skin permeability of PRG included in SLN-PRG/G and NLC-PRG/G was investigated by Franz cell experiments using SCE. To ensure sink condition, a receptor phase constituted of a water/ethanol 1:1 (v/v) mixture was used (L. M. Andrade et al., 2014; Touitou and Fabin, 1988). It should be considered that Franz cell represents an *in vitro* model which is a reconstruction of the biological environment, mimicking application on SCE membrane, without taking in consideration the full skin and the physiological distribution of PRG through blood capillaries in the dermis (Hazama et al., 2016).

Drug permeability and skin uptake were evaluated analyzing PRG content in the receptor phase and in the SCE. The results of skin permeability experiments indicate that PRG content in the receptor phase was below the detection limit of the analytical method employed. This finding corroborates the idea that PRG, being a lipophilic molecule, is strongly associated to the lipid matrix of the nanoparticles.

The analysis of the PRG content in SCE, reported in *Figure 21*, demonstrated that after 6 h similar amounts of PRG were present in the case of SLN-PRG/G and NLC-PRG/G. After 24 h the presence of PRG in SCE was statistically higher ($p < 0.001$) in the case of SLN-PRG/G with respect to NLC-PRG/G (1.5-fold higher), probably because of a higher affinity and better accommodation of PRG in the liquid phase of NLC (Küchler et al., 2009).

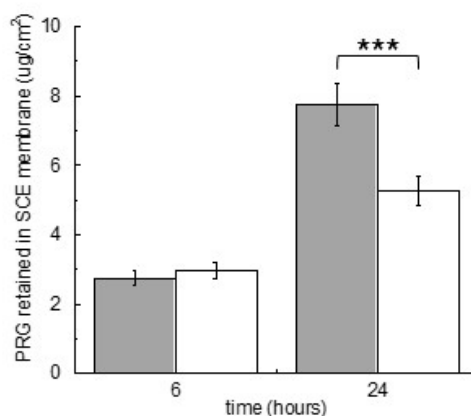


Figure 21: PRG skin uptake in SCE membrane from SLN-PRG (filled), NLC-PRG (empty) after 6 and 24 h of permeation experiments in Franz diffusion cells ($n = 6$); error bars represent the standard deviations; *** $p < 0.001$. Nanoparticles were produced by HPH method

NLC appear as vehicle able to better retain PRG within lipid matrix with respect to SLN.

5.2.7. Tape-stripping experiments

To overcome the above described limits of the Franz cell method and to investigate more accurately the performances of lipid nanoparticle formulations applied on the skin, *in vivo* experiments were performed. Tape stripping allowed to directly quantify PRG in the stratum corneum after application of the gelled nanoparticle formulations. After application of nanoparticle formulations on skin, the amount of PRG in stratum corneum was assessed to compare the performances of SLN-PRG/G and NLC-PRG/G (Esposito et al., 2014).

Experiments were carried out as schematized in *Figures 22 A-F*. *Figure 22 G* and *Table 16* show the amount of PRG present in stratum corneum after application of the different formulations and the relative AUC values, respectively.

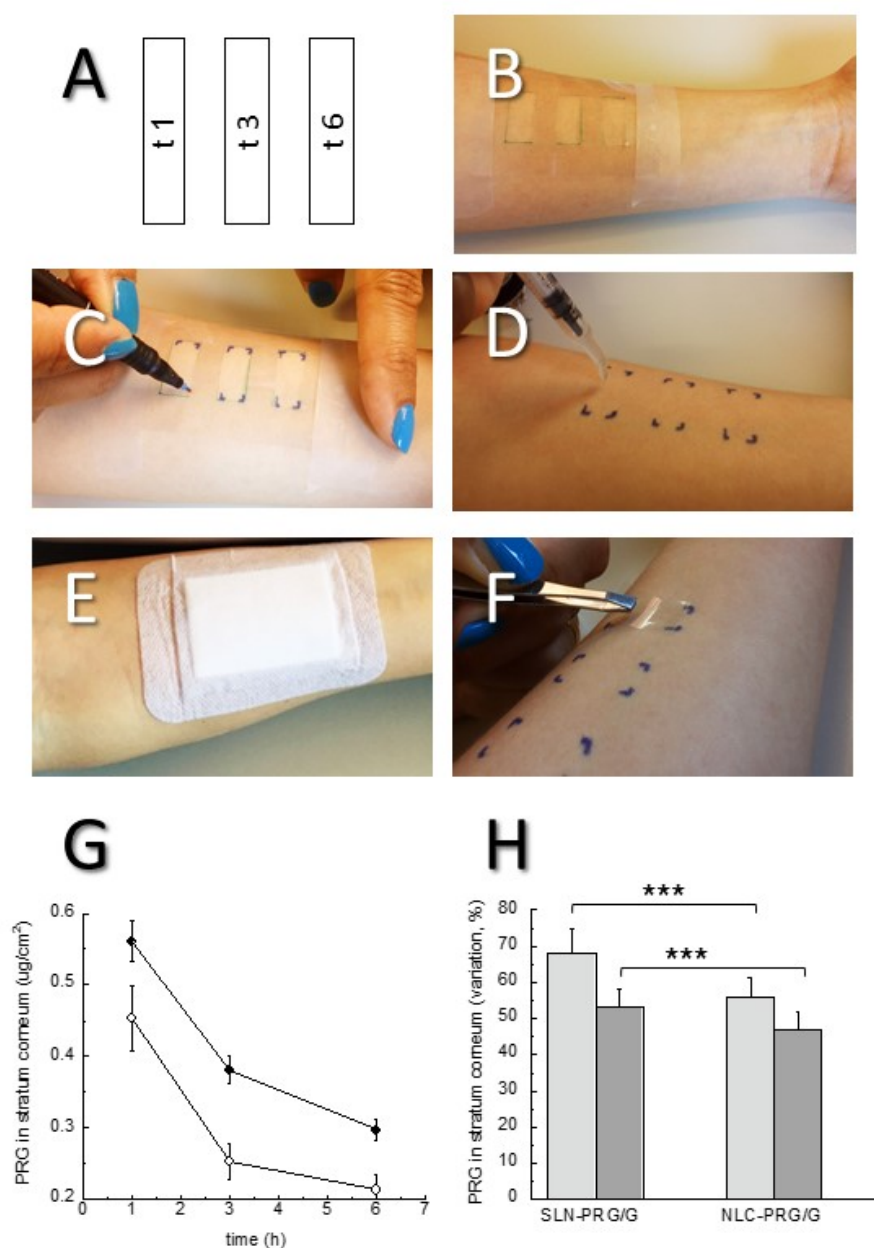


Figure 22: Tape-stripping experiment on lipid nanoparticle gels. Time setting (A) and major steps of the tape-stripping experiments; application of a plastic mask on the internal forearm (B), marking of the application sites by permanent ink pen (C), application of the gels by needleless syringe (D), application of backing (E) and removal of stratum corneum layer by tape-stripping (F). Analysis of PRG amount in stratum corneum after application of SLN-PRG/G (●) and NLC-PRG/G (○) (G). Formulations were maintained on the skin for 6 h, thereafter the PRG amount was measured at the indicated lengths of time. Comparative evaluation of the PRG level present at t 3 (light bars) and t 6 (dark bars) in stratum corneum, as determined by tape-stripping experiments; the reported levels represent the percentage of PRG with respect to that present in stratum corneum at t 1 (H). Data represent the mean of 10 subjects \pm SD, *** $p < 0.001$. Nanoparticles were produced by HPH method

Figure 22 G shows that, at t 1 from removal of the formulations, the amount of PRG in stratum corneum was higher for SLN-PRG/G than NLC-PRG/G, possibly due to a more pronounced occlusive effect induced by the solid nanoparticles (Uner and Yener, 2007). Probably part of nanoparticles remained intact on the skin surface, while another fraction penetrated the *stratum corneum* lipids (L. M. Andrade et al., 2014; Khurana et al., 2013; Teeranachaideekul et al., 2008). The difference in PRG content was confirmed at observation made at t 3 and t 6, as clearly appreciable from the AUC value reported in Table 16. For all the time intervals considered (t 1-3, 3-6 and 1-6), the content of PRG, expressed as AUC, follows the order SLN-PRG/G > NLC-PRG/G. All differences were statistically significant ($p < 0.001$).

Table 16: AUC values calculated after tape stripping experiments

Formulation	AUC t 1-3	AUC t 3-6	AUC t 1-6
SLN-PRG/G	0.94	1.05	1.99
NLC-PRG/G	0.70	0.69	1.39

AUC values were calculated from the plot relative to the amount of PRG in *stratum corneum* versus time (Figure 22G)

Finally, Figure 22 H shows that PRG values at t 3 and t 6 (expressed as percentage of PRG with respect to those found at t 1) display a similar depletion effect (i.e. the reduction of PRG content in stratum corneum with time).

It has been reported that lipid nanoparticles applied on skin can interact with stratum corneum constituents in reason of their lipophilic molecule composition, nanoscale dimensions and bioadhesive properties (Pardeike et al., 2009; Wissing et al., 2001). The skin absorption of drug delivered by lipid nanoparticle is in addition facilitated by an occlusive effect, skin hydration and a drug penetration enhancement due to the components of nanoparticles (i.e. short- medium-chain triglycerides) (Lippacher et al., 2002; Uner, 2006; Wissing et al., 2001). Some authors suggested that nanoparticle smaller than 200 nm form a monolayer on the skin surface, favoring skin moisture, open intercorneocyte spaces and promotes drug penetration into deeper layers of the skin, through the transappendageal pathway (Uner and Yener, 2007; Wissing and Müller, 2003). In this respect, tape stripping experiments indicate that PRG penetrated into stratum corneum and deeper skin layers.

6. PRODUCTION AND CHARACTERIZATION OF NANOPARTICLE BASED HYALURONATE GEL CONTAINING RETINYL PALMITATE FOR WOUND HEALING

6.1. INTRODUCTION

Wound healing is a biological process consisting of four phases (i.e. hemostasis, inflammation, proliferation, and tissue remodelling) (Heng, 2011). In some cases, associated for instance to stress, smoke, alcohol consumption, ischemia or diabetes mellitus, impaired wound healing can occur, preventing the normal development of healing process (Guo and Dipietro, 2010). Thus, wounds can get in a state of pathologic inflammation, requiring the use of specific medications able to promote proper tissue repair and to improve impaired wound healing (Bishop, 2008).

The aim of the present study was the design and the production of a nanoparticulate based gel suitable for wound healing. Particularly we hypothesized the possibility to include in the same product hyaluronic acid (HA) (*Figure 23A*) and the vitamin A derivative retinyl palmitate (RP) (*Figure 23B*), in order to obtain a synergic wound healing effect.

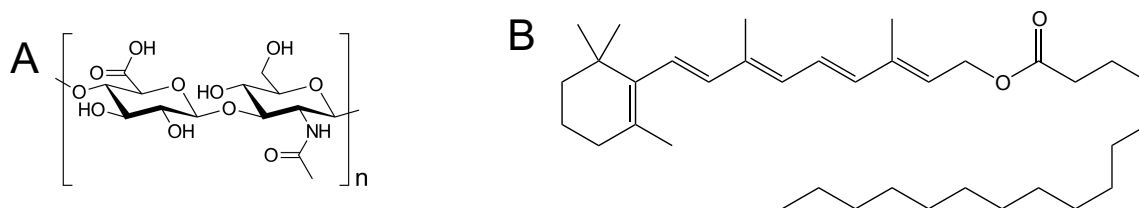


Figure 23: Chemical structure of Hyaluronic Acid (A) and Retinyl palmitate (B)

HA is a ubiquitous component of the extracellular matrix, therefore present in connective, epithelial, and neural mammalian tissues. It plays a role in different physiological processes like maintenance of water balance, wound healing and cell differentiation (Brown and Jones, 2005; Chen and Abatangelo, 1999; Kakehi et al., 2003).

HA is a linear biodegradable polysaccharide with viscoelastic properties. Due to its peculiar structure, HA can create and fill space by organizing and modifying the extracellular matrix, thus enabling several medicinal applications, e.g.

dermatological fillers, visco-supplementation for osteoarthritis treatment and surgical aid in ophthalmology. Moreover, HA based hydrogels are employed as dermal drug delivery systems, providing controlled release through the skin (Fakhari and Berkland, 2013; Salwowska et al., 2016).

Vitamin A and its derivatives (i.e. retinol, RP and retinoic acid) are important regulators of epidermal keratinocytes proliferation and differentiation. Vitamin A and its derivatives have antioxidant activity, exerting an important role in epithelial growth, limbal stem cell differentiation and corneal wound healing.

Notwithstanding their common wound healing effect, the physico-chemical properties of HA and RP are very different, being hydrophilic (log P -1.8) and lipophilic (log P 11.62), respectively therefore it is possible that those substances act at different tissue levels.

In this chapter, we investigated the potential of lipid nanoparticle dispersions as vehicles able to solubilize at the same time both RP and HA, namely considering the well-known nanoscale delivery systems solid lipid nanoparticles (SLN) and nanostructured lipid carriers (NLC) (Battaglia and Gallarate, 2012; Shidhaye et al., 2008). Particularly RP has been encapsulated within the lipid matrix of nanoparticles, while HA has been dissolved into the aqueous phase of nanoparticle dispersion, resulting in a nanoparticulate gel suitable for cutaneous administration. After production and characterization, as a first approach, wound healing effect of nanoparticulate gel was studied in an *in vitro* keratinocytes model of wound re-epithelialization.

The present results have been the object of the published paper: “Production and Characterization of Nanoparticle Based Hyaluronate Gel Containing Retinyl Palmitate for Wound Healing” [Esposito E., Pecorelli A., **Sguizzato M.**, Drechsler M., Mariani P., Carducci F., Cervellati F., Nastruzzi C., Cortesi R., and Valacchi G. “Production and Characterization of Nanoparticle Based Hyaluronate Gel Containing Retinyl Palmitate for Wound Healing.” *Current Drug Delivery* 15, no. 8 (2018): 1172–82. <https://doi.org/10.2174/1567201815666180518123926>].

6.2. RESULTS AND DISCUSSION

6.2.1. Preparation and characterization of lipid nanoparticles

In the present study lipid nanoparticles were produced by a previously assessed method namely ultrasound homogenization method (Esposito et al., 2017b). SLN and NLC were prepared using the composition described in *Table 17*.

Table 17: Composition of SLN and NLC

Acronym	Composition % (w/w)				
	tristearin	miglyol	poloxamer 188	water	RP
SLN	5.00	-	2.37	92.63	-
NLC	3.34	1.66	2.37	92.63	-
SLN-RP	5.00	-	2.37	92.53	0.10
NLC-RP	3.34	1.66	2.37	92.53	0.10

Irrespectively of their composition, both SLN and NLC appear as milky homogeneous dispersions, free from agglomerates (*Figure 24*). The presence of RP did not affect nanoparticle appearance, nor presence of agglomerates.

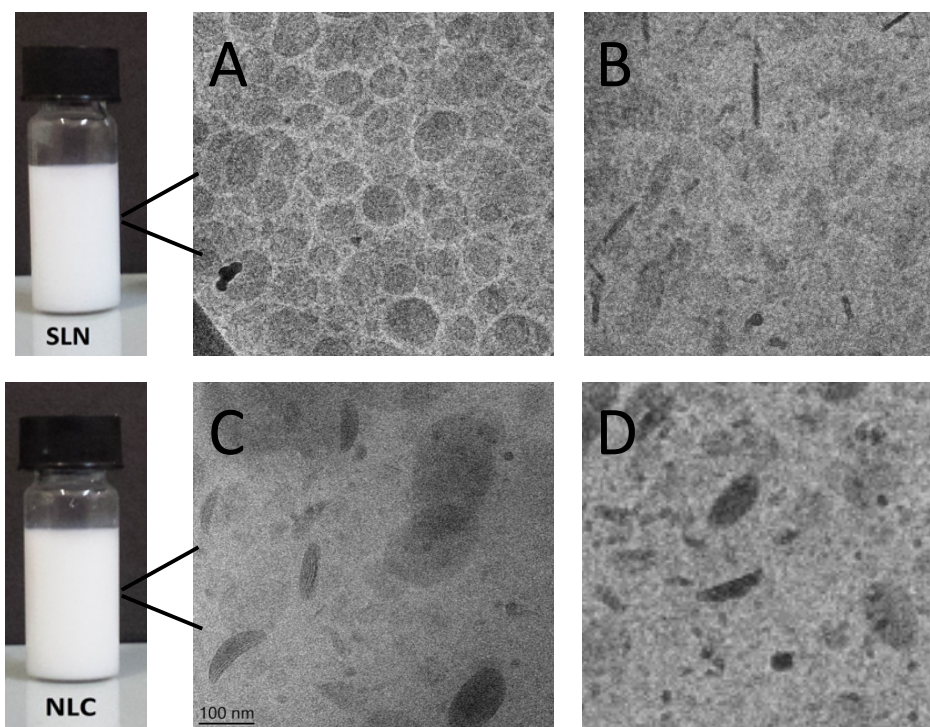


Figure 24: Macro and microscopic analysis of SLN and NLC. Cryo-TEM top-on-viewed images of to SLN (**A**, **B**) and NLC (**C**, **D**) produced in the absence (**A**, **C**) or in the presence of RP (**B**, **D**). Bar corresponds to 100 nm

The morphology of lipid nanoparticles visualized by cryo-TEM is reported in *Figures 24 and 25*. Since 3D nanoparticles are projected in 2D images, their aspect depends on their position in the thin vitrified film of the specimen. Indeed, nanoparticles appear as light flat discoids, if viewed from the top, or as darker thinner structures, when viewed edge-on (Esposito et al., 2016c). The images reported in *Figure 24* suggest that RP does not modify nanoparticle morphology, differences between SLN and NLC can be noted considering edge-on viewed structures, looking as electron-dense “needles” in the case of SLN (*Figure 24 B*) and as elliptical or semi-elliptical structures in the case of NLC (*Figure 24 C, D*).

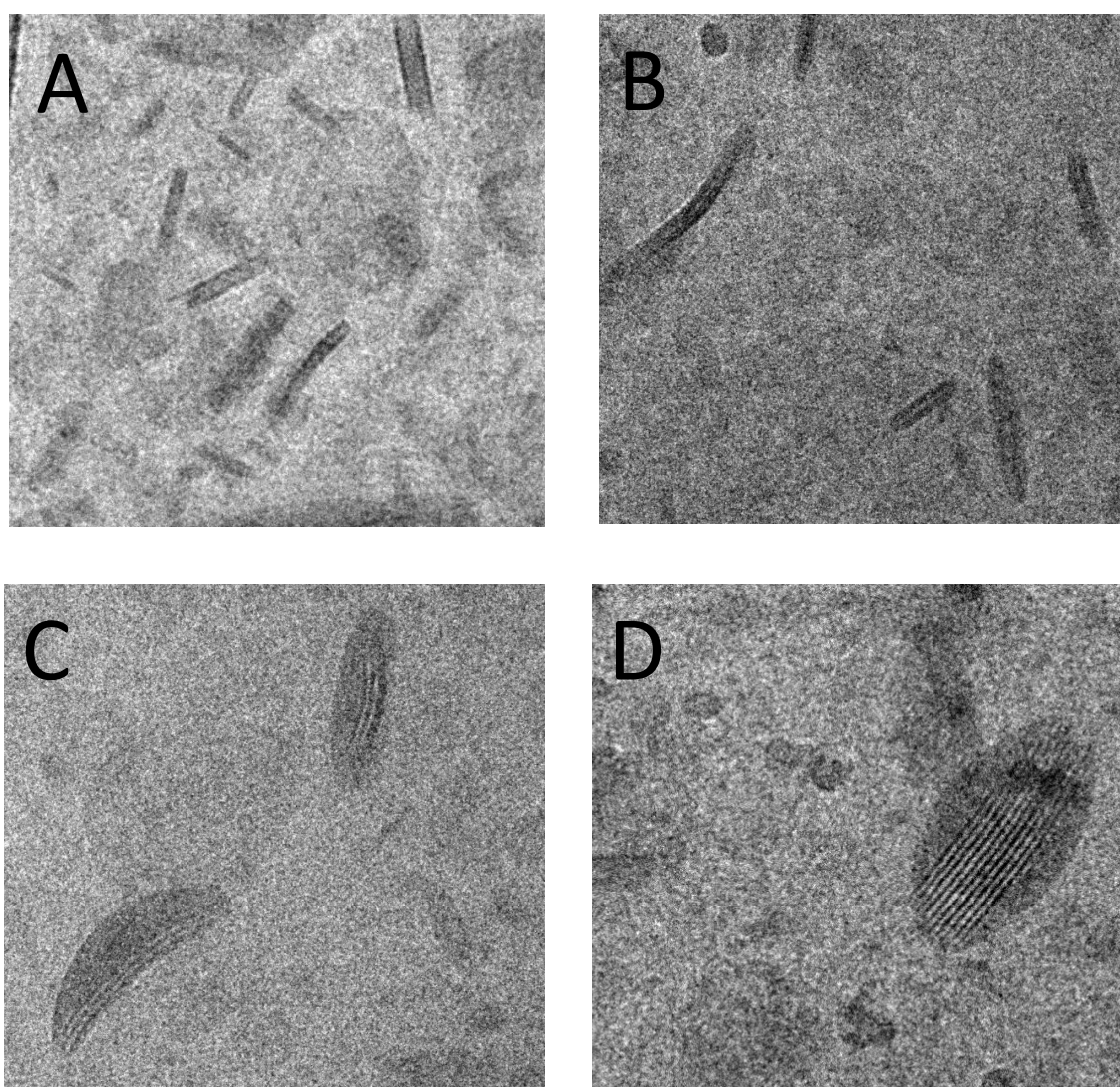


Figure 25: Cryo-TEM edge-on-viewed images of SLN (**A, B**) and NLC (**C, D**) produced in the absence (**A, C**) or in the presence of RP (**B, D**). Bar corresponds to 100 nm

Figure 25 reports edge-viewed nanoparticles imaged at higher magnification, to better visualize their internal structure. Remarkably, edge-on SLN (Figure 25 A) and SLN-RP (Figure 25 B) appear as bi-layered lamellar structures, while NLC (Figure 25 C) and NLC-RP (Figure 25 D) evidenced a multilamellar inner structure, surrounded by semi-ellipses. This last peculiar structure agrees with description of NLC morphology by Jores and colleagues, suggesting that miglyol, being liquid at room temperature, can form caps on the lamellar structure (Jores et al., 2004).

The dimensional distribution of SLN and NLC in the absence and in the presence of RP was determined by PCS studies. Mean diameters of nanoparticles expressed as Z average were comprised between 133 and 142 nm (Table 18) and were not affected by lipid composition or RP presence. Polydispersity index (Pdl) were always below 0.27, indicating a narrow size distribution and a homogenous particle population.

The inner structural features of SLN, SLN-RP, NLC and NLC-RP were investigated by X-ray diffraction, both in the low and the wide-angle region. Results are reported in Figure 26 and in Table 19.

Table 18: Dimensional characteristics of SLN and NLC

Acronym	Dimensional parameters*		
	Z average (nm)	N diam ^a (nm)	Pdl
SLN	138 ± 32	98 ± 23	0.26 ± 0.01
NLC	139 ± 15	106 ± 20	0.27 ± 0.01
SLN-RP	132 ± 46	105 ± 12	0.27 ± 0.04
NLC-RP	133 ± 22	99 ± 15	0.24 ± 0.03

*Data are the means ± sd of 6 independent batches. a: number diameter

A lamellar organization was observed, both in presence and absence of RP, confirming the preservation of the lamellar morphology. Thus, it can be asserted that the presence of RP does not modify the structural organization of lipid nanoparticles. The signal observed in the wide-angle region can be used to define the type of polymorphic form. In Figure 26 B, for all the samples measured, there is a strong main peak at 1.37 \AA^{-1} related to the sub-cell crystalline organization of nanoparticles, in a β -inner structure, triclinic parallel (Jenning et al., 2000).

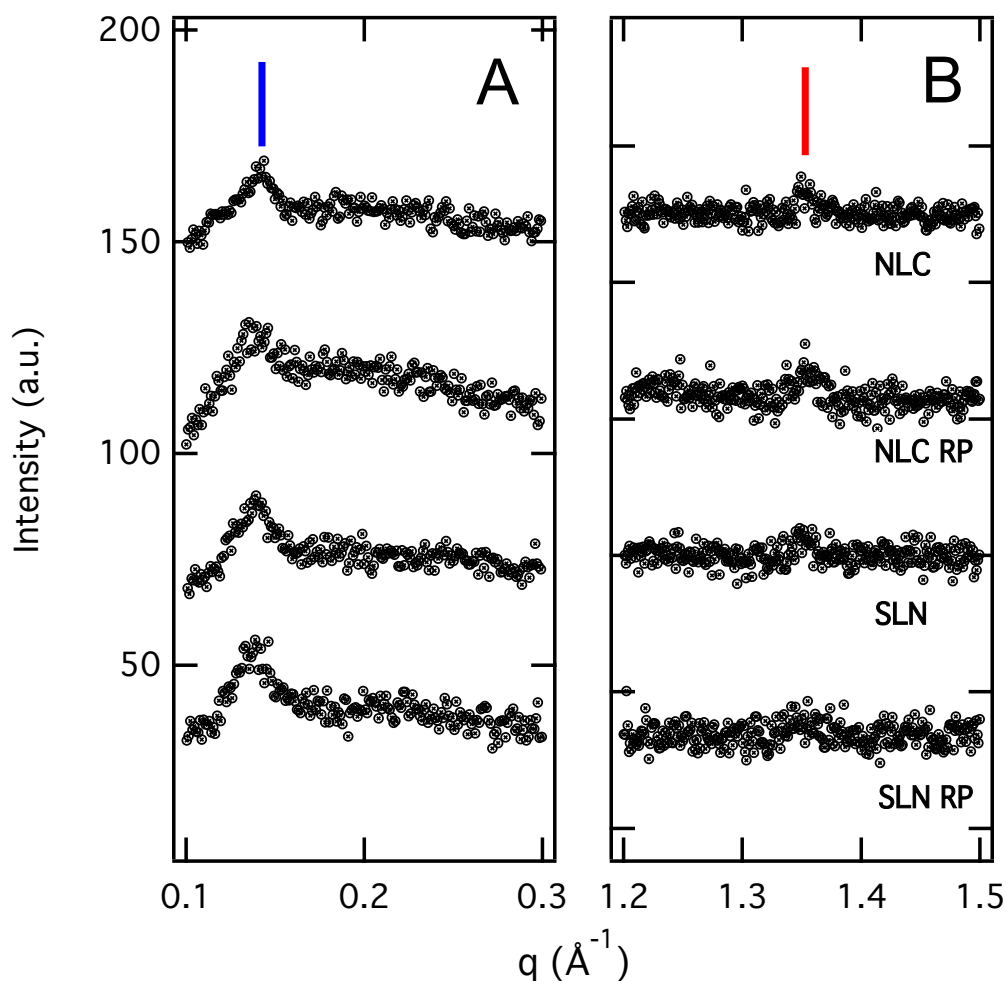


Figure 26: X-ray diffraction profiles observed both in the low-angle (A) and wide-angle region (B) for SLN and NLC, in the presence and absence of RP. The vertical blue line in panel A indicates the peak position of the first order of the Lamellar Phase Symmetry, the red line panel B is related to the sub-cell crystalline organization of nanoparticles. q is the modulus of the scattering vector, defined by the value $4\pi\sin/\lambda$, here reported in \AA^{-1}

Table 19: Structural organization obtained by X-ray diffraction experiments in the low and wide-angle region on the indicated nanoparticles

Nanoparticle type	Low angle region		Wide-Angle Region	
	Unit Cell (\AA)	Morphology	Peak Position (\AA)	Sub-cell Morphology
SLN	45.2	lamellar	4.6	β -triclinic parallel
NLC	45.5	lamellar	4.6	β -triclinic parallel
SLN-RP	45.3	lamellar	4.6	β -triclinic parallel
NLC-RP	45.9	lamellar	4.6	β -triclinic parallel

In order to compare nanoparticle capability to encapsulate RP, EE and LC were investigated. EE values were $55.1 \pm 2.7\%$ and $72.3 \pm 4.3\%$ for SLN-RP and NLC-RP respectively (*Table 20*), while the corresponding LC were $1.1 \pm 0.1\%$ and $1.4 \pm 0.2\%$.

Table 20: Content and shelf life values of RP in nanoparticles

Nanoparticle type	Shelf life values		
	RP content (%)	t_{90} (days)	$t_{1/2}$ (days)
SLN-RP	55.1 ± 2.7	2.13	36.56
NLC-RP	72.3 ± 4.3	14.11	247.50

As reported in *Table 20*, RP shelf life values in NLC-RP were longer with respect to SLN-RP, indeed, RP $t_{1/2}$ values were about 1 and 8 months for SLN-RP and NLC-RP respectively. Thus, RP was better incorporated and retained in NLC-RP, suggesting that in NLC-RP the presence of miglyol increases drug accommodation with respect to SLN-RP, constituted of sole tristearin. This result agrees well with previous findings of other authors who suggested that a combination of solid and liquid domains within a carrier allows to solubilize lipophilic drugs, thanks to the liquid regions, resulting in increased loading efficiency (Alam et al., 2015; Jennings et al., 2000; Tapeinos et al., 2017).

In reason of their higher value of EE and longer chemical stability, NLC-RP were selected to perform further experiments.

6.2.2. Preparation and characterization of nanoparticulate gel

In order to confer to NLC-RP a suitable viscosity for cutaneous administration, we chose to modify its viscosity by the addition of HA in reason of its well-known wound healing effect and its viscoelastic properties. Thus, HA is employed both for biological and textural purposes (Berriaud et al., 1994; Chen and Abatangelo, 1999). Different authors have reported on the influence of HA molecular weight on its biological activity on wound repair (D'Agostino et al., 2015; Fouda et al., 2016). On one hand, since low molecular weight HA generates low viscous gel, its application enables delivery of a high amount of HA to the injury site, hastening the repair process. On the other hand, high molecular weight HA gives rise to higher viscous

gels, but it can accumulate on wounds and binds fibrinogen that is essential for clot formation. In this study, HA with low, intermediate and high molecular weight were investigated. Particularly, HA₅₀, HA₃₀₀, or HA₈₀₀ (0.5% w/w) was directly added into the aqueous phase of NLC-RP after production and then allowed to completely hydrate, thus forming a nanoparticulate hydrogel. After 12 h, NLC-RP-HA gel reached a transparent and homogeneous appearance. *Figures 27 A-C* shows the aspect of nanoparticulate gels based on HA with different molecular weights, while *Figures 27 D* summarizes their spreadability behavior.

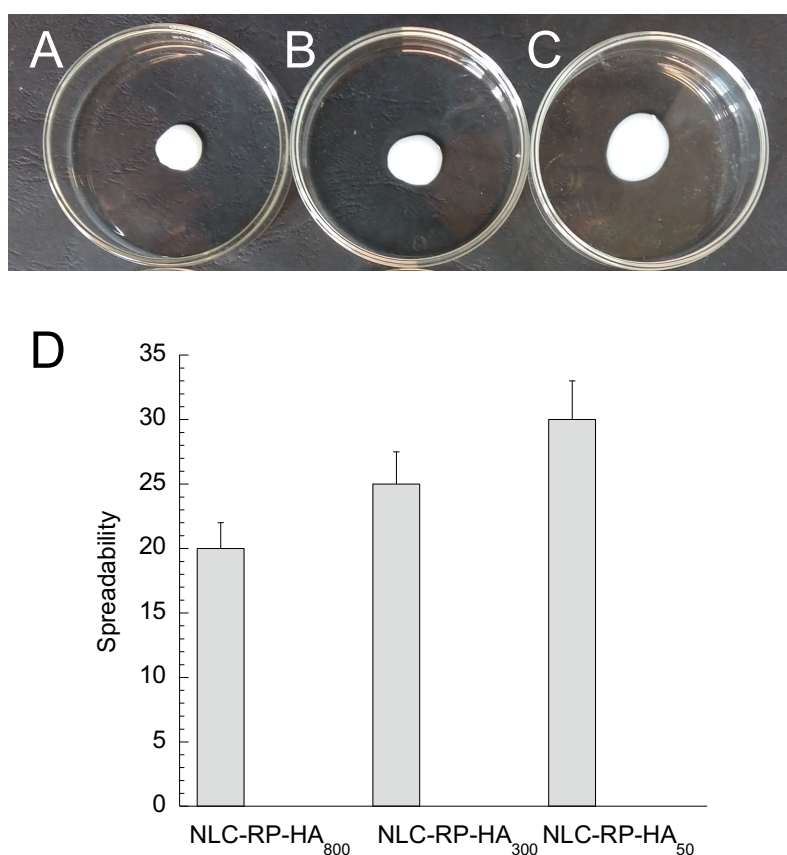


Figure 27: NLC-RP gels based on HA with different molecular weights, namely HA₈₀₀ (A), HA₃₀₀ (B) and HA₅₀ (C). Spreadability behavior of the indicated gels (D)

Spreadability of gels was measured because this parameter denotes the extent of area to which formulation readily spreads on application to skin, affecting the therapeutic efficacy of a formulation. As expected, the higher the molecular weight, the lower the spreadability of the gel, thus, the spreadability of the nanoparticulate gels follows the order NLC-RP-HA₅₀ > NLC-RP-HA₃₀₀ > NLC-RP-HA₈₀₀. In the present investigation in order to partially meet the properties of both high and low

molecular weight HA, we chose to employ an intermediate molecular weight one and NLC-RP-HA₃₀₀ was selected for further studies.

Figure 28 reports the viscosity behavior of NLC-RP-HA and plain HA gel (both based on HA₃₀₀). The nanoparticulate gel behaved as a non-newtonian shear thinning fluid, indeed, its viscosity decreased with increasing shear rate, while in the case of the plain gel, viscosity remained almost unvaried (Stocks et al., 2011). The viscosity of the gels at 100 r.p.m was 335.3 mPa-s for NLC-RP-HA and 142 mPa-s for the plain HA gel.

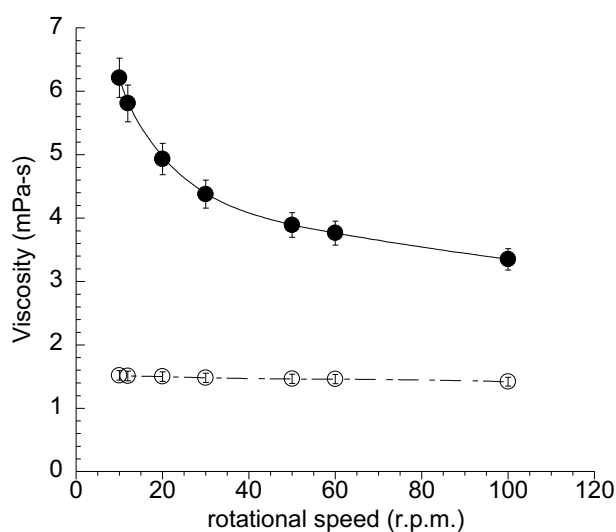


Figure 28: Viscosity of NLC-RP-HA₃₀₀ (closed circles) and HA₃₀₀ gel (open circles) as a function of rotational speed

NLC-RP viscosity is negligible, while in the case of NLC-RP-HA the addition of HA to the nanoparticle dispersion generates a complex system in which the polymer chains entanglement confers a shear dependent higher viscosity. Indeed, when shear stress is applied, the nanoparticulate gel seems to become thinner, behaving as a “pseudo-plastic” material (Fakhari and Berkland, 2013; Frykberg and Banks, 2015), thus its viscosity decreases under application, allowing to better spread on the wounds.

FT-IR spectroscopy was employed to obtain information about possible interactions between nanoparticle components, RP and HA. The main functional peaks present in the spectra are summarized in *Table 21*.

The comparison between functional groups of the different spectra suggests the absence of particular interactions between the lipids, HA and RP before and after

NLC preparation. Noteworthy the poloxamer 188 solution spectrum was almost superimposable to NLC-RP and NLC-RP-HA gel spectra, with two intense characteristic peaks (3335 and 1635 cm^{-1}) ascribable to the O-H stretching mode of water (data not shown). Indeed, it should be considered that the aqueous phase represents $\sim 92\%$ of the whole nanoparticle-based formulations. Since the spectra of RP and of NLC lipid components are similar, no unmistakable evidence of RP was identified in the NLC-RP spectra.

Table 21: FTIR peaks values of sole NLC components, their physical mixture, RP-containing NLC with or without HA

	Functional Groups ^a					
	O-H	-C-H	C=O	C-OH	CH3	C-O-C
RP	-	2922	1736	-	1456	1160
HA ₃₀₀	3282	-	1738	1030	-	-
Tristearin	-	2915	1739	1097	1464	1172
Miglyol	-	2915	1739	1097	1464	1172
Pol 188 sol ^b	3335*/1635	-	-	1091	1366	1228
Physical mixture ^c	-	2915	1739	1104	1366	1229
NLC-RP	3350*/1634	2916	1736	1092	1471	-
NLC-RP-HA gel	3342*/1639	2916	1737	1094	1471	1179

a: cm^{-1} ; b: aqueous solution of poloxamer 188 (2.5% w/w); c: tristearin+miglyol+RP+HA300; *strong and broad peak

6.2.3. RP Diffusion Study

Franz cell was employed to compare the diffusion kinetics of RP from NLC-RP and NLC-RP-HA gel. Nylon membranes and a non-physiological receptor phase with 50% v/v of ethanol were used, to allow the establishment of the sink conditions and to sustain permeant solubilization (Siewert et al., 2003; Touitou and Fabin, 1988). *Figure 29* summarizes the obtained results, as expected, RP diffusion was faster from NLC-RP than from NLC-RP-HA gel. The slope, which represents the release rate, steady-state flux, was calculated by linear regression of the linear portion of the curve. The RP calculated fluxes from NLC-RP and NLC-RP-HA gel were 1.076 and $0.480 \times 10^{-3}\text{ cm/h}$ respectively. Thus, the RP flux in the case of HA containing gel was about 2.24-fold lower than those obtained by plain NLC-RP, resulting in a better control of RP diffusion by NLC-RP-HA gel.

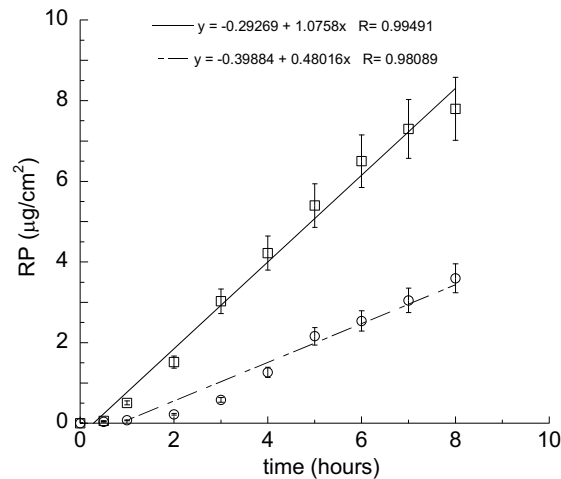


Figure 29: RP diffusion kinetics from NLC-RP (square) and NLC-RP-HA (circle), as determined by Franz cell experiment

6.2.4. Cytotoxicity

To determine the range of HA and RP concentrations nontoxic for HaCaT cells, the LDH release in the media was assessed after 24 h of treatment with the different vehicles.

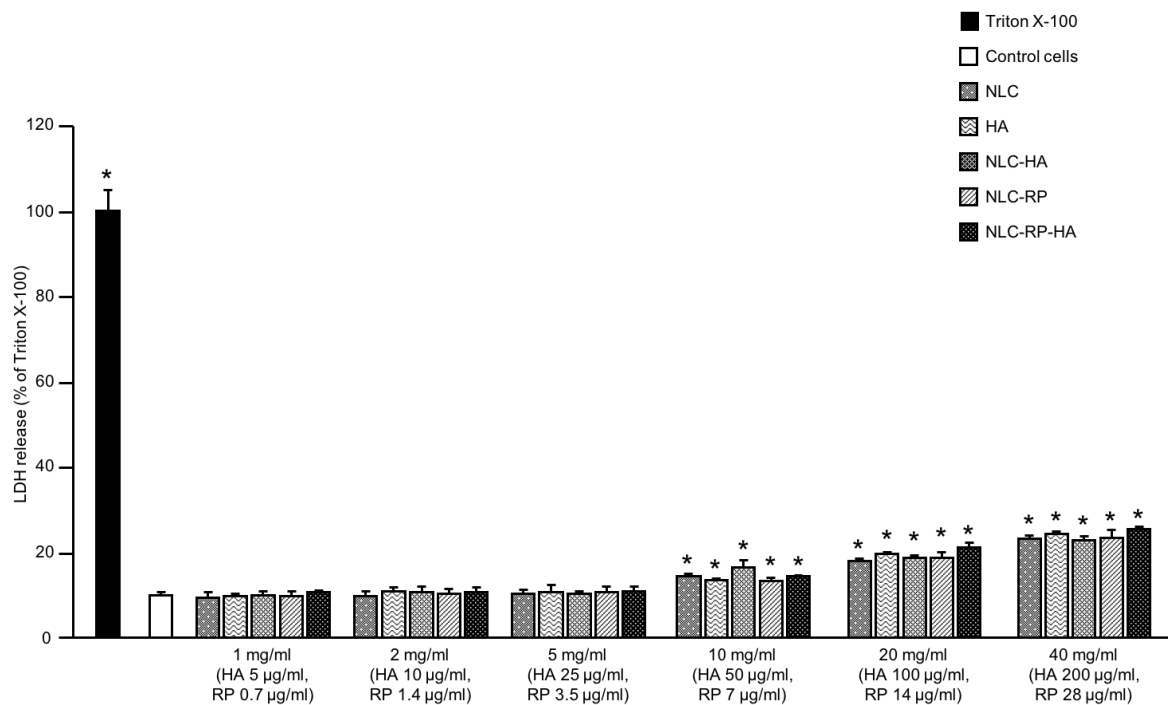


Figure 30: Cytotoxicity of the nanoparticulate gels evaluated by LDH release from HaCaT cells in the media after 24 h of treatment. Data are expressed as percentage LDH release as compared to the maximum release of LDH from Triton-X100-treated cells. Data are means \pm sd, representative of three independent experiments with at least three technical

replicates each time. *indicates statistically significant difference to untreated control cells (unpaired t-test, $p < 0.01$)

As shown in *Figure 30*, HA- and RP-induced cytotoxicity occurred in a dose-dependent manner, starting at the 50 $\mu\text{g/ml}$ HA and 7 $\mu\text{g/ml}$ RP concentrations onward. Based on these cytotoxicity data, the nanoparticulate gels containing HA 25 $\mu\text{g/ml}$, RP 3.5 $\mu\text{g/ml}$ RP were selected as the highest non-cytotoxic concentration for the subsequent scratch wound assay.

6.2.5. Wound healing assay

To test whether nanoparticulate gels could improve the delivery of RP and HA in keratinocytes, thus promoting cutaneous wound healing, an *in vitro* scratch-wound assay was performed. As shown in *Figure 31*, HA, NLC-HA, NLC-RP and NLC-RP-HA gels significantly increased the recovery of the wound area during the different time points: almost 20%, 37.5%, 46% and 58%, respectively, at 12 h; almost 43%, 56%, 72% and 80%, respectively, at 18 h; almost 50%, 76.5%, 89% and 96%, respectively, at 24 h.

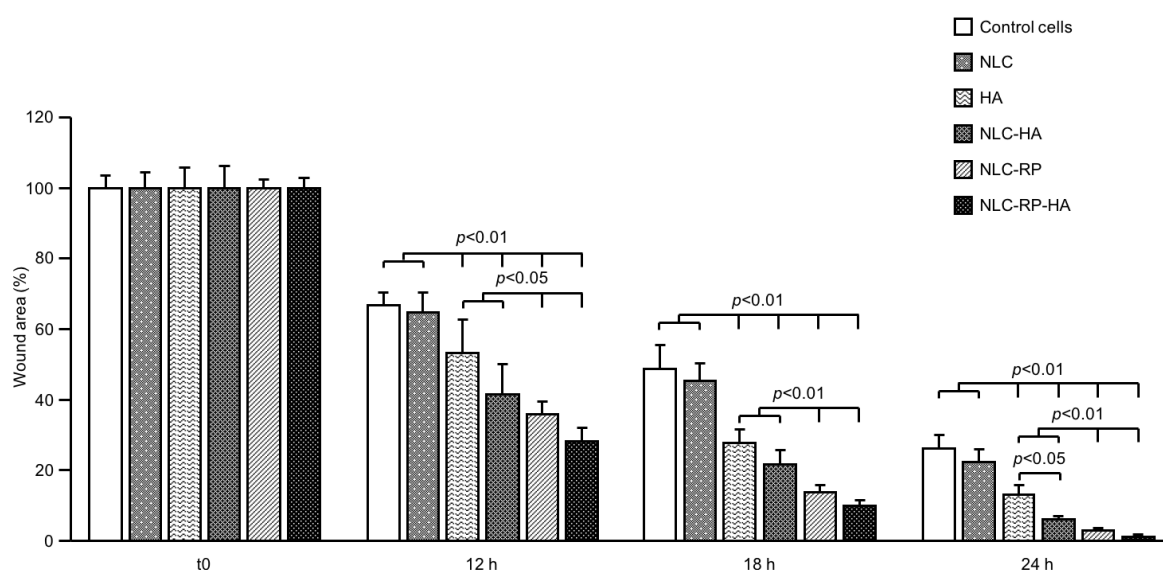


Figure 31: Effect of nanoparticulate gels containing both RP and/or HA in recovering the scratch wound in a model based on HaCaT cells. The graph shows the quantitative measurement of wound closure rate in HaCaT cells treated with the nanoparticulate gels at different time intervals (0, 12, 18 and 24 h) after the scratch wound. Gap area is expressed as a percentage of the original wound at 0 h for each treatment. Data are mean \pm sd of triplicate batches in three independent experiments

No significant difference appeared in wound closure rate between HA gel and NLC-HA, except at 24 h ($p < 0.05$). Furthermore, at each examined time point, the cells treated with the nanoparticulate gels containing alone RP and both RP and HA (i.e. NLC-RP and NLC-RP-HA) showed the most significant reduction in relative wound size compared to the other treatments, reaching the complete wound closure at 24 h. No difference was observed between untreated control cells and cells treated with NLC vehicle during the various time points post-scratch.

Our results demonstrated that nanoparticulate gels can represent an alternative and valid approach to promote the healing of wounds without any toxicity to the cutaneous epithelial cells. Interestingly, in our 2D cell model, the association of RP and HA showed an additive effect on the wound healing process, which could be in part due to the simultaneous combination of their lipophilic and hydrophilic properties. Thanks to these distinct features, two active compounds could act in parallel on the different molecular mechanisms involved in the wound repair and regeneration. Because the healing of a skin wound is achieved through a sequential and highly programmed cascade of events that involve several different cell processes and types (Martin and Nunan, 2015), further investigation is needed to understand the mechanisms of synergy between RP and HA in our nanoparticle gels.

7. LIPID NANOSTRUCTURES FOR α -TOCOPHEROL DELIVERY: A PREFORMULATION STUDY

7.1. INTRODUCTION

Air pollution increasingly affects industrialized urban areas with dramatic sequels for environment and human health. Besides being the cause of respiratory diseases (e.g. chronic obstructive pulmonary disease, asthma and lung cancer), pollution is responsible of cutaneous pathologies, spanning from skin aging, inflammation and allergy up to skin cancer (Rembiesa et al., 2018).

Cigarette smoke (CS) is one of the major toxic pollutant, exerting an important role in the onset of many serious and fatal diseases. In the last 2 decades, the noxious effect of CS on skin has been well demonstrated (Kennedy et al., 2003; Suehara et al., 2006). For instance, the chronic exposure of skin to CS induces premature skin ageing, psoriasis and inflammatory skin diseases and delays wound healing, (Onor et al., 2017). Indeed, tobacco smoke is constituted of thousands of toxic compounds, including benzene, formaldehyde, hydrogen cyanide, carbon monoxide, arsenic and radioactive components producing free radicals that cause oxidative stress (Hu et al., 2016). The release of reactive oxygen species from tobacco smoke provokes a series of systemic immunomodulatory effects that leads to a compromised inflammatory response. These destructive mechanisms affect also collagen synthesis and the skin cellular reparative effects (Benowitz et al., 2009; Bruno and Traber, 2005). It has been found that antioxidants play a key role in the regulation of the deleterious activity exerted by CS in humans, nevertheless CS alters the requirements of antioxidants, such as vitamins E and A (Bruno and Traber, 2005; Dietrich et al., 2003; Handelman et al., 1996). In this respect, quitting smoking is not always resolving the issue, since even more toxic effects have been shown for second-hand smoke.

Recently many cosmetic producers have focused their efforts towards antipollution dermocosmetics able to defend the skin against prolonged and repetitive daily exposure to pollutants, for instance film-formers or skin rejuvenating excipients have been developed. Nevertheless, these strategies offer merely a short-term improvement of skin barrier function. Thus, in this respect there is an unmet need

for an efficacious product, endowing skin protection from pollutants in long-term exposure, as well as for antipollution test methods suitable for assessing product efficacy and safety (Mistry, 2017).

Vitamin E is a potent antioxidant, able to counteract the reactive oxygen species production during fat oxidation and free radical propagation, indeed it can protect the cell membranes from free radical attack, acting against lipid peroxidation. Vitamin E exists in 8 different forms, 4 tocopherols and 4 tocotrienols (Wolf, 2005). Among them α -tocopherol (TOC) (Figure 32) can be mostly adsorbed and accumulated, thus it is largely employed as antioxidant for edible oils and in anti-aging products. Notably, TOC has been proposed for the treatment of cancer and skin barrier improvement (Buettner, 1993; Chen et al., 2017; Vaz et al., 2019).

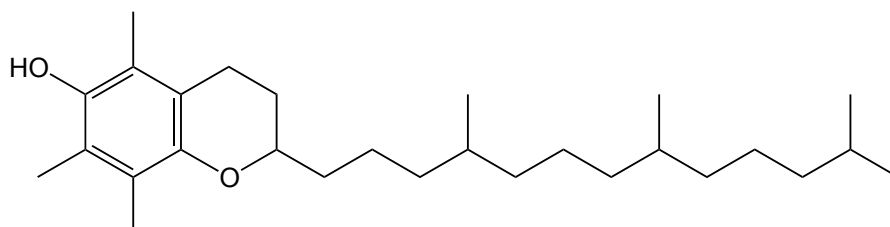


Figure 32: Chemical structure of α -tocopherol

Despite the enormous potential of TOC, some drawbacks are associated to their topical use, such as photodegradation, poor water solubility and irritative skin effects when employed in high dosage (MacGregor and Maibach, 2002). Thus, TOC need to be loaded in specialized formulations suitable for skin application and able to adequately protect them from degradation. In this respect, recently different lipid nanoparticles have been proposed, including solid lipid nanoparticles (SLN) and nanostructured lipid carriers (NLC) (Castro et al., 2007; Eiras et al., 2017; Saez et al., 2018). The choice of type and concentration of nanoparticle lipid matrix is crucial since it can affect the physico-chemical aspect of SLN and NLC, the encapsulation parameters, as well as the long-term stability of the formulation. Thus, in view of an industrial production, a preliminary formulative screening appears imperative (Dingler and Gohla, 2002; Paliwal et al., 2014).

In the present chapter an investigation conducted to develop a nanoparticulate approach for counteracting skin pollution is reported. Preliminarily, a preformulatory study was performed to select the type and composition of lipid nanoparticles suitable for encapsulating TOC. In addition, to assess the effect of antioxidant loaded in nanoparticles, a Western blot analysis has been performed to evaluate

heme oxygenase (HO-1) expression on human skin explants treated with nanoparticles and exposed to CS.

The present results have been the object of the published paper: “Lipid nanostructures for antioxidant Delivery: a comparative preformulation study” [Esposito E., **Sguizzato M.**, Drechsler M., Mariani P., Carducci F., Nastruzzi C., Valacchi G., and Cortesi R. “Lipid Nanostructures for Antioxidant Delivery: A Comparative Preformulation Study.” *Beilstein Journal of Nanotechnology* 10 (2019): 1789–1801. <https://doi.org/10.3762/bjnano.10.174>].

7.2. RESULTS AND DISCUSSION

7.2.1. Effect of lipid composition on nanoparticle macrostructure

In order to obtain a nanoparticulate system suitable for cutaneous administration of antioxidant, different lipid compositions summarized in *Tables 22* and *23* have been considered.

Table 22: Composition of solid lipid nanoparticles (SLN)

preparation	Composition % (w/w)					
	lipid phase				water phase	
	tristearin	compritol	precirol	suppocire	poloxamer 188	water
SLN T5	5	-	-	-	2.37	92.63
SLN T10	10	-	-	-	2.25	87.75
SLN C5	-	5	-	-	2.37	92.63
SLN C10	-	10	-	-	2.25	87.75
SLN P5	-	-	5	-	2.37	92.63
SLN P10	-	-	10	-	2.25	87.75
SLN S5	-	-	-	5	2.37	92.63
SLN S10	-	-	-	10	2.25	87.75

Table 23: Composition of nanostructured lipid carriers (NLC)

preparation	Composition % (w/w)						
	lipid phase					water phase	
	tristearin	compritol	precirol	suppocire	miglyol	poloxamer 188	water
NLC T5	2.5	-	-	-	2.5	2.37	92.63
NLC T10	5.0	-	-	-	5.0	2.25	87.75
NLC C5	-	2.5	-	-	2.5	2.37	92.63
NLC C10	-	5.0	-	-	5.0	2.25	87.75
NLC P5	-	-	2.5	-	2.5	2.37	92.63
NLC P10	-	-	5.0	-	5.0	2.25	87.75
NLC S5	-	-	-	2.5	2.5	2.37	92.63
NLC S10	-	-	-	5.0	5.0	2.25	87.75

Lipids were selected on the basis of their not toxicity, commercial lipid availability, similarity of chemical composition and different length carbon chains to tristearin and caprylic/capric triglycerides (miglyol), previously studied by my research group

(Esposito et al., 2008). Namely, SLN have been produced based on the use of solid di- or tri-glycerides, with chain length ranging between 18 and 21 carbon atoms, while for NLC production the same solid lipids were employed in mixture (1:1 ratio, w/w) with the liquid miglyol, characterized by C₈-C₁₀ chains.

With regard to the aqueous phase, a surfactant concentration based on poloxamer was used. Namely a concentration of 2.5%, 3% and 4 % by weight with respect to the aqueous phase have been tested, but the increase of poloxamer led to foam formation during preparation causing irregular and inhomogeneous formulations, thus 2.5% w/w of poloxamer was selected for the study.

The hot homogenization method followed by ultrasound (Esposito et al., 2008) lead to production of milky and homogeneous dispersions, nonetheless, immediately after cooling, in most cases a small amount of coalesced lipid phase appeared on the surface of the dispersion. The weight of this agglomerate, spanning between 0 and 4.65% by weight with respect to the total amount of the lipid phase, was a function of the lipid composition. Indeed, both the amount and the type of lipid phase appear to influence the agglomerate formation. Particularly, the longer the lipid chain, the higher the agglomerate weight according to the following trend: compritol (2 C₂₁ chains) > tristearin (3 C₁₈ chains) > precinol (2 C₁₈ chains) > supocire (3 C₁₀-C₁₈ chains). Specifically, as reported in the second part of this chapter (*Table 24*) in the latter case the agglomerate was almost absent. In addition, the extent of agglomeration was lower for NLC, probably due to the presence of the liquid lipid.

7.2.2. Effect of lipid composition on size distribution of nanoparticles

SLN and NLC dimensions were measured by PCS and expressed by Z Average. The obtained results are reported in *Figure 33* and *Table 24*.

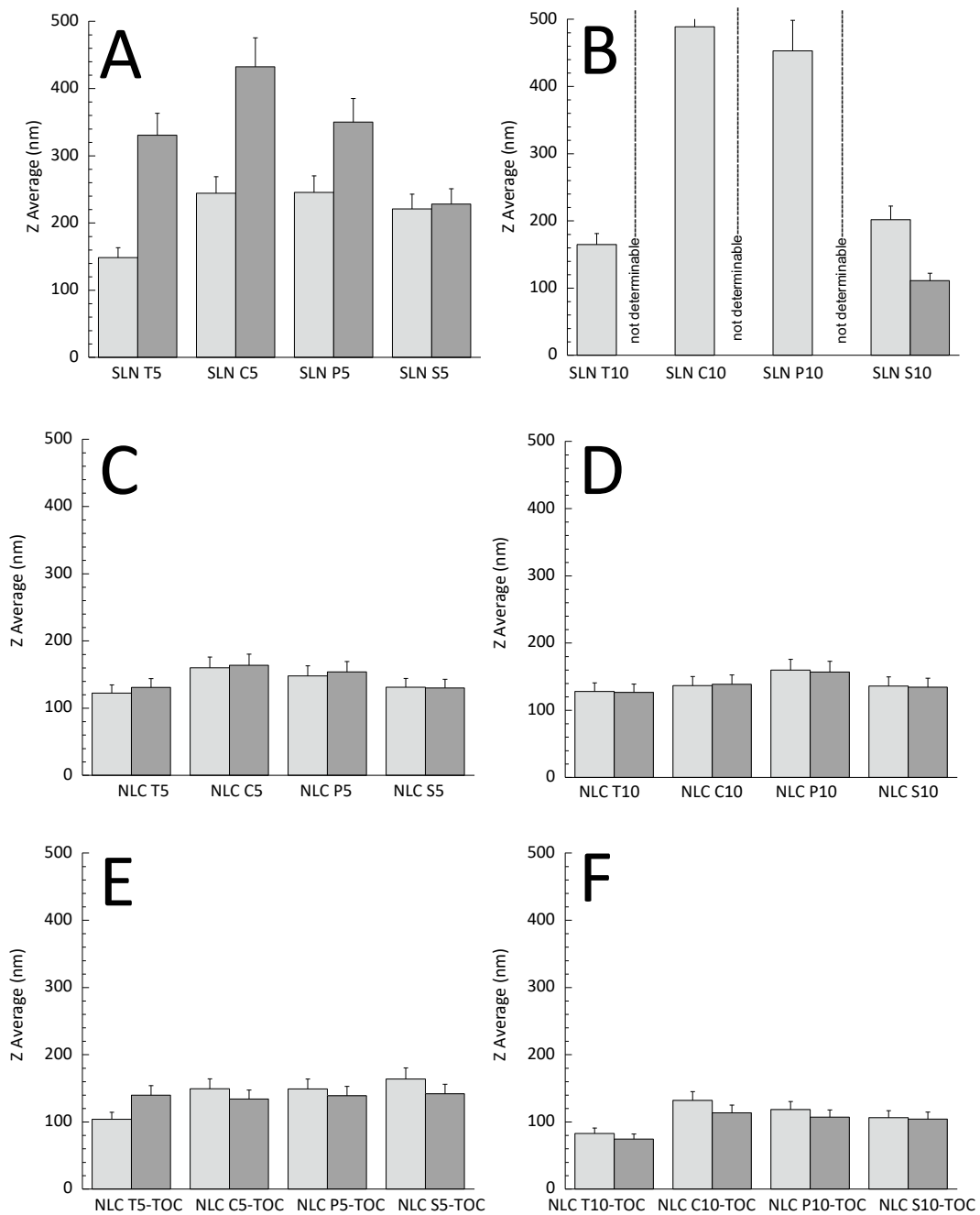


Figure 33: Variation of Z Average mean diameters of SLN (**A, B**) and NLC (**C, D**) produced in the absence of antioxidants or NLC loaded with TOC (**E, F**) evaluated at 1 (light grey) and 90 (grey) days after nanoparticle production. In the case of SLN T10, SLN C10 and SLN P10, mean diameters were not measurable by PCS 90 days after production

Table 24: Dimensional characteristics of SLN or NLC and presence of agglomerates

preparation	Z average (nm)	Polydispersity index	Agglomerate*(%)
SLN T5	148.6 ± 74.5	0.35 ± 0.11	2.86 ± 0.04
SLN T10	164.9 ± 9.4	0.33 ± 0.04	4.65 ± 0.03
SLN C5	244.5 ± 26.5	0.36 ± 0.01	3.43 ± 0.02
SLN C10	488.9 ± 25.3	0.32 ± 0.04	3.77 ± 0.04
SLN P5	245.5 ± 31.9	0.31 ± 0.03	2.48 ± 0.03
SLN P10	453.1 ± 9.3	0.39 ± 0.02	2.99 ± 0.04
SLN S5	220.9 ± 15.6	0.37 ± 0.06	1.13 ± 0.03
SLN S10	201.8 ± 82.1	0.39 ± 0.06	0.60 ± 0.04
NLC T5	122.6 ± 34.2	0.32 ± 0.07	2.14 ± 0.02
NLC T10	127.9 ± 29.1	0.29 ± 0.03	2.54 ± 0.01
NLC C5	160.2 ± 25.5	0.29 ± 0.03	3.15 ± 0.02
NLC C10	136.8 ± 51.5	0.24 ± 0.04	3.25 ± 0.01
NLC P5	148.1 ± 29.5	0.22 ± 0.10	1.51 ± 0.01
NLC P10	159.8 ± 33.7	0.30 ± 0.08	1.84 ± 0.02
NLC S5	131.3 ± 30.5	0.31 ± 0.05	0 ± 0.01
NLC S10	136.1 ± 13.5	0.29 ± 0.07	0 ± 0.01

* loss of lipids (lipid phase) due to the partial coalescence of the lipid phase during the formation of the O/W emulsion. % refers to the weight of the lipid phase. Data represent the mean ± sd of 6 independent experiments

In the case of SLN with 5% lipid phase concentration by weight, mean diameters were comprised between 148 and 245 nm. On the other hand, the doubling of lipid phase concentration induced an increase of mean diameter, especially in the case of precirol (SLN P10) and compritol (SLN C10), whose Z Average reached almost 500 nm. On the contrary, in the case of NLC the lipid phase composition scarcely affected mean diameters, ranging between 125 and 160 nm both for 5% and 10% of lipid phase. Polydispersity indexes were always below 0.39, with smaller values in the case of NLC dispersions.

Z Average mean diameters of SLN and NLC stored at 25°C were measured after 3 months from production. In the case of SLN, mean diameters dramatically increased, as shown in *Figure 33 A* and *33 B*, especially for SLN T10, SLN C10 and SLN P10, that gave rise to particles undetectable by PCS. Interestingly, mean diameters of suppicire based SLN both at 5% and 10% remained quite stable. This behavior can be attributed to the type of lipid phase able to influence both agglomerate formation and size of the produced nanoparticles. On the contrary,

NLC maintained their mean diameters almost unvaried, irrespectively of the lipid phase type and concentration (*Figures 33 C and 33 D*).

On the basis of these last results, in order to avoid agglomeration phenomena and control mean size, NLC have been selected for antioxidant loading.

7.2.3. Production and characterization of NLC containing TOC

Antioxidant containing NLC were produced loading different amounts of TOC, namely 0.4% w/w in the case of 5% NLC lipid phase and 0.8% w/w in the case of 10% NLC lipid phase. Particularly, since TOC is practically insoluble in water (logP 8.84), it was directly added to caprylic/capric triglycerides (miglyol) before addition of solid lipids and in this way its solubility can reach 16 mg/ml. The doubling of lipid phase concentration enabled to double the amount of TOC loading. The macroscopic aspect of NLC containing TOC was milky and homogeneous, as for empty NLC. Both agglomerate presence and mean size of TOC-containing NLC were lower with respect to the empty counterparts (*Table 25*).

Table 25: Dimensional characteristics, presence of agglomerates and encapsulation parameters of antioxidant containing NLC

NLC preparation	Z average (nm)	Polydispersity index	Agglomerate ^a (%)	Encapsulation efficiency ^b	Loading capacity ^c
NLC T5-TOC	104.5 ± 32.0	0.33 ± 0.11	1.22 ± 0.02	90.96 ± 1.3	7.27 ± 0.1
NLC T10-TOC	82.8 ± 10.7	0.36 ± 0.05	1.24 ± 0.01	90.69 ± 2.8	7.25 ± 0.2
NLC C5-TOC	149.4 ± 36.9	0.22 ± 0.03	2.25 ± 0.01	95.61 ± 1.5	7.64 ± 0.2
NLC C10-TOC	132.7 ± 51.3	0.34 ± 0.05	3.17 ± 0.02	79.15 ± 2.5	6.33 ± 0.1
NLC P5-TOC	149.5 ± 30.3	0.30 ± 0.02	1.11 ± 0.01	93.58 ± 1.7	7.48 ± 0.1
NLC P10-TOC	118.5 ± 31.9	0.30 ± 0.05	1.12 ± 0.02	90.99 ± 2.2	7.27 ± 0.2
NLC S5-TOC	164.6 ± 21.7	0.29 ± 0.06	0.00 ± 0.01	88.16 ± 1.3	7.05 ± 0.1
NLC S10-TOC	106.1 ± 24.2	0.29 ± 0.07	0.00 ± 0.01	60.72 ± 2.1	4.85 ± 0.1

^aloss of lipids (lipid phase) due to the partial coalescence of the lipid phase during the formation of the O/W emulsion. After cooling the coalesced lipid phase appeared as a small flake floating on the surface of the NLC dispersion. ^bpercentage (w/w) of drug in the whole dispersion with respect to the total amount used for the preparation. ^cpercentage (w/w) of drug within nanoparticles as compared to the amount of lipid used for the preparation. Data represent the mean ± SD of 6 independent experiments

This trend could suggest that TOC could contribute to stabilize the interface between the lipid and the aqueous phase, leading to smaller droplets and finally to smaller nanoparticles. The agglomerate presence was more evident in the case of compritol and absent in the case of suppcire, as in the case of empty NLC, while mean dimensions were inversely proportional to the amount of lipid phase and TOC. As observed in the case of the empty counterparts, Z Average mean diameters of antioxidants containing NLC stored at 25°C for 3 months were almost unvaried (*Figures 33 E and 33 F*). Particularly, NLC T10-TOC displayed the smallest mean diameters even after 3 months.

The morphology of NLC has been investigated by cryo-TEM and a few images are reported in *Figure 34*.

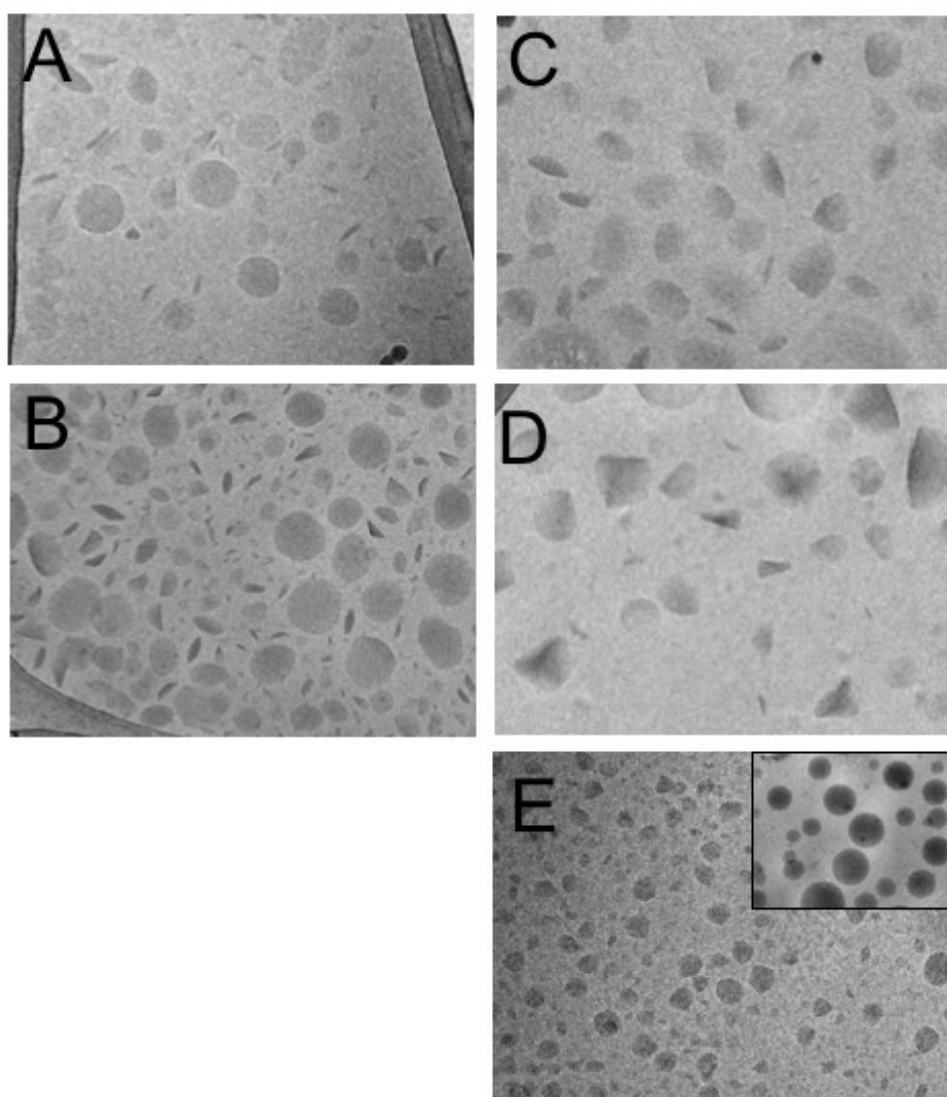


Figure 34: Cryo-TEM images of NLC T10 (A), NLC T10-TOC (B), NLC C5-TOC (C), NLC P5-TOC (D), NLC S5-TOC (E). Bar corresponds to 200 nm in panels A-D and 300 nm in panel E

In general, the shape of NLC appears discoid in the case of top view, or more electron-dense and rod-like in the case of edge-on view. In the case of tristearin based NLC, the shape was roundish, both for empty (*Figure 34 A*) or antioxidant-loaded NLC T10 (*Figure 34 B*). In the case of compritol (*Figure 34 C*) and precirrol (*Figure 34 D*) based NLC, ovoidal and triangular structures were observed. At last, in the case of suppicire NLC, besides irregular structures (*Figure 34 E*), spherical ones were detected (*insert of Figure 34 E*), resembling to vesicles rather than to solid particles.

The inner morphology of NLCs was further characterized by SAXS (Esposito et al., 2008; Kulkarni, 2012). In particular, low-angle X-ray scattering experiments were performed on NLC samples prepared by using tristearin or suppicire both in the presence and in the absence of TOC. By way of illustration, *Figure 35* shows the low-angle diffraction profiles obtained as a function of the lipid phase concentration from T5 and T10 based NLC (panel A) and from S5 and S10 based NLC (panel B), both containing TOC. The presence of Bragg peaks in the NLC T5-TOC and NLC T10-TOC samples indicates that the lipid used strongly influences the inner structure of the NLC at 30°C. Particularly, tristearin guarantees the presence of an ordered structural organization inside the NLC, while suppicire is not able to preserve such organization. This finding is in agreement with the cryo-TEM findings, where the presence of vesicles rather than nanoparticles are evident and probably form in these conditions.

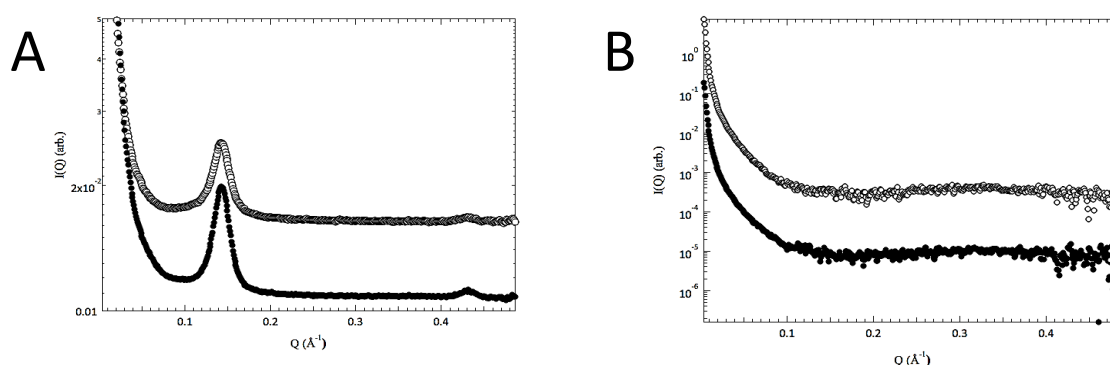


Figure 35: SAXS profiles observed for NLCT5-TOC (open symbol) and NLCT10-TOC (closed symbol) (A) and NLCS5-TOC (open symbol) and NLCS10-TOC (closed symbol) (B)

The analysis of the position of the peaks observed in tristearin based NLC allowed the identification of the internal structural organization for NLC T5-TOC and NLC T10-TOC: because the spacing ratios scale as 1:2:3..., a lamellar organization was

derived (Dingler and Gohla, 2002; Jennings et al., 2000). The corresponding unit cell dimension, which in a lamellar organization is the repeated distance between two lamellae, resulted 43.9 Å. It should be noticed that similar results were obtained from empty tristearin based NLC: the packing of the lamellae in the nanoparticle inner region is not affected by the presence of the antioxidant.

7.2.4. Encapsulation of TOC in NLC

The influence of NLC lipid composition on the capability to incorporate antioxidants was studied by evaluating EE and LC. The values reported in *Table 25* and *Figure 36* evidenced that in the case of tristearin or precirrol based NLC, TOC EE was > 90%, irrespectively from lipid phase concentration. In the case of NLC C10-TOC, both a decrease of EE value and an increase of agglomeration were detected with respect to NLC C5-TOC. This behavior suggests that the lipid concentration doubling promotes the agglomeration of lipid phase, partially avoiding TOC encapsulation within the nanoparticles. This hypothesis was corroborated by disaggregation and HPLC analysis of the lipid agglomerate, revealing the presence of TOC 13 % w/w with respect to the total amount used for NLC production.

The lowest EE values were found in the case of NLC S10-TOC.

In the case of suppicire, TOC EE values decreased from 88 to 60% by doubling the lipid phase concentration, suggesting that the presence of vesicles instead of nanoparticles prevented high loading of the antioxidant within their structure.

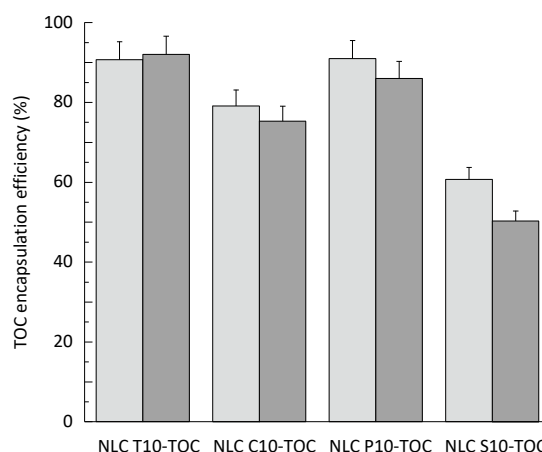


Figure 36: TOC encapsulation efficiency in the indicated NLC, evaluated at 1 (light grey) and 90 (grey) days after production

In order to detect the capability of NLC to control the encapsulation of antioxidant under storage, EE values have been evaluated for 90 days (*Figure 36*). Particularly, NLC containing 10% lipid phase have been selected, due to their marked dimensional stability. TOC EE values were almost unvaried in the case of NLC T10-TOC, they slightly decreased in the case of NLC C10-TOC and NLC P10-TOC, whilst the decrease was more evident in the case of NLC S10-TOC, passing from 60 to 48 %. It can be hypothesized that the prevalence of vesicles in NLC S10-TOC, instead of more structured carriers, prevented the maintenance of TOC encapsulation.

7.2.5. Cytotoxicity of NLC containing TOC

As the produced formulations are intended for topical administration on the skin, experiments on human keratinocytes were conducted in order to test the cytotoxicity of NLC T10-TOC, NLC C10-TOC, NLC P10-TOC and NLC S10-TOC. The LDH release in the media was assessed 24 h after TOC treatment at the concentrations of 25, 50, 100 and 200 μM .

As shown in *Figure 37*, no NLC cytotoxicity was observed with respect to control cells and no significant difference among the different NLC was noticed, confirming the biocompatibility of the components.

Due to the obtained results, NLC T10-TOC were selected for further ex-vivo studies. Indeed, this kind of NLC displayed better physico-chemical properties with respect to NLC based on different lipid compositions, being able to longer maintain size and EE of TOC.

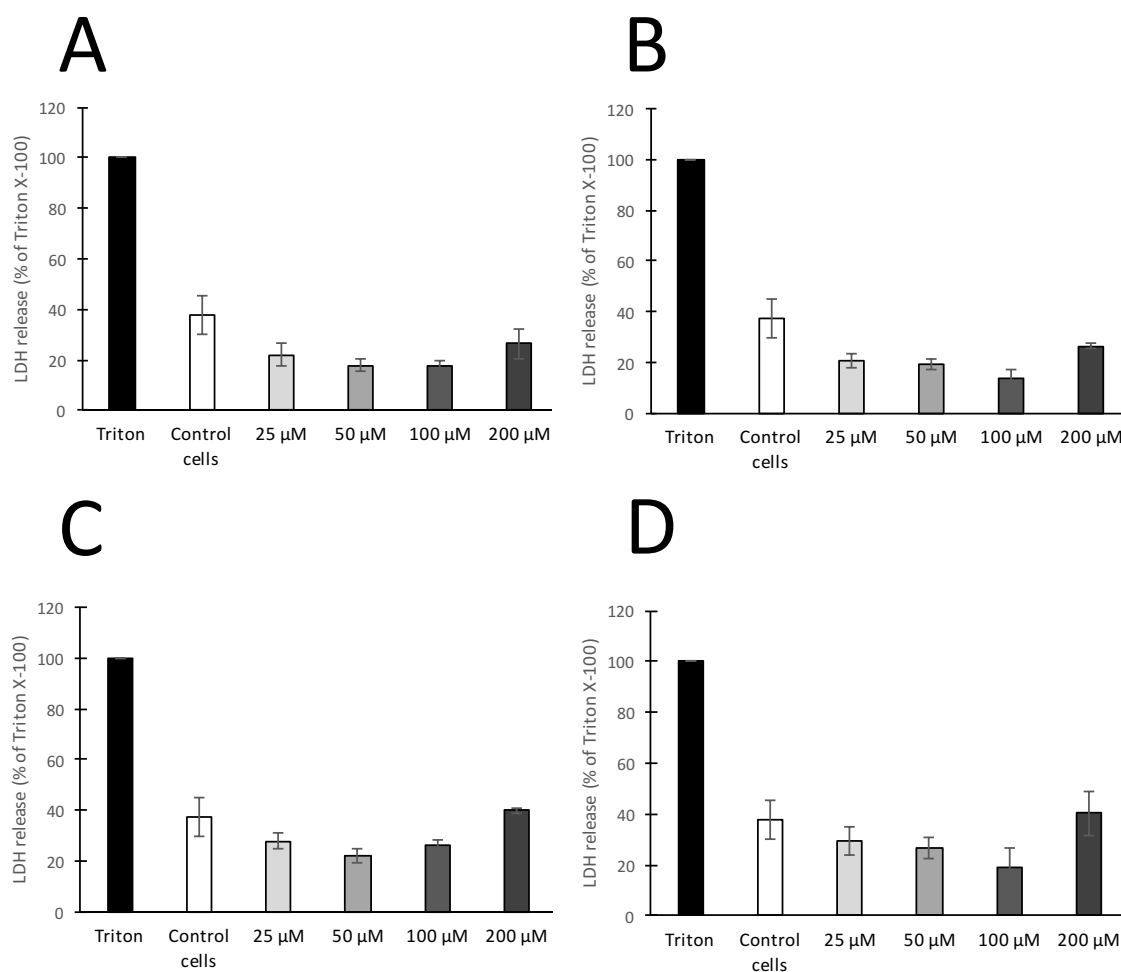


Figure 37: Cytotoxicity of NLC T10-TOC (**A**), NLC C10-TOC (**B**), NLC P10-TOC (**C**) and NLC S10-TOC (**D**) evaluated by LDH release from HaCaT cells in the media after 24 h of treatment. Data are expressed as percentage LDH release as compared to the maximum release of LDH from Triton-X100-treated cells. Data are the mean \pm sd of three independent experiments with at least three technical replicates at each time

7.2.6. Antioxidant effect of NLC containing TOC

Following results obtained in the 2D cell model, the study of the protective effect of NLC T10-TOC was carried out on human skin explants (HSE).

CS contains many components able to elicit oxidative stress, which can induce the cytoprotective enzyme heme oxygenase (HO-1). HO-1 increase promotes protection against inflammation and/or cell death induced by CS (Abraham and Kappas, 2008; Atzori et al., 2004). In order to evaluate the effect of NLC T10-TOC in preventing damage caused by CS, the HO-1 expression was evaluated on culture of HSE exposed to CS or to air for 24 h. Namely HO-1 has been determined by Western blot analysis, quantified by densitometry and normalized to beta-actin level

for each sample (Figure 38 A). The mean relative density ratios of three experiments are shown in Figure 38 B.

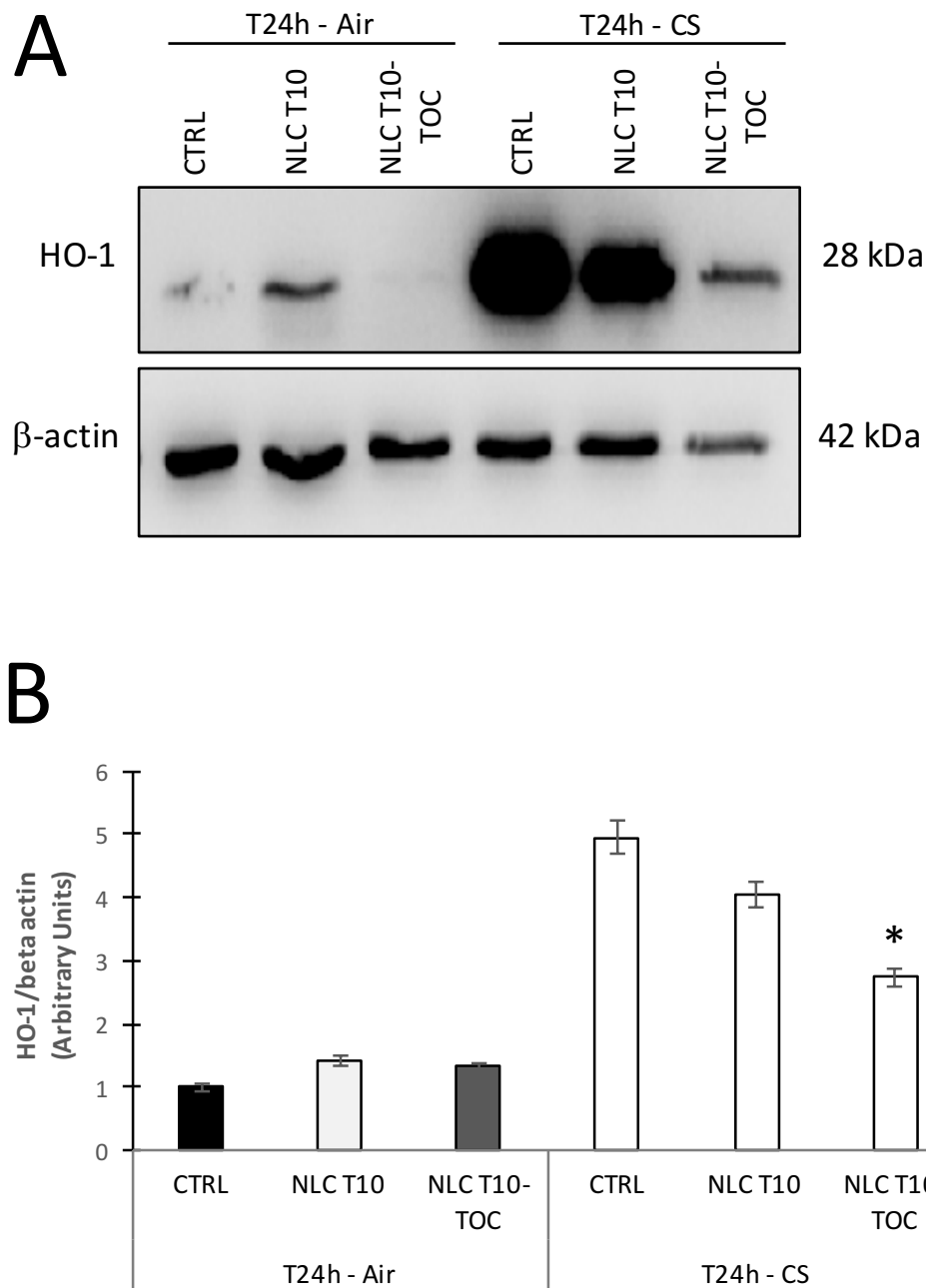


Figure 38: Effect of cigarette smoke (CS) on heme-oxygenase (HO-1) expression evaluated on human skin explants (HSE) treated with NLCT 10 or NLCT 10-TOC, exposed to air or CS for 30 min and harvested after 24 h. Representative Western blot analyses of HO-1 protein expression (with the respective β -actin controls) (A). Mean expression of HO-1 as a ratio of β -actin (B). Results are shown as mean of 3 experiments. * $p < 0.05$ respect to the control

As depicted, the expression of HO-1 protein level is significantly induced by the CS exposure, because of the ability of this outdoor stressor to promote oxidative-related cellular modifications to the skin (Esposito et al., 2008). On the other hand, HO-1 levels in skin explants treated with NLC T10-TOC and exposed to CS were dramatically and significantly prevented (47% decrease, $P < 0.001$ vs control).

These results suggest that NLC T10-TOC can reduce the induction of cutaneous HO-1 that is a sensor of tissue stress, suggesting the ability of this topical application to prevent CS induced skin damage. Further studies will be required to investigate the dose and type-dependent manner of action of TOC loaded in NLC with respect to an unloaded TOC solution.

8. LIPID BASED NANOPARTICLES FOR THE DELIVERY OF UBIQUINONE

8.1. INTRODUCTION

Rett syndrome (RTT) is a severe neurodevelopmental disorder that affects the female gender with a frequency of approximately 1:10,000 live births (Gold et al., 2014). During the first 6-18 months of life, patients have a normal early developmental period and the classical clinical picture shows an early neurological regression followed by the development of autistic behavior, characterized by rapid loss in acquired cognitive, social and motor skills (Pecorelli et al., 2016a).

RTT is caused by mutations in the X-linked Methyl-CpG-binding protein 2 (MECP2) gene but the pathogenic mechanism that links MECP2 dysfunction to disease expression is still under investigation (Pecorelli et al., 2016b).

However, over the last years researchers demonstrated a strong correlation between oxidative stress (OS) and RTT, as indicated by high levels of 4-hydroxy-2-nonenal (4HNE) protein adducts (Cervellati et al., 2015). 4HNE is a reactive electrophilic α,β -unsaturated aldehyde, a reactive lipid mediator generated from oxidative stress-induced lipid peroxidation. Because of its reactivity, 4HNE is able to bind and modify nucleophilic protein residues via Michael addition or to form a Schiff's base with the addition of the aldehydic group to an amino group of the protein (Castro et al., 2017). Recent studies conducted on fibroblasts, demonstrated that 4HNE protein adducts significantly increase in RTT cells respect to healthy control fibroblasts, and this result has been demonstrated also in animal and ex-vivo models (Pecorelli et al., 2011; Sticozzi et al., 2013).

Nowadays, no treatments can arrest the neurological regression in the disease, thus the modulation of OS represents the strategy aimed at improving patient quality of life (De Felice et al., 2009). The involvement of antioxidant molecules able to reduce reactive oxygen species (ROS) generation could represent the therapeutic approach of this study.

Coenzyme Q10 (CoQ10) is a lipid-soluble antioxidant and it is largely distributed in all cell membranes, essential for the prevention of lipid peroxidation. In its oxidized form, known as Ubiquinone (Ub-O) (*Figure 39 A*), plays a central role in the

mitochondrial electron transport chain transporting electrons between complexes I/II and III to produce ATP (Masotta et al., 2019). Its reduced form, Ubiquinol (Ub-R) (Figure 39 B), is a potent antioxidant and free radical scavenger that provides protection to cell membranes and plasma lipoproteins. CoQ10 reduces mitochondrial ROS generation shuttling between the oxidized and the reduced form (Sharma et al., 2012).

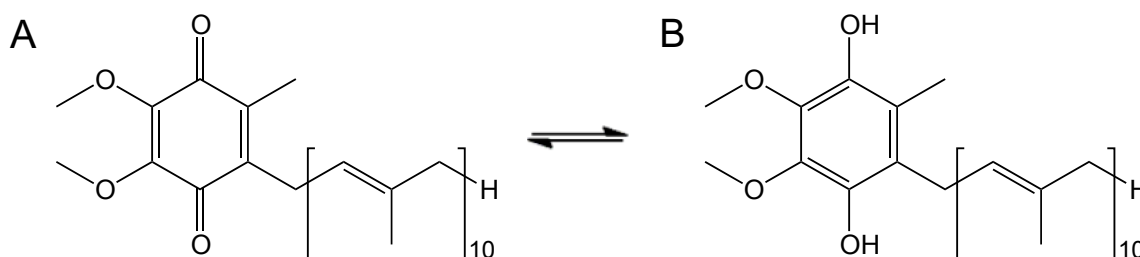


Figure 39: Chemical structure of Ubiquinone (Ub-O) (A) and Ubiquinol (Ub-R) (B)

The low solubility of CoQ10 and its photo-instability led to the development of novel delivery systems in order to preserve the activity of the drug. The topical administration of CoQ10 onto nasal mucosa was considered in order to reach brain tissues via nose to brain drug transport pathway (Shelke et al., 2016) and to increase compliance considering the age of the young patients.

Nanostructured lipid carriers (NLC) described in this chapter were selected for encapsulating Ub-O. After a preformulative study, the stability of produced NLC was evaluated in time. Despite the absence of cytotoxicity on human fibroblasts, the lack of stability in terms of encapsulation efficiency, suggested the development of another lipid based drug delivery system, namely ethosomes (ETHO). The ability of ETHO to improve the solubilization of Ub-O and its activity was investigated. To assess the effect of encapsulated Ub-O in protect cells against OS, immunocytochemical analysis has been performed on human fibroblasts, evaluating 4HNE production.

8.2. RESULTS AND DISCUSSION

8.2.1. Preparation and characterization of lipid nanoparticles containing Ub-O

In the present chapter, Ub-O was encapsulated into NLC, following the ultrasound homogenization method described in the experimental section.

A preliminary study concerning the composition of NLC was conducted in order to produce a nanoparticulate system suitable for the delivery of an optimal amount of Ub-O. Indeed, NLC were selected as promising delivery system in reason of the presence of a liquid lipid in the formulation that could improve the solubilization of the Ub-O, being fat-soluble and highly hydrophobic (Masotta et al., 2019).

The selection of lipid components was based on the choice of biocompatible and not toxic substances, constituted of fatty acids with different carbon chain lengths.

Firstly, a content of 5% of lipid phase as compared to the total amount of dispersion was used. Particularly, tristearin was employed as solid lipid and coconut oil, composed of saturated fatty acids (about 94%), with a good percentage of medium-chain fatty acids, was employed as liquid lipid. The use of this lipid mixture in the production of nanoparticles led to an increased physical stability, compared to other mixtures (e.g. tristearin/miglyol) previously studied in our research group.

With the aim of producing stable NLC-containing Ub-O, the concentration of the drug was gradually increased, as shown in *Table 26* and its effect on the produced NLC was evaluated on their size during time.

Table 26: Composition of NLC

Formulation	Composition % (w/w)				Ubiquinone (Ub-O) (mg/ml)
	lipid phase		water phase		
	tristearin	coconut oil	poloxamer 188	water	
NLC 5	2.5	2.5	2.37	92.63	-
NLC 5 Ub-O _{0.4}	2.5	2.5	2.37	92.63	0.4
NLC 5 Ub-O _{0.8}	2.5	2.5	2.37	92.63	0.8
NLC 5 Ub-O _{1.5}	2.5	2.5	2.37	92.63	1.5
NLC 5 Ub-O _{3.0}	2.5	2.5	2.37	92.63	3.0
NLC 10	5.0	5.0	2.25	87.75	-
NLC 10 Ub-O _{5.0}	5.0	5.0	2.25	87.75	5.0

In order to overcome drug precipitation, NLC were in a second step produced increasing the lipid phase up to 10%, allowing to encapsulate 5.0 mg/ml of Ub-O. All the produced NLC appear as milky homogeneous light-yellow dispersions free from agglomerates and their stability in terms of size and encapsulation efficiency has been investigated during time.

Table 27 shows the results of dimensional analysis performed on the formulations above described.

Table 27: Dimensional characteristics of NLC containing Ub-O

Time (d)	NLC 5 Ub-O _{0.4}	NLC 5 Ub-O _{0.8}	NLC 5 Ub-O _{1.5}	NLC 5 Ub-O _{3.0}	NLC 10 Ub-O _{5.0}
	Z-Ave (nm) <i>Pdl</i>	Z-Ave (nm) <i>Pdl</i>	Z-Ave (nm) <i>Pdl</i>	Z-Ave (nm) <i>Pdl</i>	Z-Ave (nm) <i>Pdl</i>
1	170.33 ± 28.22 <i>0.43 ± 0.07</i>	122.20 ± 1.13 <i>0.33 ± 0.09</i>	112.10 ± 6.22 <i>0.30 ± 0.08</i>	121.40 ± 0.40 <i>0.42 ± 0.01</i>	70.70 ± 9.90 <i>0.25 ± 0.01</i>
7	171.05 ± 53.25 <i>0.37 ± 0.11</i>	122.85 ± 3.46 <i>0.39 ± 0.13</i>	108.85 ± 0.35 <i>0.32 ± 0.09</i>	139.10 ± 14.10 <i>0.41 ± 0.01</i>	73.80 ± 0.70 <i>0.29 ± 0.04</i>
15	165.70 ± 50.77 <i>0.31 ± 0.07</i>	125.05 ± 7.71 <i>0.38 ± 0.09</i>	112.40 ± 4.67 <i>0.32 ± 0.07</i>	117.10 ± 4.00 <i>0.38 ± 0.07</i>	83.30 ± 17.60 <i>0.29 ± 0.03</i>
30	155.20 ± 46.10 <i>0.37 ± 0.10</i>	124.70 ± 13.2 <i>0.39 ± 0.03</i>	132.00 ± 11.60 <i>0.42 ± 0.05</i>	119.90 ± 5.00 <i>0.36 ± 0.04</i>	76.50 ± 0.60 <i>0.28 ± 0.08</i>

The NLC 5 Ub-O_{5.0} are characterized by mean diameters comprised between 108 and 171 nm, while the mean diameter of NLC 10 Ub-O_{5.0} is around 70 nm. The decreased dimensions of NLC 10 Ub-O_{5.0} is probably due to the higher concentration of coconut oil, leading to more stable formulations also confirmed by polydispersity values. The dimensional distribution of NLC stored at 25°C was evaluated up to 30 days after production and the NLC maintained their mean diameters as well as their appearance almost unvaried.

8.2.2. Encapsulation of Ub-O in NLC

The stability of the NLC during 30 days was evaluated also in terms of encapsulation efficiency (EE) of the Ub-O. As evidenced in Table 28, the EE of the drug the first day after production was higher than 88% for all the formulations, but dramatically decreases over time. Indeed, 30 days after production, the value of EE halved for

all formulations, suggesting the weakness of the NLC to control the encapsulation of the active compound. It can be hypothesized that the instability of Ub-O in NLC has been caused by thermal and mechanical stresses during the production phase. As described in the method section, the high temperature, the high-speed homogenization and the ultrasound gave rise to degradation of the drug resulting in the loss of drug content.

Table 28: Encapsulation efficiency of NLC containing Ub-O

Time (d)	Encapsulation efficiency (%)				
	NLC 5 Ub-O _{0.4}	NLC 5 Ub-O _{0.8}	NLC 5 Ub-O _{1.5}	NLC 5 Ub-O _{3.0}	NLC 10 Ub-O _{5.0}
1	88.69 ± 4.8	104.02 ± 6.1	88.14 ± 0.79	98.78 ± 3.42	91.24 ± 5.69
7	87.35 ± 5.1	97.12 ± 4.9	79.13 ± 1.90	96.88 ± 3.22	81.08 ± 3.13
15	78.16 ± 3.8	78.30 ± 4.5	68.42 ± 3.65	73.87 ± 1.19	63.93 ± 1.71
30	51.38 ± 3.5	52.75 ± 3.2	57.33 ± 5.21	65.29 ± 5.08	58.75 ± 1.22

8.2.3. Cytotoxicity of NLC containing Ub-O

On the basis of dimensional distribution and encapsulation efficiency of the produced nanoparticles, NLC 5 Ub-O_{3.0} and NLC 10 Ub-O_{5.0} have been selected to evaluate the cytotoxicity of the formulations. Primary dermal fibroblasts from healthy control subject were selected for the *in vitro* tests, being the fibroblasts the molecular target of the study (Cervellati et al., 2015).

At first, the evaluation of the cytotoxicity of the empty NLC was assessed in order to confirm the safeness of the novel mixture used in the formulation. *Figure 40* shows the results Trypan blue exclusion, MTT and LDH tests performed with different concentrations of NLC 5 and NLC 10 (with respect of tristearin concentration).

Three different techniques were employed to evaluate the cytotoxicity of the formulations. As depicted in *Figure 40*, no cytotoxicity was observed at different concentrations of NLC 5 and NLC 10. In particular, the LDH assay (*Figure 40 C*) revealed that no differences between cells exposed to NLC treatment and control cells (not treated) were detected in terms of LDH released in the media, confirming the results obtained with Trypan blue exclusion (*Figure 40 A*) and MTT (*Figure 40 B*) assays.

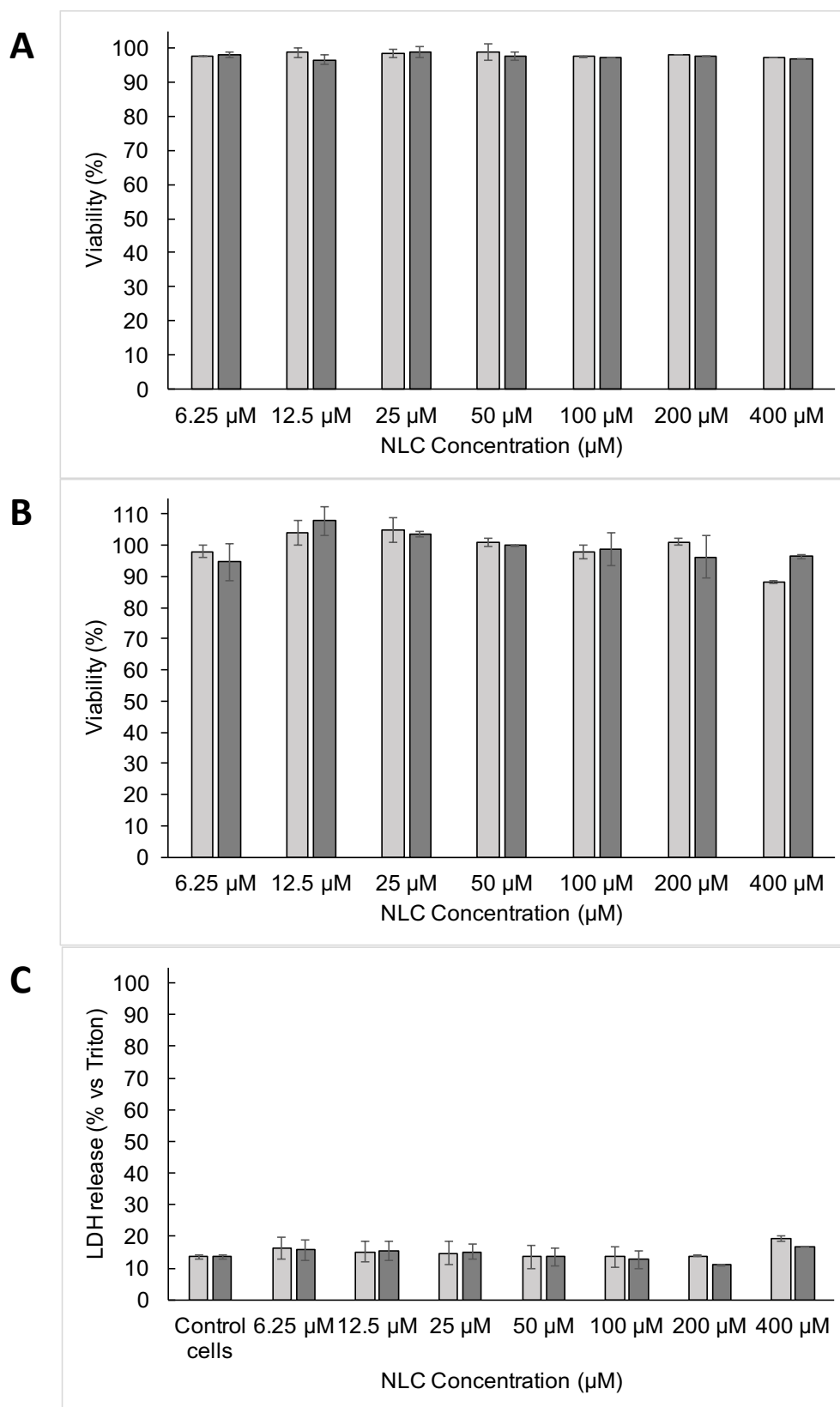


Figure 40: Cytotoxicity of empty NLC 5 (light grey) and empty NLC 10 (dark grey) evaluated by Trypan blue exclusion (**A**), MTT (**B**) and LDH (**C**) tests on Primary dermal fibroblasts from healthy control subject after 24h of treatment. Data are given as mean \pm sd, representative of three independent experiments with at least three technical replicates each time

Furthermore, the cytotoxicity of NLC 5 Ub-O_{3.0} and NLC 10 Ub-O_{5.0} was evaluated and compared with the results obtained with the corresponding empty formulations. As displayed is *Figure 41*, both Trypan blue exclusion (*Figure 41 A*) and MTT (*Figure 41 B*) assays revealed similar results of cytotoxicity of those obtained with the empty NLC. Thus, the encapsulated Ub-O did not induce toxic effects on cells at all concentrations tested.

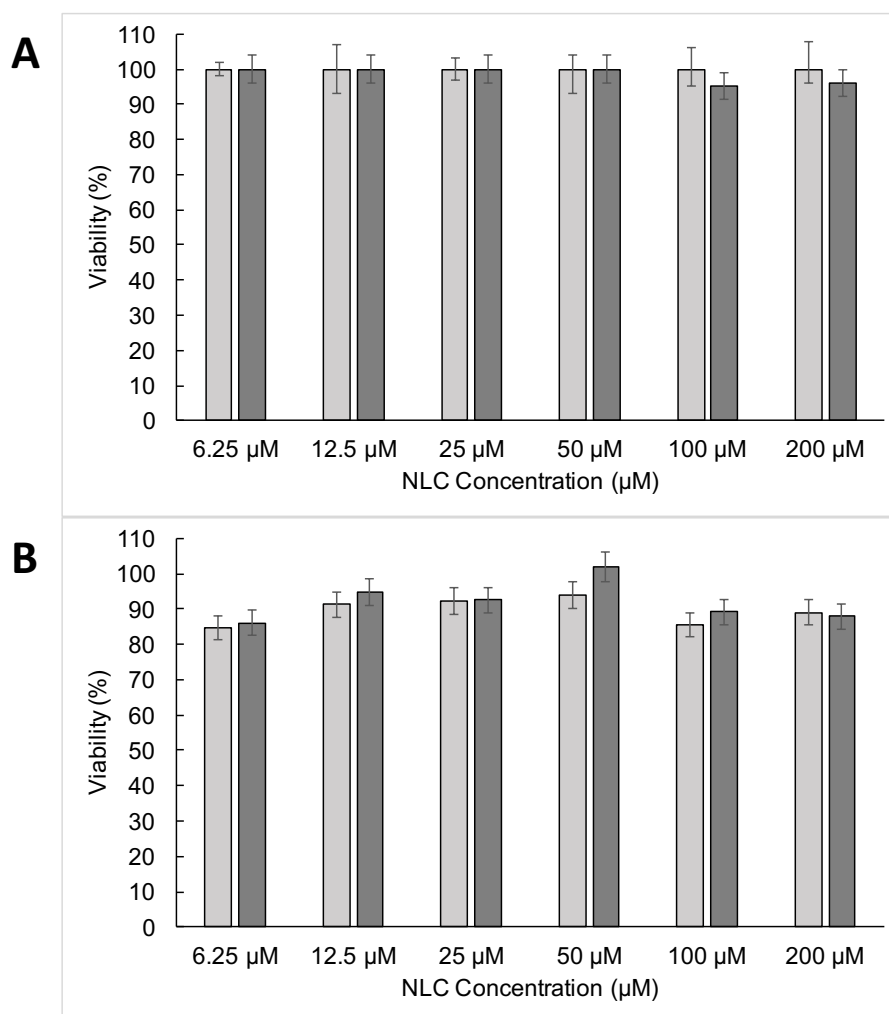


Figure 41: Cytotoxicity of NLC 5 Ub-O_{3.0} (light grey) and NLC 10 Ub-O_{5.0} (dark grey) evaluated by Trypan blue exclusion (**A**) and MTT (**B**) tests on Primary dermal fibroblasts from healthy control subject after 24h of treatment. Data are given as mean \pm sd, representative of three independent experiments with at least three technical replicates each time

Unfortunately, the possible degradation of Ub-O evidenced by the lack of stability in EE, limits the effectiveness of the drug as antioxidant molecule. Indeed, the production method of NLC represent the crucial point of the formulation. For this

reason, the antioxidant effect of the encapsulated active compound was not evaluated and the development of a different formulation strategy was considered. In order to overcome these drawbacks, another drug delivery system, namely ethosome (ETHO), was investigated for the encapsulation of Ub-O.

8.2.4. Preparation and characterization of ethosomes

The production of ETHO containing Ub-O (composed as shown in *Table 29*) was spontaneously obtained by slow addition of water to a soy phosphatidyl choline (PC) ethanol solution under continuous stirring at room temperature (Esposito et al., 2016b).

Table 29: Composition of ETHO

Formulation	Composition % (w/w)			Ubiquinone (Ub-O) (mg/ml)
	Soy phosphatidylcholine	Ethanol	Water	
ETHO	0.9	29.1	70.0	-
ETHO Ub-O	0.9	29.1	70.0	1.0

The active was previously solubilized in PC ethanol solution and it conferred a yellow color to the dispersion (*Figure 42*). Moreover, the production procedure characterized by the absence of high energy input and heating allowed to avoid physico-chemical stresses towards Ub-O weak stability. The resulting nanosystem appeared as a homogeneous formulation, with no agglomerated or precipitation of the drug.

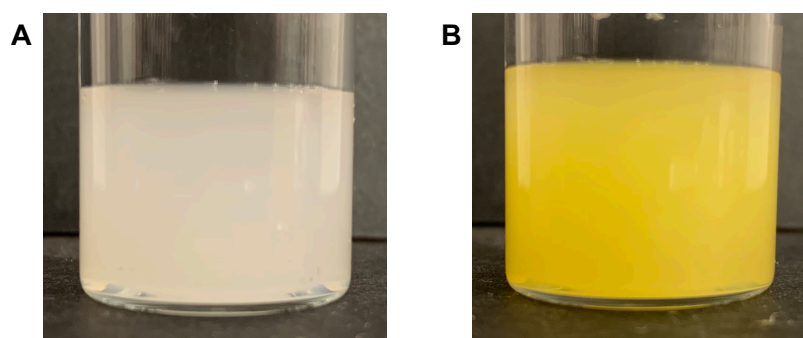


Figure 42: Macroscopic analysis of ETHO (A) and ETHO Ub-O (B)

The morphology of ETHO was investigated by Cryo-TEM and *Figure 43* reports the images of ETHO (**A**) and ETHO Ub-O (**B**). The presence of multilamellar spherical vesicles and multivesicular vesicles was evidenced in both cases.

Thus, the presence of Ub-O in the formulation did not interfere with the supramolecular organization of PC, giving rise to drug loaded vesicles.

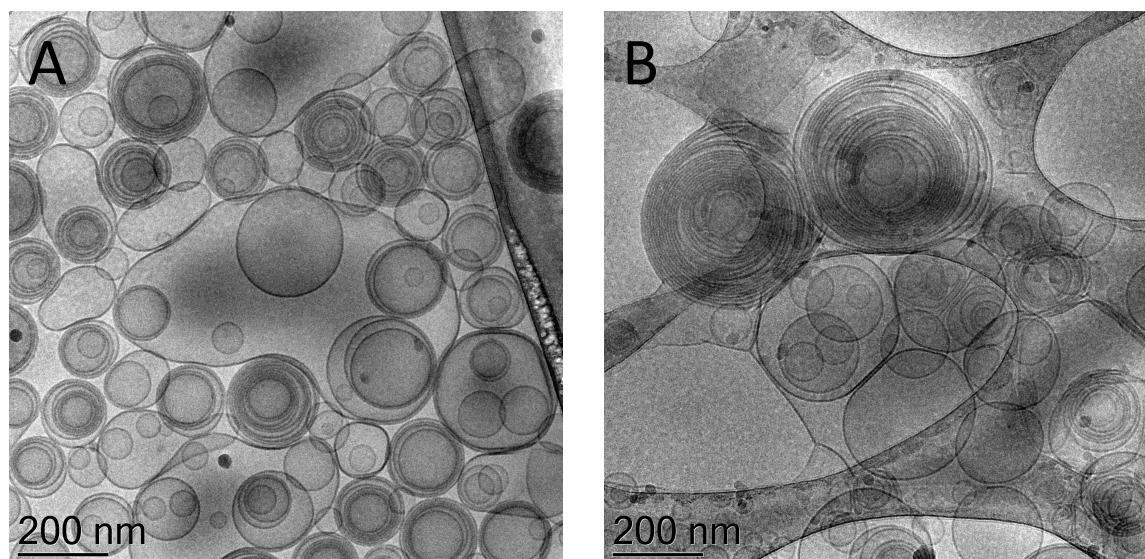


Figure 43: Cryo-transmission electron microscopy images (Cryo-TEM) of ETHO (**A**) and ETHO Ub-O (**B**). Bar corresponds to 200 nm

The dimensional distribution of empty and drug loaded ethosomes was monitored during time by PCS analysis. As summarized in *Table 30*, vesicle mean diameters were stable up to 30 days after production, comprised between 255 nm and 282 nm in the case of ETHO and between 271 nm and 297 nm in the case of ETHO Ub-O. The presence of the drug slightly increased the mean diameter of vesicles, but the dimensional distribution, described by Pdl values, denoted a unimodal distribution up to one month for both formulations.

Table 30: Dimensional parameters of ethosomes as determined by PCS

Time (d)	ETHO		ETHO Ub-O	
	Z-Average (nm)	Pdl	Z-Average (nm)	Pdl
1	255.20 ± 8.10	0.10 ± 0.02	271.20 ± 5.56	0.14 ± 0.01
3	280.95 ± 3.46	0.12 ± 0.05	284.25 ± 11.24	0.16 ± 0.01
7	282.55 ± 17.47	0.12 ± 0.02	292.95 ± 4.59	0.12 ± 0.02
15	282.85 ± 17.18	0.11 ± 0.03	297.60 ± 17.39	0.11 ± 0.02
30	270.70 ± 10.01	0.12 ± 0.03	293.05 ± 17.18	0.16 ± 0.03

8.2.5. Encapsulation of Ub-O in ETHO

In view of producing a suitable nanosystem able to protect Ub-O from degradation and maintain its antioxidant effect, the stability of Ub-O encapsulated in ETHO has been determined in time and expressed as percentage with respect to the total amount of drug loaded in the formulation (*Table 31*).

Table 31: Ub-O encapsulation efficiency in ETHO, evaluated 1, 7, 15 and 30 days after production by HPLC

Time (d)	Encapsulation efficiency (%)
1	102.38 ± 0.84
7	100.98 ± 0.26
15	96.13 ± 1.13
30	90.24 ± 1.70

The Ub-O EE values were almost quantitative of the total amount of drug used for the preparation during the time storage at 25°C. Indeed, 30 days after production, the drug recovery decreased from 102 to 90%, confirming the stability of the formulation already suggested by the dimensional studies and the visual inspection. It should be noticed that the hypothesis of physico-chemical degradation of the drug caused by the ultrasound homogenization method used to produce NLC was corroborated by comparing the results of EE of ETHO Ub-O with those obtained with NLC Ub-O.

In the reason of the higher stability of ETHO Ub-O, this formulation was considered to evaluate the *in vitro* cytotoxicity and the evaluation of the antioxidant activity on fibroblasts.

8.2.6. Cytotoxicity of ETHO containing Ub-O

The *in vitro* cytotoxicity of ETHO Ub-O has been assessed on the same cell line employed for NLC, namely fibroblasts from healthy control. Thus, Trypan blue exclusion, MTT and LDH assays have been performed with different concentrations of ETHO Ub-O (with respect of encapsulated Ub-O). Starting from the results of NLC cytotoxicity, the range of concentrations was selected in order to confirm the biocompatibility of this novel drug delivery system and the encapsulated active.

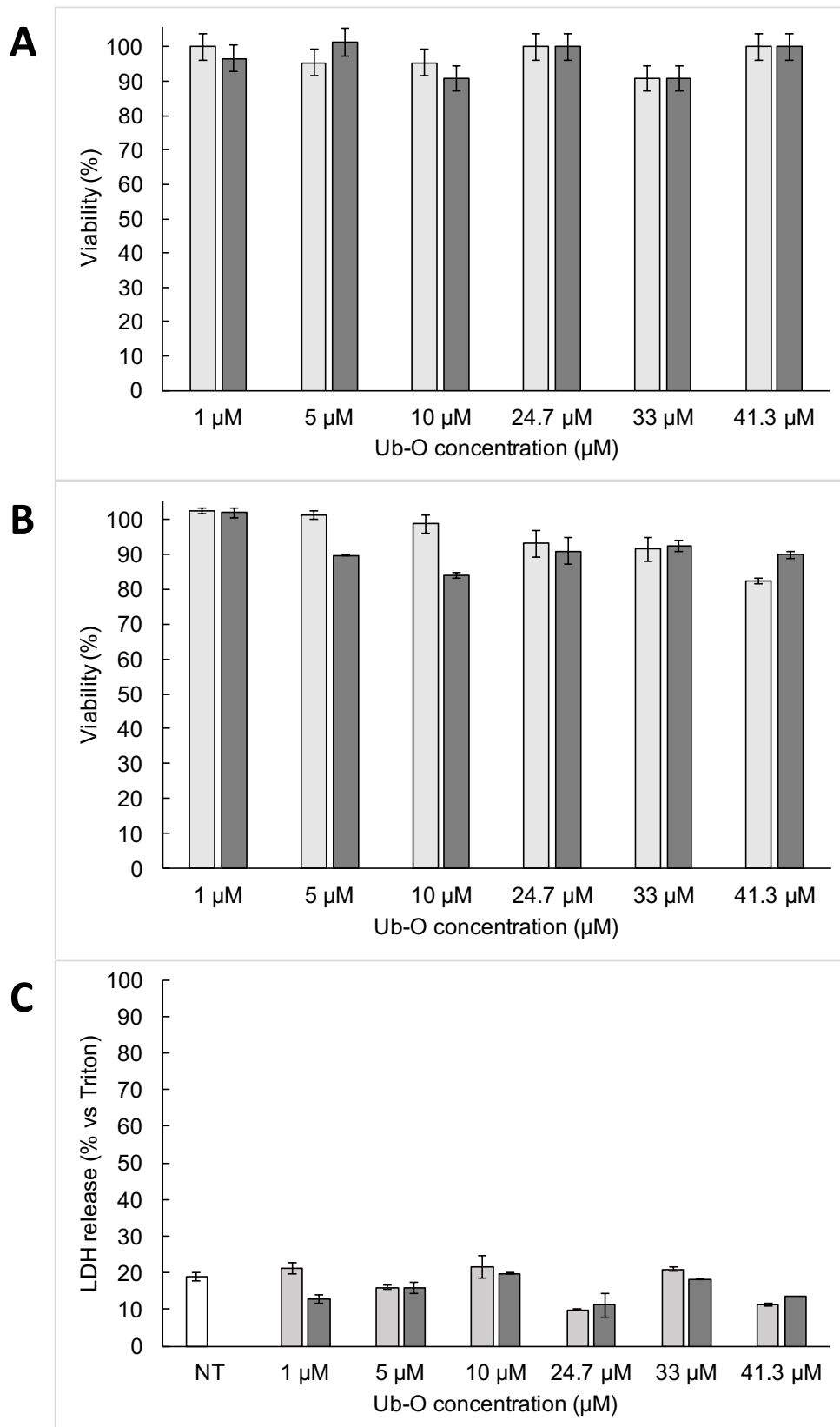


Figure 44: Cytotoxicity of ETHO (light grey) and ETHO Ub-O (dark grey) evaluated by Trypan blue exclusion (**A**), MTT (**B**) and LDH (**C**) tests on primary dermal fibroblasts from healthy control subject after 24h of treatment. Data are given as mean \pm sd, representative of three independent experiments with at least three technical replicates each time

Figure 44 displays the results of cytotoxicity obtained with the techniques mentioned above, comparing the empty vehicle to the drug loaded formulation. Both formulations display the same behavior without cytotoxicity up to the highest concentration tested. In detail, cell viability detected by Trypan Blue exclusion assay (*Figure 44 A*) was higher than 90% for both ETHO and ETHO Ub-O for all concentrations. Moreover, MTT (*Figure 44 B*) and LDH (*Figure 44 C*) assays confirmed the absence of cytotoxicity, resulting in a cell viability of 82% and 89%, in the case MTT assay, in 11% and 13% of LDH release for ETHO and ETHO Ub-O respectively.

Based on these data, the highest concentration, being 41.3 μM of Ub-O encapsulated into ethosomes, was selected for further *in vitro* experiments.

8.2.7. ETHO uptake in fibroblasts detected by TEM

In order to investigate the uptake of ETHO in treated fibroblasts, TEM analysis was performed comparing the ultrastructural morphology with untreated cells.

Since ethosomes represent the second generation of liposomes, the mechanisms of interaction between liposome and cell could be considered to better understand the internalization of ETHO into fibroblasts. The main liposome-cell interactions involved are the exchange of lipids with cell membranes, the adsorption of liposomes to cells, the internalization by endocytosis or phagocytosis and the fusion of bound liposome bilayer with the cell membrane (Akbarzadeh et al., 2013).

Focusing on cell membrane section displayed in *Figure 45*, at the two experimental conditions and at different magnifications, the passage of ETHO is clearly evidenced in panels C and D. Moreover, the involvement of endocytosis pathway could be supposed for the presence of cell membrane invaginations and vesicles within the cytoplasm.

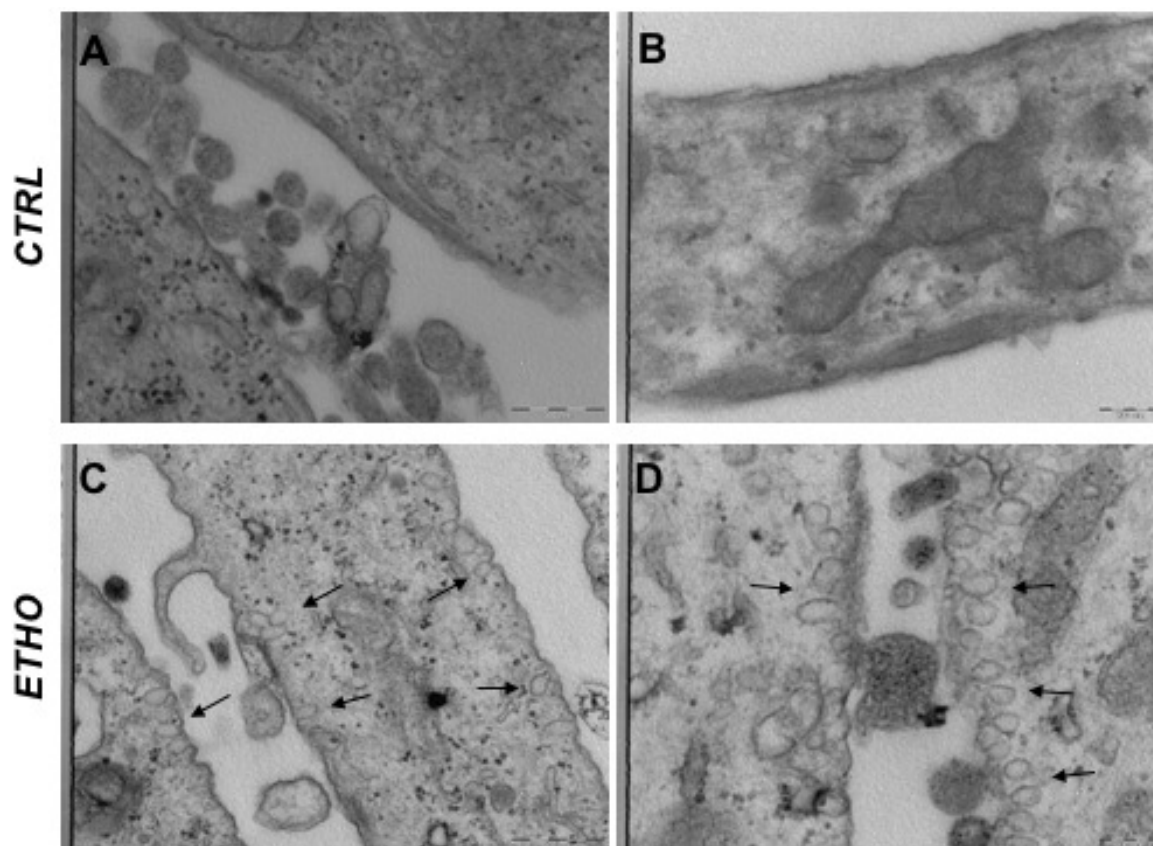


Figure 45: TEM images of control cells (A, B) and cells treated with ETHO (C, D). Images of panels A and C refer to 31.5K magnification; images of panels B and D refer to 50K magnification. Arrows indicate the presence of ETHO. Bar correspond to 500nm in panels A and C and 200 nm in panels B and D

Furthermore, comparing the images with those of untreated cells, the ultrastructural morphology of fibroblast is not affected by the presence of ETHO.

Taking together the results of cytotoxicity and TEM, ETHO appeared as promising nanoparticulate systems able to deliver the Ub-O to the target cell with the aim of enhancing the cellular antioxidant defense status.

8.2.8. Evaluation of 4HNE protein adducts levels in fibroblasts treated with ETHO Ub-O by Immunocytochemistry analysis

As well reported in literature, the high levels of 4HNE protein adducts in RTT fibroblasts is related to increased lipid peroxidation and OS in patients (Sticozzi et al., 2013).

In order to investigate the effect of the Ub-O delivered by ETHO in protecting cells against oxidative insults, an immunocytochemical analysis for 4HNE protein adducts has been performed on human health fibroblasts treated with H_2O_2 as an inducer of oxidative stress.

Briefly, untreated cells (CTRL), cells treated with empty ETHO and cells treated with ETHO Ub-O 41.3 μM have been exposed to 50 μM of H_2O_2 for 1 hour and 4HNE protein adducts levels have been evaluated after 2 and 6 hours of exposure.

4HNE protein adducts were analyzed by immunofluorescence (Figure 46 A) and quantified with respect to untreated cells (Figure 46 B).

Comparing the results with those of cells not subjected to oxidative insult (data not shown), the exposure with 50 μM of H_2O_2 induced a significant increase in 4HNE protein adducts formation (green fluorescence), in CTRL and ETHO cells (Figure 46 A). On the other hand, when cells exposed to H_2O_2 were pre-treated with Ub-O delivered by ETHO, the formulation was able to counteract the formation of 4HNE protein adducts, as indicated by the reduction in green fluorescence signal intensity (Figure 46 A).

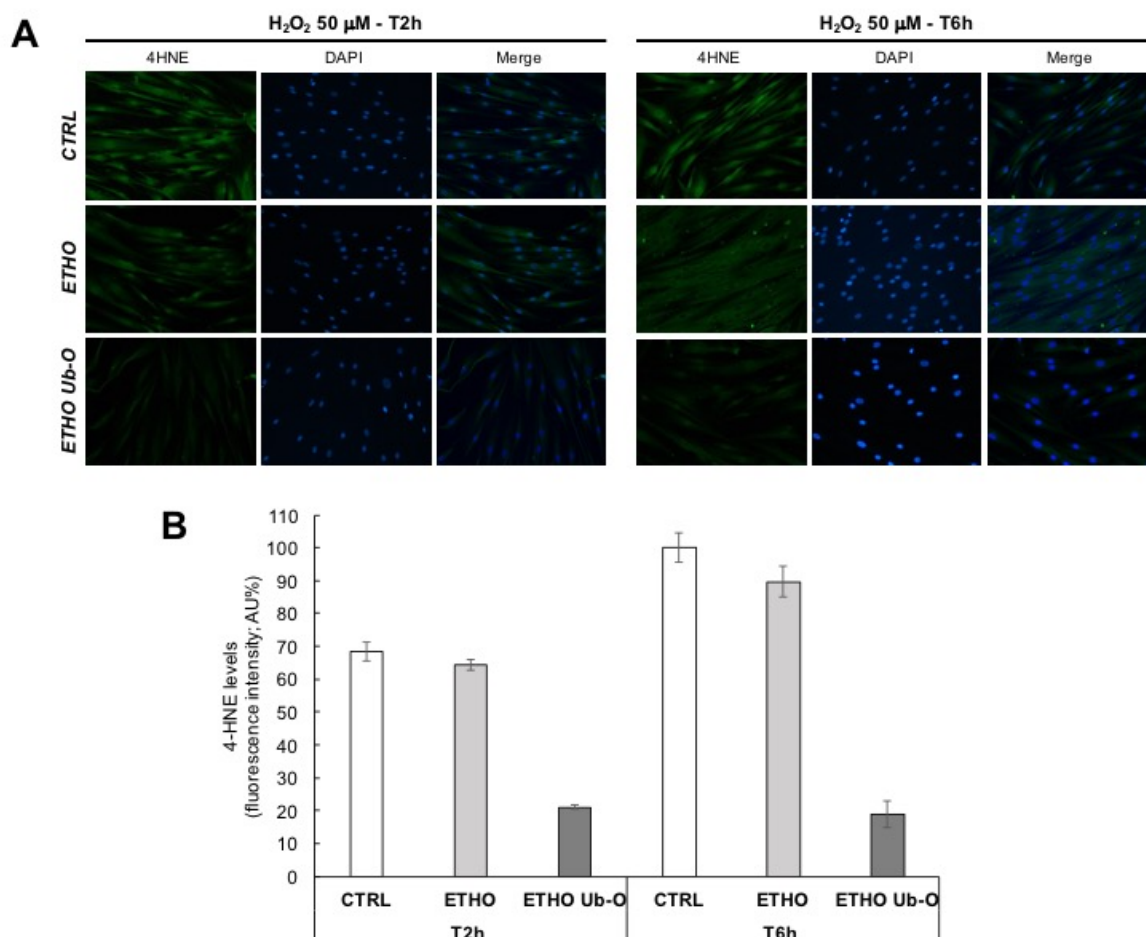


Figure 46: Representative images of immunocytochemistry for 4HNE protein adducts in primary dermal fibroblasts from healthy control at 20x under the various experimental conditions (A). Quantification of immunofluorescence signal for 4HNE protein adducts in the various experimental conditions (B). Data were normalized with respect to the CTRL cells at T6h and expressed as arbitrary units \pm sd

As displayed in *Figure 46 B*, after H₂O₂ exposure, the levels of 4HNE protein adducts in ETHO Ub-O treated cells were maintained around 20% at both time points, while the production of 4HNE protein adducts increased significantly over time in untreated cells.

This result corroborates the role of extracellular Ub-O as antioxidant molecule (Takahashi and Takahashi, 2019) and the drug-targeting delivery achieved with ETHO formulation represents a new achievement in the treatment of cellular dysfunction.

Further studies will be required to perform the encapsulation of Ub-R into ETHO in order to enhance the activity of the drug. In addition, future investigations will clarify the efficacy of ETHO Ub-O formulations in the rescue of the intracellular redox imbalance, already present in RTT fibroblasts (Pecorelli et al., 2016b; Valacchi et al., 2017b).

9. GALLIC ACID LOADED POLOXAMER GELS AS A NEW ADJUVANT STRATEGY FOR MELANOMA: A PRELIMINARY STUDY

9.1. INTRODUCTION

Skin and mucous membranes can be affected by a number of tumors, including melanoma and cervical cancer. Cutaneous melanoma is the most aggressive skin cancer, responsible of 50,000 deaths/year all over the world (Leonardi et al., 2018). Melanoma treatment is usually based on surgery, radiotherapy and chemotherapy. Typically, for the treatment of cutaneous melanoma with a high risk of recurrence, the adjuvant approach can be proposed, aiming to improve the prognosis of the disease after complete resection of the primary melanoma. Nature offers a wide range of compounds with therapeutic properties, among them, some polyphenols, such as gallic acid (3,4,5-trihydroxybenzoic acid, GA) (Figure 47), possess many therapeutic activities including antioxidant, anti-inflammatory, antimicrobial, antiviral and anticancer (Badhani et al., 2015). Particularly some studies have recently demonstrated the GA antiproliferative and anti-apoptotic properties in human melanoma and uterine cervix cells (Badhani et al., 2015; Lin, 2010). In addition, some researchers have attributed to GA wound healing properties (Yang et al., 2016).

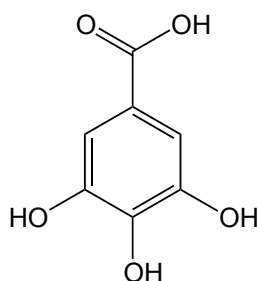


Figure 47: Chemical structure of Gallic Acid

The treatment of cutaneous and mucosal diseases could be achieved by topical application of semi-solid systems constituted of biocompatible polymeric matrices. Notably, the non-ionic poly(oxyethylene)poly(oxypropylene) (PEO-PPO) block

copolymer poloxamer 407 possesses smart properties, passing from a low viscosity sol to a transparent viscous gel above $T_{\text{sol-gel}}$ (Baloglu et al., 2011; Dumortier et al., 2006). This stiff hydrogel, characterized by a closely packed micellar system, is effective for lipophilic and hydrophilic drug delivery (Grinberg et al., 2018; Sarkar et al., 2013). The peculiar thermo-reversible character of poloxamer gels makes them suitable for administration on skin and mucosae, indeed they can be applied as a flowing micellar solution, afterwards, at body temperatures, their viscosity increases, forming long-lasting, semi-solid vehicles (Bodratti and Alexandridis, 2018; Oh et al., 2004). In order to design a semi-solid form suitable for application on the skin, some properties influencing cutaneous application should be considered, such as rheological behavior, as well as spreadability. In addition, *in vitro* diffusion test should be conducted by the use of Franz cell system, in order to predict drug permeability after application of the semi-solid form on the skin (Ng et al., 2010b). Diffusion results strongly depend on the choice of the employed membrane, namely natural or synthetic membranes (Clément et al., 2000). Recently, research efforts have been devoted to find synthetic membrane systems suitable to reproduce the natural stratum corneum (Bartosova and Bajgar, 2012; Karadzovska et al., 2013). For instance, Strat-M[®] is constituted of multiple polymeric layers with different diffusivity, namely two polyether sulfone layers resistant to diffusion and one polyolefin bottom layer more open to diffusion. These overlapped layers generate a porous structure offering a controlled diffusivity. The whole system is impregnated with synthetic lipids conferring further skin-like features (Haq et al., 2018).

The present study aims to (i) design poloxamer gels for GA topical application and (ii) select a membrane system to mimic GA skin permeability by Franz cell. In this view synthetic membranes have been employed, singularly or as combined systems, and compared to a natural membrane. Furthermore, to gain information on the suitability of the GA gels in the treatment of cell migration, *in vitro* assays have been conducted on human keratinocytes (HaCaT cells) and melanoma cells (SK-Mel 28).

The present results have been the object of the published paper: “Gallic acid loaded poloxamer gel as new adjuvant strategy for melanoma: A preliminary study” [Sguizzato M., Valacchi G., Pecorelli A., Boldrini P., Simelière F., Huang N., Cortesi R., and Esposito E. “Gallic Acid Loaded Poloxamer Gel as New Adjuvant Strategy for Melanoma: A Preliminary Study.” *Colloids and Surfaces B: Biointerfaces* 185 (2020): 110613. <https://doi.org/10.1016/j.colsurfb.2019.110613>].

9.2. RESULTS AND DISCUSSION

9.2.1. Gel preparation and characterization

A preformulation study has been conducted to produce a vehicle suitable for GA application on the skin. The vehicle should (a) solubilize GA (solubility in water 1.19 mg/ml), (b) be easily applied on the skin after melanoma resection, (c) remain at the site of application and (d) achieve GA prolonged release. We chose to employ the smart copolymer PEO-PPO-PEO poloxamer 407, characterized by an amphiphilic surfactant character (Shubhra et al., 2014).

Table 32 reports acronyms and composition of the different produced gels based on poloxamer.

Table 32: Acronyms, compositions and sol-gel temperatures of the produced gels

Acronym	Composition %			T _{sol-gel} (°C) ± sd
	poloxamer 407 (w/w)	water (w/w)	gallic acid (w/v)	
P15	15.0	85.0	-	28.6 ± 1.5
P20	20.0	80.0	-	20.6 ± 0.9
P25	25.0	75.0	-	17.1 ± 0.0
P15-GA5	15.0	85.0	0.5	27.9 ± 1.7
P15-GA10	15.0	85.0	1.0	27.5 ± 0.8
P20-GA5	20.0	80.0	0.5	22.8 ± 1.8
P20-GA10	20.0	80.0	1.0	21.8 ± 1.0
P25-GA5	25.0	75.0	0.5	16.9 ± 1.1
P25-GA10	25.0	75.0	1.0	17.5 ± 1.3

Poloxamer gels enabled to increase GA solubility up to 10-fold with respect to water, reaching 10 mg/ml, as determined by HPLC (section 4.3.3.). In addition the gel transparency allowed to exclude the presence of GA powder crystals by visual inspection, confirming the GA complete solubilization.

Gels were characterized by different viscosity values, as a function of poloxamer concentration and temperature. Notably, poloxamer in water assembles itself and forms micellar structures characterized by a peculiar thermo-reversible behavior. Indeed, the micellization phenomenon can be related to the poloxamer concentration (critical micellization concentration) at a fixed temperature or to the

increase of temperature (critical micellization temperature or gelation temperature $T_{\text{sol-gel}}$) at a fixed poloxamer concentration. The latter effect is reversible and attributed to a decrease of the PPO block solubility in water upon heating, which leads to the aggregation of Poloxamer 407 molecules into micelles (Dumortier et al., 2006; Ricci et al., 2005; Yu et al., 1992).

i) Rheological study

In order to gain information on the gel behavior upon storage and to predict their changes under application on the skin, rheological studies have been performed. Particularly the viscoelastic behavior of the gels, i.e. the elastic modulus G' and the viscous modulus G'' have been measured. The elastic modulus indicates the solid-like component of elastic behavior, reflecting the stored elastic energy, while the loss or viscous modulus reflects the dissipated loss of energy (Koffi et al., 2006). *Figure 48* displays the elastic modulus G' and the viscous modulus G'' , as a function of temperature for P15 (A), P20 (B) and P25 (C).

In all cases, G' and G'' profiles almost overlapped in the first phase, whilst at a well-defined temperature ($T_{\text{sol-gel}}$) a sudden increase of the moduli was observed, with G' becoming higher than G'' , thus indicating a transition from liquid (sol) to structured (gel) behavior. The highest value of $T_{\text{sol-gel}}$ (28.6°C) was found in the case of P15, followed by P20 and P25 (*Table 32* and *Figure 48*). Indeed, the gelation temperature is reasonably inversely related to the poloxamer concentration, the higher the poloxamer concentration, the sharper the observed transition (Koffi et al., 2006). Above the gelation temperature G' was significantly higher than G'' , indicating an ordered packing of the micelles. This behavior, typical of solid-like structures, suggests that gels were almost purely elastic (Koffi et al., 2006).

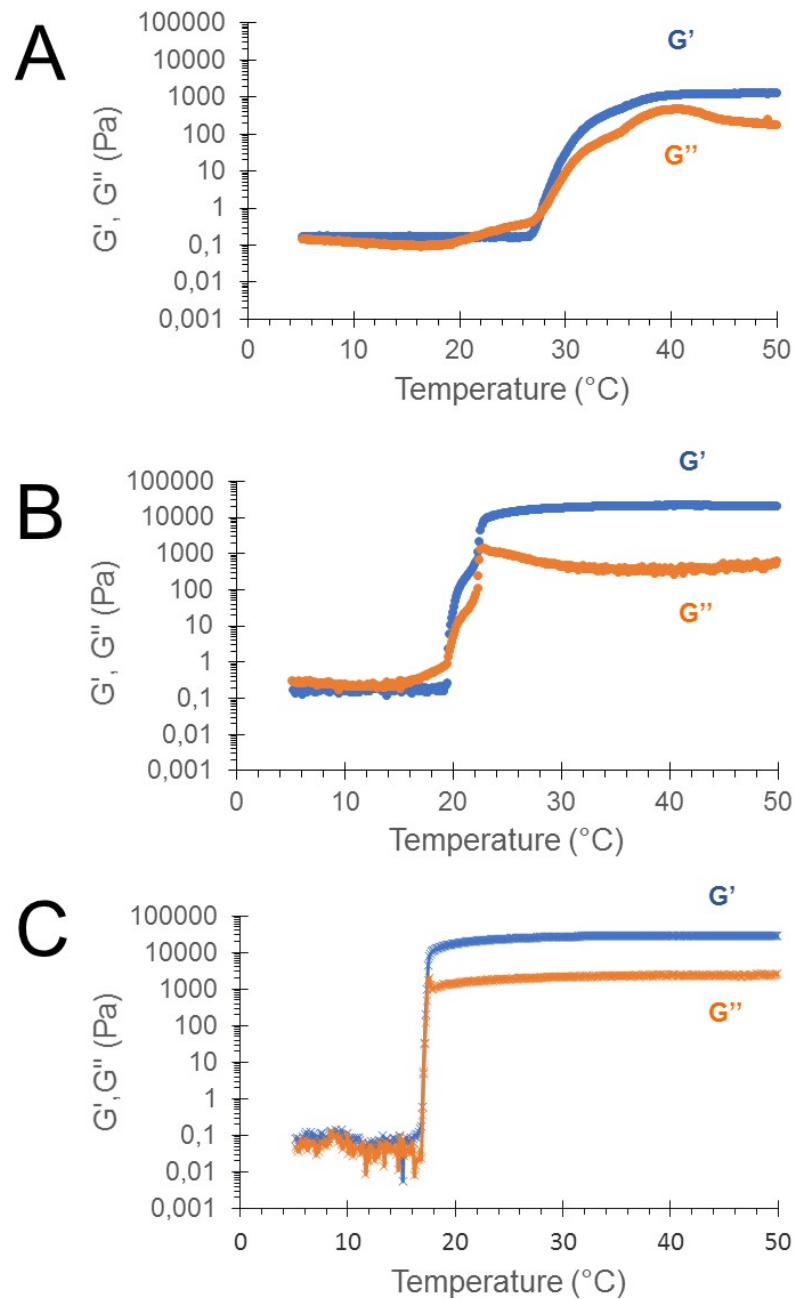


Figure 48: Effect of the temperature on elastic (G') and viscous (G'') moduli for poloxamer gels P15 (A), P20 (B) and P25 (C)

The presence of GA in different amounts (*Figure 49*) did not change the viscoelastic properties of the gels, indicating that poloxamer entirely governed the viscoelastic properties, with no noticeable interactions with GA.

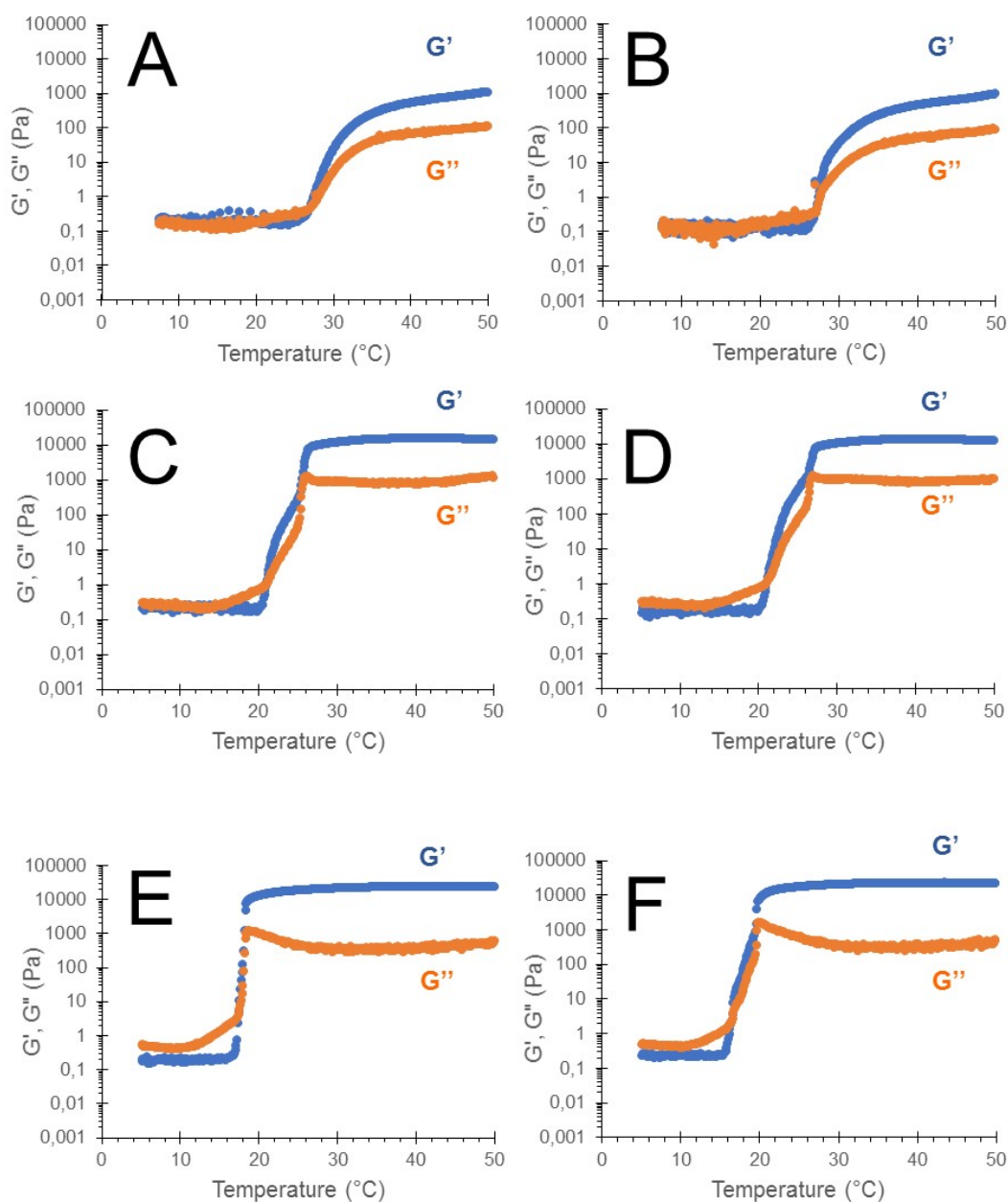


Figure 49: Effect of the temperature on elastic (G') and viscous (G'') moduli for poloxamer gels P15-5GA (A), P15-10GA (B), P20-5GA (C), P20-10GA (D), P25-5GA (E) and P25-10GA (F)

ii) Spreadability study

In order to have information on gel application on skin, the spreadability values of P15-GA10, P20-GA10 and P25-GA10 have been evaluated (Table 33). Indeed, spreadability influences gel extrudability from the package, covering of skin area, patient compliance and finally drug therapeutic efficacy (Esposito et al., 2018b). As expected, the lower the poloxamer concentration, the higher the spreadability.

Indeed spreadability value of P15-GA10 was about 1.5-fold higher than the others. Conversely P25-GA10 was scarcely spreadable. This result agrees with rheological data, indicating that P25-GA10 was not suitable for application on the skin, being too stiff at ambient temperature (25°C). For this reason, the gel was not considered for further diffusion studies.

Table 33: Spreadability and GA recovery of the selected gels

Acronym	spreadability (g x cm / sec)	GA recovery % ^a in gels as a function of time (days)		
		30	60	90
P15-GA10	0.047 ± 0.002	99.1 ± 0.5	96.2 ± 1.7	95.3 ± 2.2
P20-GA10	0.030 ± 0.001	99.2 ± 0.6	97.1 ± 2.2	96.2 ± 3.1
P25-GA10	0.032 ± 0.001	99.1 ± 0.4	98.1 ± 1.8	97.1 ± 1.1

The reported results are the average of four independent experiments ± sd a: as a function of initial GA content

9.2.2 GA stability in poloxamer gels

GA content in the different gels was calculated monthly, up to 90 days, as percentage of the total amount of GA used for the preparation. The obtained results are reported in *Table 33*.

All the gels demonstrated a remarkable efficacy in controlling GA stability. In fact, 3 months after gel production, GA content was higher than 95 %.

The macroscopic aspect of the gels did not change by time; indeed, the gels appeared homogeneous and transparent also after six months from production.

9.2.3 *In vitro* GA diffusion kinetics

i) Selection of membrane system

The *in vitro* GA diffusion was studied by Franz cell, in order to investigate the efficiency of poloxamer gels designed as topical vehicles. With the aim to reproduce drug permeation through the skin, synthetic membranes have been considered, singularly or as combined system, and compared to the natural SCE membrane.

Many factors can affect drug diffusion through synthetic membranes, such as their physicochemical properties, pore size and thickness, thus a preliminary screening aimed at membrane selection was carried out (Simon et al., 2016).

As reported in *Table 34*, mixed esters cellulose, polycarbonate, nylon and polyvinylidene fluoride have been proposed as hydrophilic membranes, while polytetrafluoroethylene as hydrophobic one.

Table 34: Membrane employed for diffusion studies and flux values of GA

Membrane Characteristics				GA* flux (cm/h x 10 ³)
type	character	pore size (μm)	thickness (μm)	
mixed cellulose ester	hydrophilic	0.22	39.63 ^a	249.97 \pm 18.5
polycarbonate	hydrophilic	0.22	7-20 ^b	205.00 \pm 20.5
nylon	hydrophilic	0.22	150-187 ^b	181.92 \pm 17.5
polyvinylidene fluoride	hydrophilic	0.22	100-130 ^b	163.09 \pm 12.1
polytetrafluoroethylene	hydrophobic	0.22	155.6 ^a	3.19 \pm 0.7
polyethersulfone -polyolefin (Strat-M [®])	amphiphilic	n.a.	316.9 ^a	2.86 \pm 0.8
mixed cellulose ester- polytetrafluoroethylene- mixed cellulose ester	amphiphilic	0.22	234.86 ^a	2.07 \pm 0.2
stratum corneum- epidermis (SCE)	amphiphilic	n.a.	20.77 ^a	5.77 \pm 1.0

The reported results are the average of six independent experiments \pm sd

*gallic acid aqueous solution (1 mg/ml); a: as measured by SEM; b: as indicated by the supplier; n.a.: not available

These membranes are commercially available, chemically inert, typically employed for quality control purposes, as recommended by the FDA (FDA Guidance for Industry). Furthermore, to mimic the peculiar stratum corneum structure (Bouwstra and Ponec, 2006), more specialized membrane systems have been employed, namely a sandwich-like membrane system arranged by assembling two hydrophilic membranes separated by one hydrophobic one (cellulose/polytetrafluoroethylene/cellulose) and the commercial Strat-M[®] membrane (Salamanca et al., 2018). This last ultrafiltration membrane is constituted of two polyethersulfone layers that somewhat hinder drug permeation and one more permeable polyolefin layer. These polymeric layers are impregnated with synthetic lipids, providing lipophilic skin-like character to the membrane (Karadzovska and Riviere, 2013).

Figure 50 shows the aspect of membranes analyzed by SEM, viewed on top surface (A, C, E, G) or on edge (B, D, F, H).

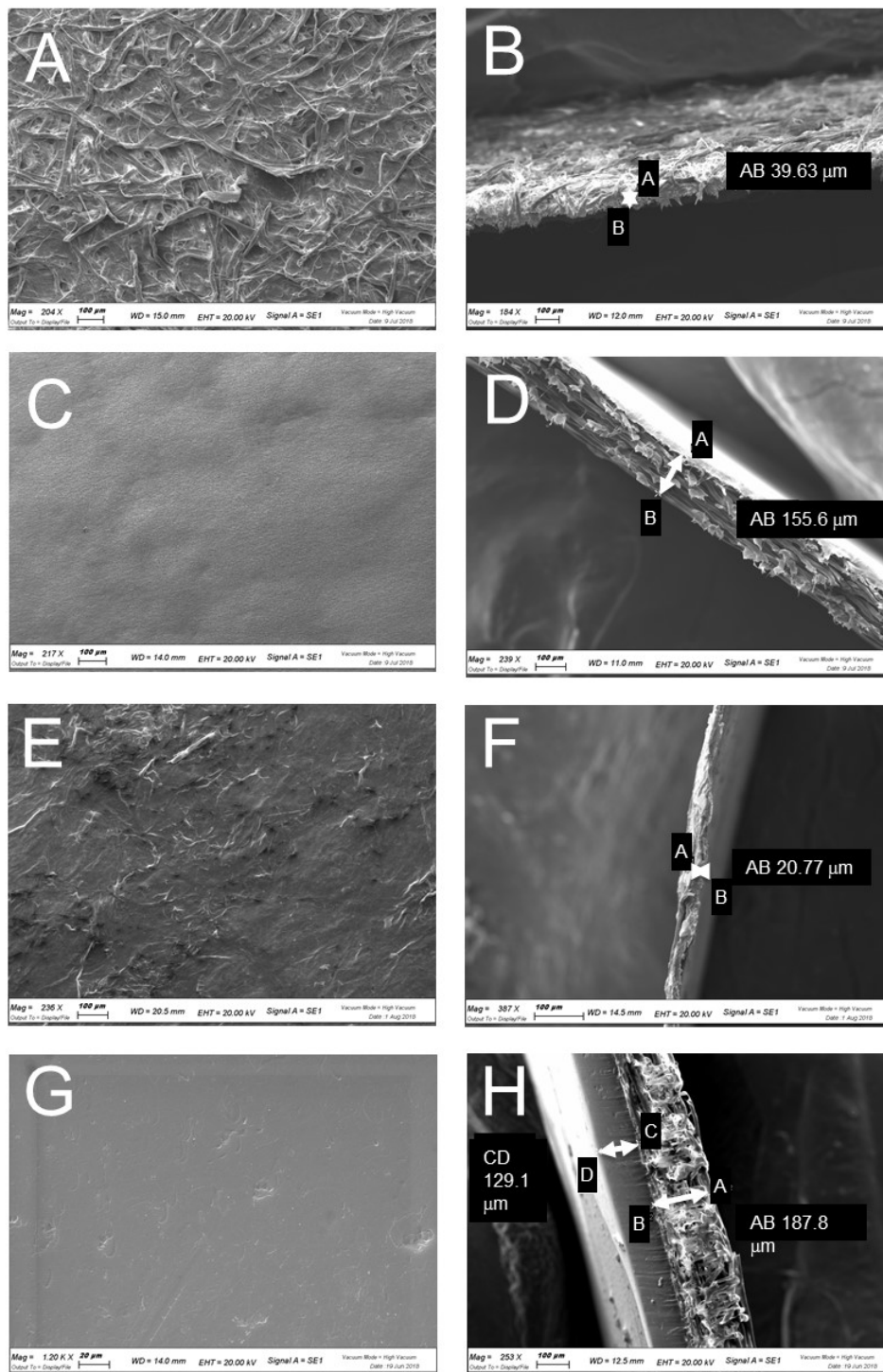


Figure 50: Scanning electron micrographs of membranes employed for Franz cell diffusion tests. Images were taken analyzing top surface (A, C, E, G) or edge (B, D, F, H) of mixed cellulose esters (A, B), polytetrafluoroethylene (C, D), SCE (E, F) or Strat-M® (G, H) membranes. White arrows and black insets indicate the thickness of the membranes. The bar corresponds to 100 μm

The top surface of membrane appeared irregular in the case of mixed cellulose esters and SCE, smooth and homogeneous in the case of polytetrafluoroethylene and Strat-M[®]. Concerning membrane thickness, the finest was found in the case of SCE (20 μm) and the thickest in the case of Strat-M[®] (317 μm). In the case of sandwich system, the thickness was the sum of the single strata (235 μm) (Table 34).

A preliminary study was performed in order to evaluate the effect of the membrane on the diffusion of GA. Particularly the diffusion kinetics of GA aqueous solution (1 mg/ml) through different membranes has been compared (Figure 51, Table 34).

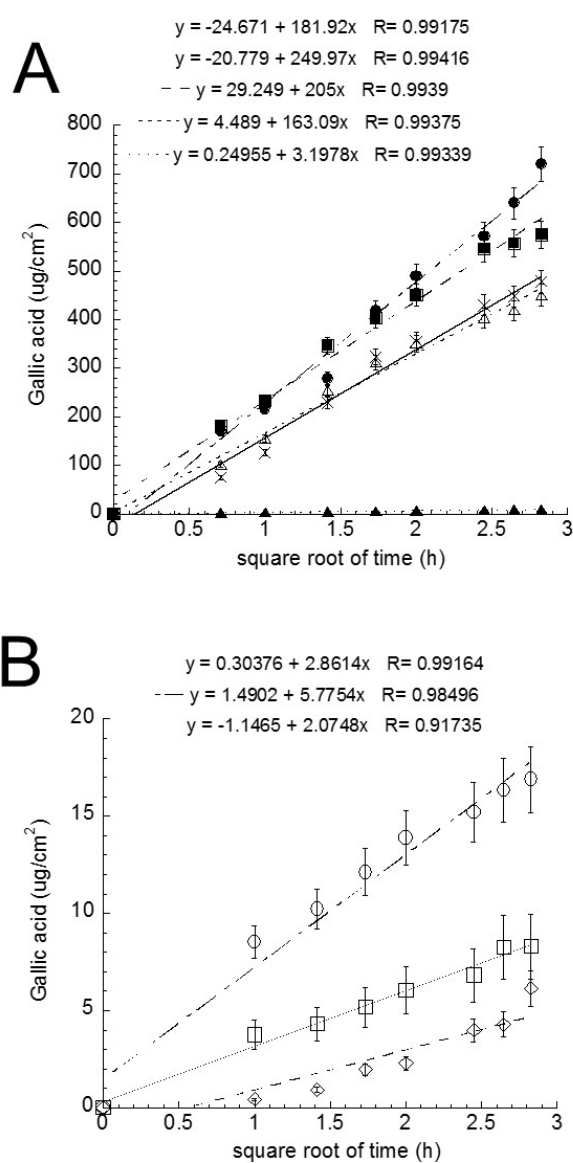


Figure 51: *In vitro* diffusion profiles of GA aqueous solution 1 mg/ml determined by Franz cells associated to mixed cellulose esters (●), polycarbonate (■), polyvinylidene fluoride (△) and nylon (x) membranes (A) and to Strat-M[®] (□), SCE (○), or sandwich (cellulose/polytetrafluoroethylene/cellulose) (◇) membranes (B). Data represent the mean of six independent experiments \pm S.D

As first approach, the single membranes have been employed and compared with SCE. Very different flux values have been found, spanning from 3.19 to 249 cm/h x 10³. Thus, some membranes in some extent acted as rate-limiting to GA diffusion (Ng et al., 2010a). Namely, hydrophilic membranes allowed a faster GA diffusion, whilst the hydrophobic polytetrafluoroethylene membrane displayed a very lower diffusion profile, close to that obtained by SCE (*Figure 51 A, Table 34*). Some authors have suggested that the chemical affinity between compound and membrane can affect the diffusion, indeed hydrophilic molecules diffuse faster through hydrophilic membranes than through hydrophobic ones (Clément et al., 2000). Since GA can be identified as an amphiphilic compound (logP 0.7), in this case the membrane character should not strictly affect the molecule diffusion (PubChem).

As a second approach, GA diffusion through the specialized membrane systems was evaluated and compared with SCE (*Figure 51 B, Table 34*). Flux values were generally lower with respect to those obtained by single hydrophilic membranes. Namely, the sandwich-like system led to a 50-fold decrease of GA diffusion, as compared to the single mixed cellulose membrane, resulting in a flux value resembling those obtained by Strat-M[®] and SCE membranes. Importantly, the GA fluxes for Strat-M[®], sandwich and SCE were very close each other, irrespectively of the differences in membrane thickness. Concerning membrane pores, in the case of SCE and Strat-M[®], due to the complexity of their heterogeneous structure, the pore size has not been evaluated. Nevertheless, since stratum corneum is characterized by tortuosity of pores (Pierard et al., 2015) a tortuous structure can be hypothesized in the case of SCE. Analogously, in the case of Strat-M[®] and sandwich membrane, the overlapping of different strata could create an irregular tortuous system. Thus, pore tortuosity could account for the similar fluxes found for Strat-M[®], sandwich and SCE. These preliminary results suggest that a combined membrane system could better mimic skin behavior with respect to a single synthetic membrane, namely both sandwich and Strat-M[®] can be employed to reproduce skin performance in diffusion experiments.

ii) Study of GA diffusion from gels

The sandwich-like membrane system was further employed to study GA diffusion from P15-GA10 and P20-GA10 (*Figure 52 A*). Surprisingly, unexpected diffusion

profiles were found, characterized by a sigmoidal curve in the case of P20-GA10 and a faster profile in the case of P15-GA10. In both cases an initial lag time (up to 1 and 2 h for P20-GA10 and P15-GA10 respectively), defined as the time required for the diffusion flow to become stable, was followed by an increase of GA diffusion. In the case of P20-GA10, GA diffusion reached a plateau after 8 h, whilst in the case of P15-GA10, GA diffusion was definitely rapid. These different behaviors should be attributed to the rheological characteristics of the gels at 32°C (i.e. the temperature settled in Franz cell chamber to reproduce physiological skin temperature (Esposito et al., 2014)). Namely G' and G'' values were very higher in the case of P20-GA10 (11,500 and 104 Pa) with respect to P15-GA10 (923 and 15 Pa), suggesting that the higher viscoelasticity of P20-GA10 could be responsible for the slower GA diffusion from this kind of gel. Since $T_{\text{sol-gel}}$ of P20-GA10 is 21.85°C (*Table 32*), at ambient temperature and even more at cutaneous one (Romanovsky, 2014) the gel would be already too stiff, thus hindering its application on the injured skin. Taking into account this consideration, P20-GA10 has not been further studied. Anyway, as expected, viscous forms better control the GA diffusion as compared to the GA solution, indeed GA flux from P15-GA10 in the linear part of the profile was $0.36 \text{ cm/h} \times 10^3$, thus 5.6-fold lower with respect to the GA solution flux calculated by the sandwich membrane (*Table 34*).

The GA diffusion from P15-GA10 was further investigated, comparing the diffusion profiles through the single membrane based on mixed cellulose ester, or the combined membrane systems sandwich, Strat-M[®] and SCE (*Figure 52 B*). In all cases SEM conducted after diffusion studies revealed the integrity of the employed membranes. A steady-state diffusion was observed in the case of the single membrane, (GA diffused at 8 h: $2.7 \text{ } \mu\text{g}/\text{cm}^2$, flux $10^6 \text{ cm/h} \times 10^3$) (insert of *Figure 52 B*), 100-fold faster with respect to combined membrane systems, following non-steady-state profiles. This behavior endorses the hypothesis of a tortuous porosity in the case of combined membrane systems, strongly influencing the molecule diffusion. Particularly, GA diffusion through Strat-M[®] shows an initial lag time (up to 2 h), as in the case of sandwich membrane, followed by a moderate increase (GA diffused at 9 h: $2.9 \text{ } \mu\text{g}/\text{cm}^2$, flux $0.08 \text{ cm/h} \times 10^3$). In the case of SCE, GA diffusion did not undergo a lag-time, instead it was faster in the first 2 h and became slower in the 2-9 h time period. However, the total amount of GA diffused at 9 h through sandwich ($23.8 \text{ } \mu\text{g}/\text{cm}^2$) was comparable to the amount diffused through SCE ($17.7 \text{ } \mu\text{g}/\text{cm}^2$), suggesting the suitability of this membrane system to mimic the skin.

Hence, in addition to the marketed Strat-M[®], also the sandwich system could be employed to get information on diffusion of molecules through skin.

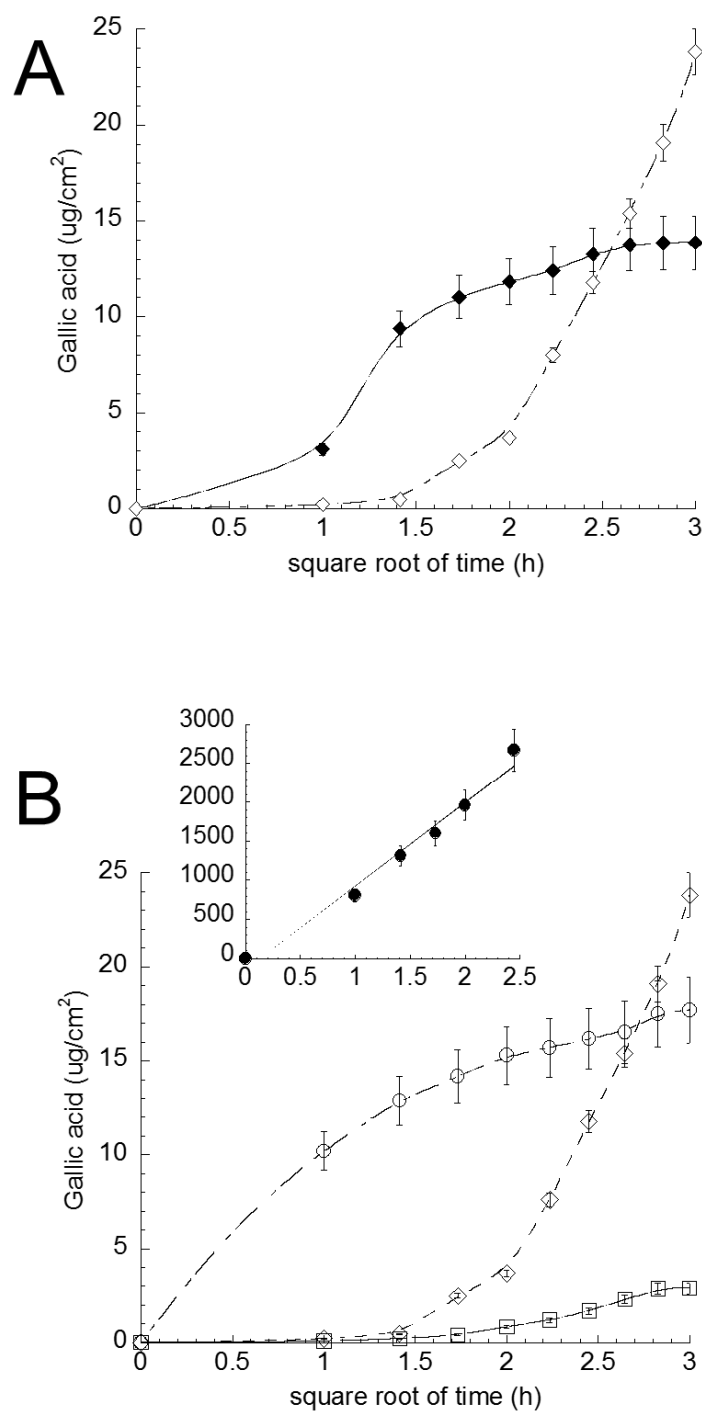


Figure 52: Franz cells diffusion profiles of GA from P15-GA10 (◇) or P20-GA10 (◆) through sandwich (cellulose/polytetrafluoroethylene/cellulose) membranes (**A**). Franz cells diffusion profiles of GA from P15-GA10 through sandwich (cellulose/polytetrafluoroethylene/cellulose) (◇), Strat-M[®] (□), SCE (○) membranes and mixed cellulose esters (●) (insert) (**B**). Data represent the mean of six independent experiments \pm S.D

9.2.4 Biological activity studies

Due to the promising results suggesting the suitability of P15-GA10 to control GA stability and diffusion, the gel was further investigated with regard to *in vitro* activity. The beneficial effects of polyphenols on human skin are largely described, such as antioxidant, anti-aging, anti-inflammatory, wound healing and anti-cancer activities (Badhani et al., 2015; Yang et al., 2016). Particularly, one of the properties of GA is the inhibition of the invasive capacity of melanoma cells (Lin, 2010) and therefore both wound healing and migration assays were performed on HaCaT cells and SK-Mel 28 cells.

i) MTT assay

To determine the effect of gels on cell viability, the cytotoxicity was assessed by MTT assay. P15, P15-GA10 and GA aqueous solution were tested for 24h and the range of GA concentrations nontoxic for both HaCaT and SK-Mel 28 cells was studied. In both cell lines, cytotoxicity of GA occurred in a dose-dependent manner and the blank vehicle did not show cytotoxic effect at all concentrations (data not shown).

Based on the cytotoxicity data, GA 50 μ M and 100 μ M were selected as the highest non-cytotoxic concentrations respectively for HaCaT and SK-Mel 28 cells, for the subsequent assays.

ii) Wound healing assay

To test whether the gel could improve the effect of GA in wound closure, *in vitro* wound healing assay has been performed, and results are depicted in *Figure 53*. Particularly, the wound healing effect on HaCaT cells (*Figure 53 A*) by P15-GA10 clearly prevented the “in vitro” wound closure at both 24 h and 36 h, respect to untreated control cells (CTRL) and cells treated only with the vehicle (gel P15). Of note, no differences between CTRL and cells treated with P15 were observed at the different time-points, confirming the inhibitory activity of GA in wound closure. Similar results have been obtained in the case of SK-Mel 28 cells, (*Figure 53 B*), with an even more evident effect at the later time point (36 h). Despite some authors have demonstrated the capability of GA in accelerating wound closure in human

keratinocytes (Yang et al., 2016), it is possible that the result discrepancy could be due to the different GA doses used, suggesting a dose opposite effect based on its pharmacological concentration. Taking in consideration that cellular migration is a key event in wound healing (especially in the *in vitro* scratch assay) (Grada et al., 2017; Muresan et al., 2018a), we decided to evaluate the ability of GA to prevent cellular migration.

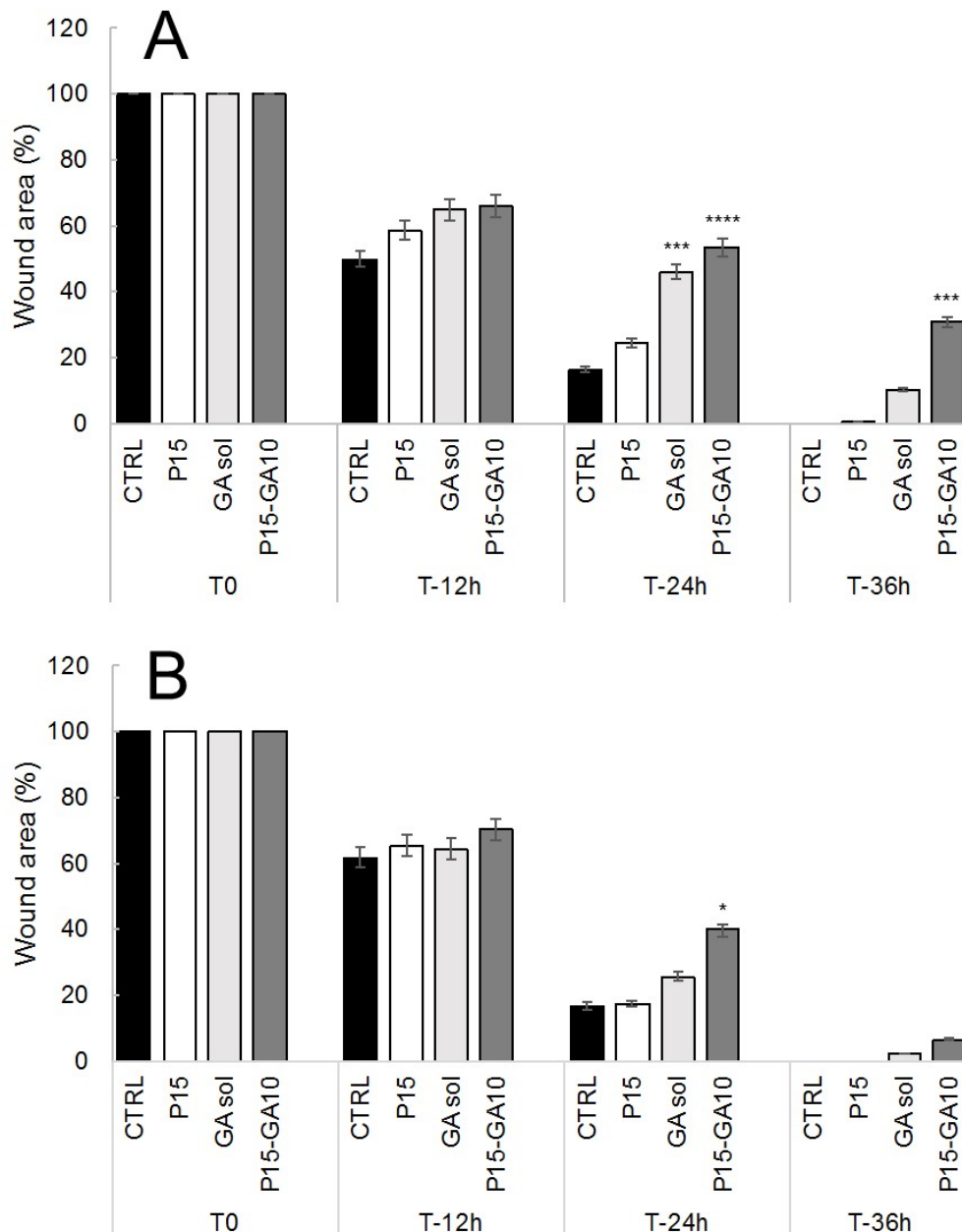


Figure 53: Effect of P15, GA sol and P15-GA10 in counteracting the wound closure in a model based on HaCaT cells (**A**) and SK-Mel 28 cells (**B**). The graph shows the quantitative measurement of wound closure rate in cells treated with the three formulations at different time intervals (0, 12, 24 and 36 h) after the scratch wound. Gap area is expressed as a percentage of the original wound at 0 h for each treatment. Data are means \pm sd of triplicate in three independent experiments (one-way ANOVA, * $p < 0.05$, *** $p < 0.001$, **** $p < 0.0001$ vs CTRL at the same timepoint)

iii) Migration assay

Particularly, the ability of GA solution or P15-GA10 in inhibiting cell migration was evaluated in both HaCaT and SK-Mel 28 cell lines. As shown in *Figure 54*, the ability of GA to reduce cellular migration has been enhanced in the case of P15-GA10. This effect was already noticeable at 6 h and extremely significant for both cell lines (*Figure 54 B*) ($p < 0.0001$), confirming the results obtained with scratch wound assay.

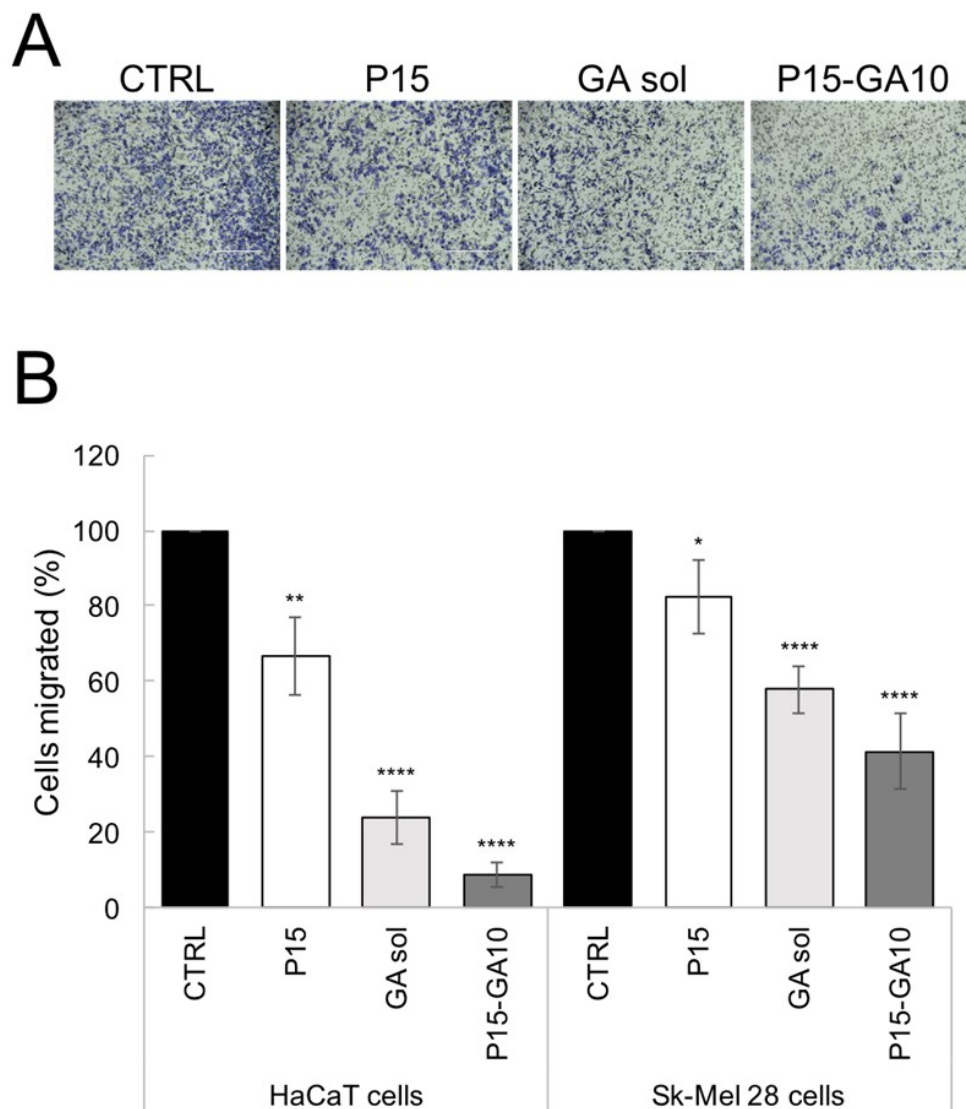


Figure 54: Effect of P15, GA sol and P15-GA10 on cell migration. Representative images of experiments performed on Sk-Mel 28 cells, scale bar 400 μm (**A**). Cells were seeded in 8 μm -pore size transwells and incubated for 6h, then fixed and migrated cells were stained. Quantification of migrated cells after 6 h of treatment for HaCaT and SK-Mel 28 cells (Average of 5 picture fields at 10x total magnification) (**B**). Data are means \pm sd of triplicate in three independent experiments (one-way ANOVA, * $p < 0.05$, ** $p < 0.01$, **** $p < 0.0001$ vs their respective untreated control)

Thanks to the enhanced inhibitory effect of P15-GA10 on SK-Mel 28 cells, the gel could be possibly proposed as adjuvant for the treatment of cutaneous melanoma. Moreover, the suitable application of the gel on the skin represents a promising new technology, not only targeting cancer but also any hyperproliferative disease such as psoriasis.

10. POLOXAMER-HYALURONIC ACID BASED GELS FOR THE DELIVERY OF CAFFEIC ACID

10.1. INTRODUCTION

In the last decades, hydrogels have gained attention thanks to their distinct properties, such as high water content, swellable matrix, biocompatibility and viscoelasticity, which allow their topical application in the treatment of cutaneous and mucosal diseases. Moreover, the crosslink network able to load drugs, providing protection from physical-chemical degradation, makes them suitable for drug delivery field (Chai et al., 2017).

In literature both synthetic and natural polymers have been largely described as promising components for the development of biocompatible hydrogel. Particularly, the association of synthetic polymers, such as Poloxamers, with natural ones, such as hyaluronic acid (HA), can result in a thermosensitive and mucoadhesive formulation for drug delivery (Mayol et al., 2008).

As recently investigated by our group, Poloxamer 407 (poly(oxyethylene)poly(oxypropylene)) (PEO-PPO) block copolymer, is characterized by self-assembly and thermo-reversible properties (Sguizzato et al., 2020). The ability to gel *in situ* when topically applied, make it an attractive carrier for the delivery of different active molecules. However, the poor mechanical character of poloxamer gels need to be optimized by the use of a viscoelastic molecule able to improve the mucoadhesion of the gel maintain its gelation property. At this purpose, HA, a major component of the extra-cellular matrix of the connective tissue, has been studied for its mucoadhesive properties in different applications. Indeed, this natural polysaccharide showed film-forming properties in association to poloxamer gels, without affecting the thermo-reversible and self-assembly characters (Mayol et al., 2008).

In this study, the development of poloxamer-HA based gels has been considered for the delivery of a natural molecule, namely Caffeic acid (CA).

CA is a phenolic compound, cinnamic acid derivative (*Figure 55*) largely distributed in plant tissues and food sources (Magnani et al., 2014).

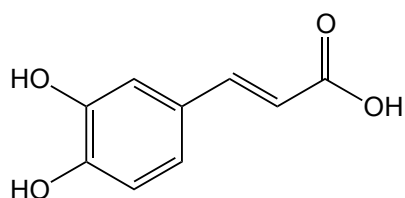


Figure 55: Chemical structure of Caffeic Acid

It is well known that this compound possesses antioxidant, anti-aging, antimicrobial and carcinogenic inhibitor properties. Particularly, it exerts antioxidant activity acting as free radical scavenger in the initiation step as well as in the propagation of the oxidative process. Additionally, its photoprotective property has been demonstrated in UV induced-lipid peroxidation (Saija et al., 1999).

Furthermore, the antiproliferative effect of CA on Sk-Mel 28 cells, a human malignant melanoma cell line, has been studied *in vitro*, showing inhibitory effect on cell proliferation (Pelinson et al., 2019).

The multiple activities of CA make them attractive both in cosmetic and pharmaceutical fields, especially for topical administration.

In order to increase the stability and the activity of CA, its delivery in poloxamer-HA based gels has been investigated. A preformulation study has been conducted, focusing on different production methods. Spreadability, adhesion and rheology tests of the formulated gels have been studied in order to evaluate the influence of the different components in the final characterization. The *in vitro* CA diffusion from the gels was investigated by Franz cells method and the cytotoxicity on human keratinocytes, namely HaCaT cells, was tested.

10.2. RESULTS AND DISCUSSION

10.2.1. Gel preparation and characterization

In view of topical administration of CA, the copolymer Poloxamer 407 was selected to produce a thermoreversible gel able to improve the solubilization of the drug. Based on the preformulation study described in our previous work (Sguizzato et al., 2020), the poloxamer-based gels were prepared at the concentration of 15% (w/w), following the “cold technique” described in the method section. In this study, the addition of a natural polymer, namely HA, in the formulation of the gels was considered, thanks to its viscoelastic and physiological properties (Esposito et al., 2018a).

Table 35 describes the formulations produced for this study.

Firstly, HA4 with different molecular weights, i.e. 50, 300 and 800 kDa, were considered in order to produce several gels with concentration of 4% (w/v). The consistence of HA₅₀, HA₃₀₀ and HA₈₀₀ gels was evaluated with the aim of considering their final addition to poloxamer gel and finally the intermediate HA₃₀₀ was selected. Two different techniques were investigated to incorporate HA in the preformulated P15. The first method is based on the direct addition of HA₃₀₀ in poloxamer gel and the resulting formulation appeared inhomogeneous, characterized by a long solubilization time. The second technique consists in the respective dilution of P30 and HA4, in order to obtain the final concentration of P15-HA2. Despite the additional production of two intermediate gels, this method appeared more efficacy in obtaining a homogeneous formulation.

Table 35: Acronyms and compositions of the produced gels

Acronym	Composition %			
	poloxamer 407 (w/w)	water (w/w)	hyaluronic acid (w/v)	caffeic acid (w/v)
P15	15.0	85.0	-	-
P15-HA2	15.0	85.0	2	-
P30	30.0	70.0	-	-
HA4	-	-	4	-
P15-CA	15.0	85.0	-	0.1
P15-HA2-CA	15.0	85.0	2	0.1

The ability of P15 and P15-HA to solubilize CA was evaluated under visual inspection, gradually increasing the CA concentration. After direct addition of CA, the presence of drug precipitates or suspended powder crystals was observed comparing the products with CA aqueous solution. The final solubility concentration in water was 0.5 mg/ml, while in the case of P15 and P15-HA2, the gels enabled to increase the concentration up to 1 mg/ml. Thus, P15 and P15-CA appeared homogeneously transparent, while P15-HA2 and P15-HA2-CA appeared slightly opalescent for the presence of HA. Moreover, these concentrations were selected for further experiments.

10.2.2. Rheological study

In order to predict the behavior of P15-CA and P15-HA2-CA during storage and after administration onto the skin, rheological studies have been conducted.

Particularly the viscoelastic behavior of the gels, described by measuring elastic G' and viscous G'' moduli, have been evaluated. As reported in our previous work (Sguizzato et al., 2020), the elastic modulus indicates the solid-like component of elastic behavior, reflecting the stored elastic energy, while the viscous modulus reflects the dissipated loss of energy. *Figure 56* shows the elastic modulus G' and the viscous modulus G'' as a function of temperature for P15-CA (A) and P15-HA2-CA (B).

In the case of P15-CA (*Figure 56 A*), G' and G'' profiles are almost overlapped in the first phase, while in the case of P15-HA2-CA (*Figure 56 B*) G' profile is lower than G'' . At a well-defined temperature ($T_{\text{sol-gel}}$) a sudden increase of the moduli was observed in both cases, with G' becoming higher than G'' , indicating a transition from liquid (sol) to structured (gel) behavior. The transition temperature $T_{\text{sol-gel}}$ of P15-CA was 28.6°C (Sguizzato et al., 2020), while that of P15-HA2-CA was 24.7°C. Thus, the presence of HA in the formulation leads to a decreased $T_{\text{sol-gel}}$, resulting in a stiffer gel. Above the gelation temperature G' was significantly higher than G'' , indicating an ordered packing of the micelles, mostly in the case of P15-HA2-CA. This behavior suggests that both gels were almost purely elastic, being the typical performance of solid-like structures (Koffi et al., 2006).

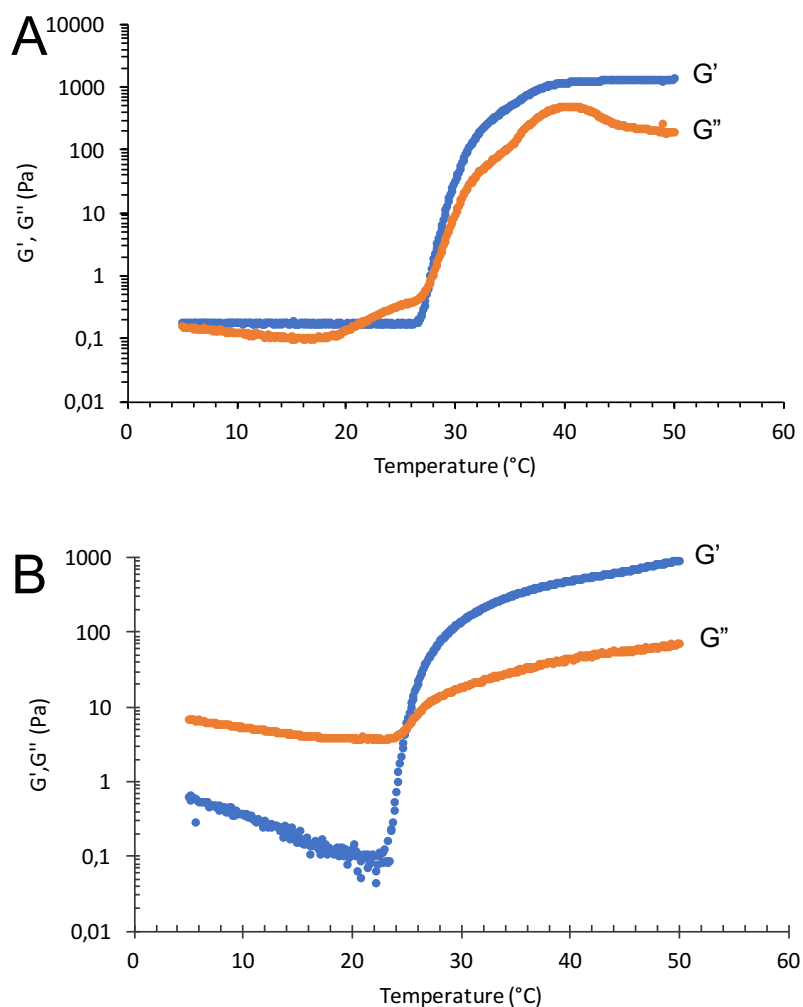


Figure 56: Effect of the temperature on elastic (G') and viscous (G'') moduli for P15-CA (**A**) and P15-HA2-CA (**B**)

Comparing the results with those obtained with empty P15 and P15-HA2 gels (data not shown), the presence of CA in both formulations did not change the viscoelastic properties of the gels, indicating no interactions with the drug.

10.2.3. Spreadability study

The spreadability of gels is an important parameter, being involved in different processes during application on skin, such as extrudability from the package, covering of skin area, patient compliance and drug therapeutic efficacy. In order to mimic the skin temperature, this parameter has been evaluated at 33°C comparing the different gels.

Table 36 describes the spreadability values of P15-CA and P15-HA2-CA.

Table 36: Spreadability of the produced gels

Acronym	Spreadability (g x cm / sec)
P15-CA	8.24 ± 2.01
P15-HA2-CA	5.02 ± 0.39

The reported results are the average of four independent experiments ± sd

As expected, the lower the stiffness, the higher the spreadability, indeed spreadability value of P15-CA was about 1.5-fold higher than P15-HA2-CA (Sguizzato et al., 2020). This result confirms the rheological data, indicating that HA influences the spreadability of the gel.

10.2.4. Skin Adhesion study

In order to gain information on the gel adhesion after administration on skin, P15-CA and P15-HA2-CA were applied on the ventral surface forearm of a volunteer and their residence times were compared.

As shown in *Figure 57*, the *in vivo* evaluation evidenced a higher residence time for P15-HA2-CA, indicating the ability of HA to obtain an in-situ formulation. Indeed, after 10 seconds, P15-CA slides along the forearm.

Furthermore, the presence of both gels on skin surface upon time demonstrates the suitability of the poloxamer gels for skin application.



Figure 57: Adhesion of P15-CA (A) and P15-HA2-CA (B) on the ventral surface of a volunteer forearm

10.2.5. $!(\%)*+,-$ CA diffusion kinetics

In order to investigate the efficacy of P15 and P15-HA2 in controlling the release of CA, the *in vitro* CA diffusion was studied by Franz cells experiment. The nylon membrane was exploited as synthetic membrane able to reproduce the diffusion of the drug after topical application.

The concentration of CA diffused in time was quantified by HPLC and the diffusion profiles are displayed in *Figure 58*.

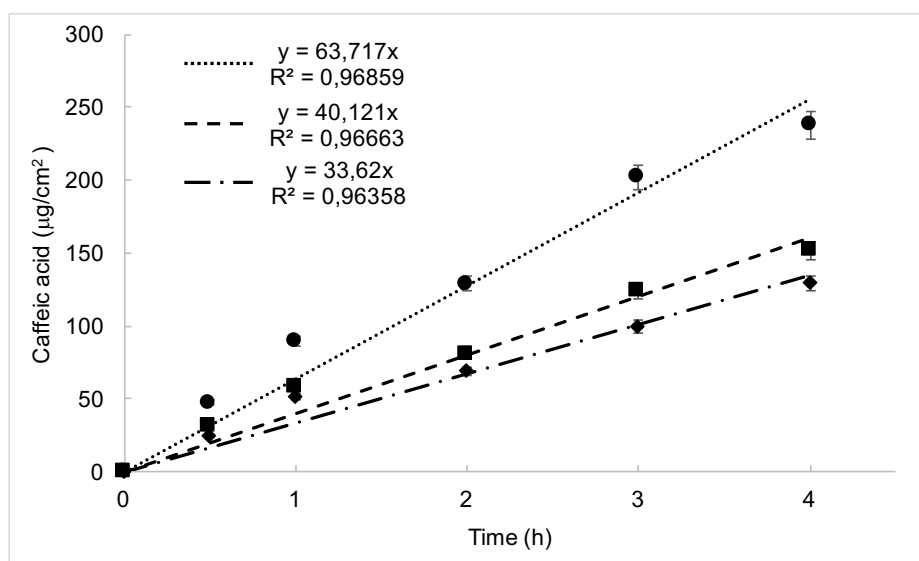


Figure 58: Franz cells diffusion profiles of GA from P15-CA (diamond), P15-HA2-CA (square) and CA aqueous solution (circle). Data represent the mean of six independent experiments \pm sd

As expected, CA diffusion was faster from the aqueous solution than from P15-CA and P15-HA2-CA, indicating a controlled release of CA by the gels. Despite the rheological results, P15-HA2-CA showed a faster diffusion rate compared to P15-CA. It can be assumed that at the body temperature the organization of the packed micellar system of poloxamer is modified by the presence of HA. Indeed, the intramolecular H bonds of HA could be disrupted by temperature, resulting in a more flexible conformation (Ström et al., 2015). Thus, the CA diffusion rate resulted accelerated.

Furthermore, it should be noticed that the CA concentration employed in the different vehicles corresponded to the highest solubility concentration, thus 0.5 mg/ml in the aqueous solution and 1 mg/ml in the gels. Consequently, the diffusion coefficients and the flux values reported in *Table 37* have been calculated considering the real concentrations employed in the assay.

Table 37: CA diffusion data from the gels and the aqueous solution obtained by Franz cells

Formulation	F ^a	D ^b
P15-CA	33.62 ± 3.0	33.62 ± 3.0
P15-HA2-CA	40.12 ± 4.5	40.12 ± 4.5
CA sol	63.72 ± 5.7	127.44 ± 5.7

The reported results are the average of four independent experiments ± sd

a: flux (slope of the lines); b: diffusion coefficients

Comparing the diffusion coefficients reported in *Table 37*, the diffusion rate of CA from the aqueous solution was respectively 3.79-fold and 3.17-fold higher from P15-CA and from P15-HA2-CA. As expected, viscous forms better control CA diffusion, suggesting the suitability of the poloxamer-based gels as topical “smart” formulations with controlled release properties.

10.2.6. Cytotoxicity study

Considering the topical administration of the formulated gels, their cytotoxicity was evaluated on HaCaT cells by MTT assay. The viability of cells was assessed 24 h after treatment with the formulations at different concentrations.

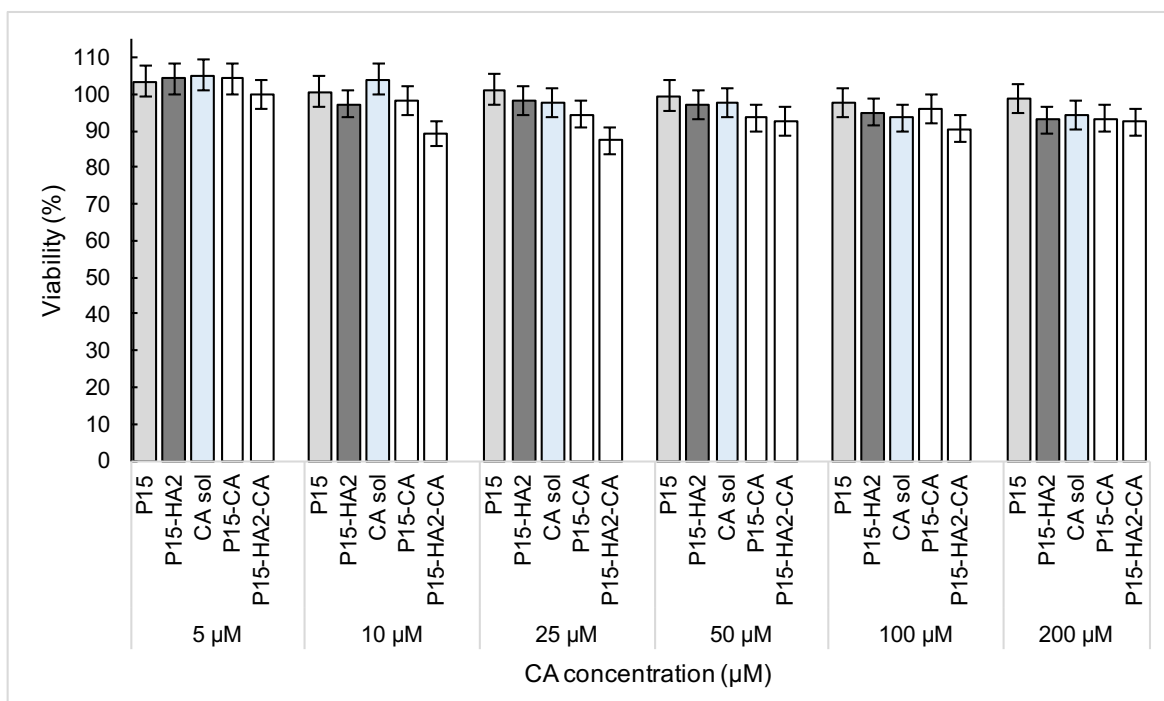


Figure 59: Cytotoxicity of P15 (light grey), P15-HA2 (dark grey), CA aqueous solution (light blue), P15-CA (light grey square) and P15-HA2-CA (dark grey square) evaluated by MTT test on HaCaT cells after 24h of treatment. Data are given as mean ± sd, representative of three independent experiments with at least three technical replicates each time

As shown in *Figure 59*, all the formulations resulted not cytotoxic up to the highest concentration of CA. The viability was higher than 87% in all treatments and no significant differences were detected between the different vehicles. These results confirm the biocompatibility of the polymers used in the gels, namely synthetic as poloxamer and natural as HA.

Based on these data, the highest concentration can be selected for further experiments in order to evaluate the antioxidant activity of CA as well as the improved efficacy of the drug when delivered by the gels.

11. CONCLUSIONS

Considering the results obtained in this work, the conclusions reported in the following paragraphs can be drawn.

The study reported in chapter 4 describes the design and characterization of a liposphere gel containing CLO for the treatment of *Candida albicans*.

The results evidenced that the presence of AL in the LS composition enables to solubilize and encapsulate higher amount of CLO with respect to the use of a single component in the formulation. Furthermore, the anticandidal activity of the drug was supported by the effects of AL in controlling bacterial proliferation, in re-establishing the pH of the vaginal environment and modulating LS metabolism.

The inclusion of LS in the gel led to a minimal leakage, a long adhesion time and a slower release of drug, demonstrating the suitability of Gel LS_{TRIST/AL1}-CLO for vaginal application. Remarkably, Gel LS_{TRIST/AL1}-CLO production can be easily scaled-up for industrial production.

However, *in vivo* experiments are required to confirm the possible treatment of vaginal candidiasis.

The investigation described in the chapter 5, focuses on a scaling up study aimed at producing PRG containing nanoparticles in a pilot scale.

The results indicate that both SLN-PRG and NLC-PRG produced by HPH were characterized by a good physical and chemical stability and smaller mean diameters of particles with respect to UH method. They appeared homogeneous and without agglomeration phenomena up to 6 months from the production. Both SLN and NLC displayed high encapsulation efficiency for PRG with double fold stability of the drug, controlling its release and skin uptake.

Tape stripping experiments indicated that PRG formulated in SLN/G and NLC/G represent suitable formulations to facilitate and control the skin uptake of the drug. Nevertheless, further *in vivo* studies are required to better understand the kinetics of PRG distribution in the different skin layers, as well as to evaluate in deeper detail the effect of formulation constituents (i.e. thickening agents and nanoparticle components) on the *in vivo* performances of lipid nanoparticles.

The study described in chapter 6, suggests that a nanoparticle based hyaluronate gel containing RP can be efficiently employed for wound healing.

The choice of lipid nanoparticles has been effective in encapsulating two substances with different physico-chemical properties in the same vehicle. Indeed, RP was solubilized in the lipid dispersed phase, while HA in the aqueous dispersing phase.

NLC enabled to encapsulate higher amount of RP with respect to SLN, showing great stability over time. The viscosization of NLC by dispersing HA conferred “pseudo-plastic” properties to the vehicle, allowing to better control cutaneous administration on wounds and RP diffusion.

The promising findings obtained on a 2D *in vitro* model of wound healing create a solid basis for future studies in more complex and realistic skin models such as 3D skin equivalents or animals to generate novel approaches for wound healing complications.

The work reported in chapter 7, underlines the importance of technological screening in the design of a nanoparticulate lipid dosage formulation.

Notably, dimensional and morphological characterization of nanoparticles should be performed after different lengths of time from production. Actually, this investigation has demonstrated that type and concentration of lipid phase affect physico-chemical stability of nanoparticles.

NLC T10-TOC selected by the pre-formulation study deserved further *in vitro* and *in vivo* studies. Indeed supplementary studies will be performed to investigate the activity of hydrophilic antioxidant molecules, loaded in NLC and in comparison with conventional “non-nano” formulation. In addition, since some authors have demonstrated that CS induces depletion of some essential vitamins, such as TOC, it should be interesting to evaluate the suitability of NLC T10-TOC as oral antioxidant supplement.

In chapter 8, two different lipid based nanocarriers were developed with the aim of enhancing the effect of Ub-O in protecting cells against oxidative stress.

The characterization of NLC and ETHO in terms of size, morphology and encapsulation efficiency allowed to select the second formulation as the optimal delivery system for Ub-O. The high stability of the encapsulated drug demonstrated the effect of ETHO in protecting sensitive molecule from degradation, thanks to the avoidance of thermal and mechanical insults.

Moreover, the flexibility of this novel lipid-based delivery system facilitated the interaction with cellular membrane, allowing extracellular Ub-O to counteract OS. The results revealed a promising strategy in prevent cellular OS status, combining the antioxidant activity of Ub-O and the drug-targeting property of ETHO. Further studies should be conducted on RTT fibroblasts in order to evaluate the antioxidant effect of Ub-O in unhealthy cells. Additionally, the design of Ub-R-containing ETHO should be considered to compare the activity of the drug in the different oxidation states.

In chapter 9, the production and characterization of poloxamer gels containing GA are described, in order to obtain a formulation suitable for topical application to treat melanoma.

The rheological and spreadability characterization enabled to select P15-GA10 gel as a smart vehicle for GA application on the skin, enhancing drug solubility and stability over time.

Franz cell studies revealed that drugs solubilized in viscous formulations could display unexpected diffusion profiles with respect to aqueous solutions, decidedly influenced by the employed membrane. Indeed, the GA diffusion discrepancies have evidenced the importance of the membrane choice. Many types of commercial membranes are available on the market, displaying different diffusion properties for any drug. Besides physicochemical properties and pore size of the membranes, also solvents and composition of the donor and receptor compartment can affect drug diffusion. Thus, despite single synthetic membranes can be suitable for quality control studies, any new topical formulation should require a preliminary screening aimed at selecting a synthetic membrane system for mimicking *in vivo* diffusion.

The encouraging biological results here presented suggest the possibility to employ P15-GA10 gel in the treatment of cutaneous diseases, such as melanoma, as well as any hyperproliferative disease, such as psoriasis. Nevertheless, *in vivo* studies are required to confirm these preliminary data.

The preliminary study reported in chapter 10 describes the combination of two different polymers, namely poloxamer and HA, in the development of a thermosensitive and mucoadhesive gel for the delivery of CA.

The achievement of an in-situ formulation preserving the smart properties of poloxamer gel, obtained by the addition of HA, allowed to ensure a long residence time and a controlled release of solubilized CA. On one hand, the rheological and

spreadability investigations demonstrated the suitability of the formulated gels in view of application on the skin. On the other one, the ability of gels to better control CA diffusion was confirmed by *in vitro* studies with Franz cells experiment.

Further studies concerning the internal structure of the gel network should elucidate the interaction between poloxamer and HA. Furthermore, since the formulations did not show cytotoxicity on human keratinocytes, the *in vitro* antioxidant activity of delivered CA should be evaluated in order to consider the topical administration of this natural molecule, both in pharmaceutical or cosmetical application.

At the end of this thesis it has to be underlined the importance of a technological screening in the design of novel delivery nanosystems. The study of the structure and the behavior of the selected components as well as their interaction with the interested molecules allowed to develop different carrier systems by the employment of innovative techniques. The effectively tolerability of the described drug delivery systems after application onto skin makes them suitable for both pharmaceutical and cosmetic fields.

12. BIBLIOGRAPHY

- Abraham, N.G., Kappas, A., 2008. Pharmacological and Clinical Aspects of Heme Oxygenase. *Pharmacol Rev* 60, 79–127. <https://doi.org/10.1124/pr.107.07104>
- Aka-Any-Grah, A., Bouchemal, K., Koffi, A., Agnely, F., Zhang, M., Djabourov, M., Ponchel, G., 2010. Formulation of mucoadhesive vaginal hydrogels insensitive to dilution with vaginal fluids. *European Journal of Pharmaceutics and Biopharmaceutics* 76, 296–303. <https://doi.org/10.1016/j.ejpb.2010.07.004>
- Akbarzadeh, A., Rezaei-Sadabady, R., Davaran, S., Joo, S.W., Zarghami, N., Hanifehpour, Y., Samiei, M., Kouhi, M., Nejati-Koshki, K., 2013. Liposome: classification, preparation, and applications. *Nanoscale Res Lett* 8, 102. <https://doi.org/10.1186/1556-276X-8-102>
- Alam, T., Pandit, J., Vohora, D., Aqil, M., Ali, A., Sultana, Y., 2015. Optimization of nanostructured lipid carriers of lamotrigine for brain delivery: in vitro characterization and in vivo efficacy in epilepsy. *Expert Opin Drug Deliv* 12, 181–194. <https://doi.org/10.1517/17425247.2014.945416>
- Alexander, A., Dwivedi, S., Ajazuddin, Giri, T.K., Saraf, Swarnlata, Saraf, Shailendra, Tripathi, D.K., 2012. Approaches for breaking the barriers of drug permeation through transdermal drug delivery. *Journal of Controlled Release* 164, 26–40. <https://doi.org/10.1016/j.jconrel.2012.09.017>
- Andrade, A.O., Parente, M.E., Ares, G., 2014. Screening of mucoadhesive vaginal gel formulations. *Braz. J. Pharm. Sci.* 50, 931–941. <https://doi.org/10.1590/S1984-82502014000400029>
- Andrade, L.M., de Fátima Reis, C., Maione-Silva, L., Anjos, J.L.V., Alonso, A., Serpa, R.C., Marreto, R.N., Lima, E.M., Taveira, S.F., 2014. Impact of lipid dynamic behavior on physical stability, in vitro release and skin permeation of genistein-loaded lipid nanoparticles. *European Journal of Pharmaceutics and Biopharmaceutics* 88, 40–47. <https://doi.org/10.1016/j.ejpb.2014.04.015>
- Anirudhan, T.S., Nair, S.S., Nair, A.S., 2016. Fabrication of a bioadhesive transdermal device from chitosan and hyaluronic acid for the controlled release of lidocaine. *Carbohydrate Polymers* 152, 687–698. <https://doi.org/10.1016/j.carbpol.2016.06.101>
- Atzori, L., Caramori, G., Lim, S., Jazrawi, E., Donnelly, L., Adcock, I., Barnes, P.J., Chung, K.F., 2004. Effect of cigarette smoking on haem-oxygenase expression in alveolar macrophages. *Respiratory Medicine* 98, 530–535. <https://doi.org/10.1016/j.rmed.2003.11.007>
- Aulton, M.E., Taylor, K. (Eds.), 2018. *Aulton's pharmaceutics: the design and manufacture of medicines*, Fifth edition. ed. Elsevier, Edinburgh ; New York.
- Badhani, B., Sharma, N., Kakkar, R., 2015. Gallic acid: a versatile antioxidant with promising therapeutic and industrial applications. *RSC Adv.* 5, 27540–27557. <https://doi.org/10.1039/C5RA01911G>
- Baloglu, E., Karavana, S.Y., Senyigit, Z.A., Guneri, T., 2011. Rheological and mechanical properties of poloxamer mixtures as a mucoadhesive gel base. *Pharmaceutical Development and Technology* 16, 627–636. <https://doi.org/10.3109/10837450.2010.508074>

- Bartosova, L., Bajgar, J., 2012. Transdermal drug delivery in vitro using diffusion cells. *Curr. Med. Chem.* 19, 4671–4677. <https://doi.org/10.2174/092986712803306358>
- Battaglia, L., Gallarate, M., 2012. Lipid nanoparticles: state of the art, new preparation methods and challenges in drug delivery. *Expert Opinion on Drug Delivery* 9, 497–508. <https://doi.org/10.1517/17425247.2012.673278>
- Benowitz, N.L., Hukkanen, J., Jacob, P., 2009. Nicotine Chemistry, Metabolism, Kinetics and Biomarkers, in: Henningfield, J.E., London, E.D., Pogun, S. (Eds.), *Nicotine Psychopharmacology*. Springer Berlin Heidelberg, Berlin, Heidelberg, pp. 29–60. https://doi.org/10.1007/978-3-540-69248-5_2
- Berriaud, N., Milas, M., Rinaudo, M., 1994. Rheological study on mixtures of different molecular weight hyaluronates. *Int. J. Biol. Macromol.* 16, 137–142. [https://doi.org/10.1016/0141-8130\(94\)90040-x](https://doi.org/10.1016/0141-8130(94)90040-x)
- Bhaskar, K., Mohan, C.K., Lingam, M., Mohan, S.J., Venkateswarlu, V., Rao, Y.M., Bhaskar, K., Anbu, J., Ravichandran, V., 2009. Development of SLN and NLC Enriched Hydrogels for Transdermal Delivery of Nitrendipine: In Vitro and In Vivo Characteristics. *Drug Development and Industrial Pharmacy* 35, 98–113. <https://doi.org/10.1080/03639040802192822>
- Bishop, A., 2008. Role of oxygen in wound healing. *J Wound Care* 17, 399–402. <https://doi.org/10.12968/jowc.2008.17.9.30937>
- Boddupalli, B., Mohammed, ZulkarN.K., Nath, R., Banji, D., 2010. Mucoadhesive drug delivery system: An overview. *J Adv Pharm Tech Res* 1, 381. <https://doi.org/10.4103/0110-5558.76436>
- Bodratti, A., Alexandridis, P., 2018. Formulation of Poloxamers for Drug Delivery. *JFB* 9, 11. <https://doi.org/10.3390/jfb9010011>
- Bouwstra, J.A., Ponec, M., 2006. The skin barrier in healthy and diseased state. *Biochim. Biophys. Acta* 1758, 2080–2095. <https://doi.org/10.1016/j.bbamem.2006.06.021>
- Brown, M.B., Jones, S.A., 2005. Hyaluronic acid: a unique topical vehicle for the localized delivery of drugs to the skin. *J Eur Acad Dermatol Venereol* 19, 308–318. <https://doi.org/10.1111/j.1468-3083.2004.01180.x>
- Bruno, R.S., Traber, M.G., 2005. Cigarette Smoke Alters Human Vitamin E Requirements. *The Journal of Nutrition* 135, 671–674. <https://doi.org/10.1093/jn/135.4.671>
- Buettner, G.R., 1993. The Pecking Order of Free Radicals and Antioxidants: Lipid Peroxidation, α -Tocopherol, and Ascorbate. *Archives of Biochemistry and Biophysics* 300, 535–543. <https://doi.org/10.1006/abbi.1993.1074>
- Burry, K.A., Patton, P.E., Hermsmeyer, K., 1999. Percutaneous absorption of progesterone in postmenopausal women treated with transdermal estrogen. *American Journal of Obstetrics and Gynecology* 180, 1504–1511. [https://doi.org/10.1016/S0002-9378\(99\)70046-3](https://doi.org/10.1016/S0002-9378(99)70046-3)
- Canella, R., Benedusi, M., Martini, M., Cervellati, F., Cavicchio, C., Valacchi, G., 2018. Role of Nrf2 in preventing oxidative stress induced chloride current alteration in human lung cells. *J Cell Physiol* 233, 6018–6027. <https://doi.org/10.1002/jcp.26416>
- Carter, P., Narasimhan, B., Wang, Q., 2019. Biocompatible nanoparticles and vesicular systems in transdermal drug delivery for various skin diseases. *International Journal of Pharmaceutics* 555, 49–62. <https://doi.org/10.1016/j.ijpharm.2018.11.032>
- Castro, G.A., Oréfice, R.L., Vilela, J.M.C., Andrade, M.S., Ferreira, L.A.M., 2007.

Development of a new solid lipid nanoparticle formulation containing retinoic acid for topical treatment of acne. *Journal of Microencapsulation* 24, 395–407. <https://doi.org/10.1080/02652040701288519>

Castro, J.P., Jung, T., Grune, T., Siems, W., 2017. 4-Hydroxynonenal (HNE) modified proteins in metabolic diseases. *Free Radical Biology and Medicine* 111, 309–315. <https://doi.org/10.1016/j.freeradbiomed.2016.10.497>

Cervellati, C., Sticozzi, C., Romani, A., Belmonte, G., De Rasmio, D., Signorile, A., Cervellati, F., Milanese, C., Mastroberardino, P.G., Pecorelli, A., Savelli, V., Forman, H.J., Hayek, J., Valacchi, G., 2015. Impaired enzymatic defensive activity, mitochondrial dysfunction and proteasome activation are involved in RTT cell oxidative damage. *Biochimica et Biophysica Acta (BBA) - Molecular Basis of Disease* 1852, 2066–2074. <https://doi.org/10.1016/j.bbadis.2015.07.014>

Chai, Q., Jiao, Y., Yu, X., 2017. Hydrogels for Biomedical Applications: Their Characteristics and the Mechanisms behind Them. *Gels* 3, 6. <https://doi.org/10.3390/gels3010006>

Chen, J., Wei, N., Lopez-Garcia, M., Ambrose, D., Lee, J., Annelin, C., Peterson, T., 2017. Development and evaluation of resveratrol, Vitamin E, and epigallocatechin gallate loaded lipid nanoparticles for skin care applications. *European Journal of Pharmaceutics and Biopharmaceutics* 117, 286–291. <https://doi.org/10.1016/j.ejpb.2017.04.008>

Chen, W.Y., Abatangelo, G., 1999. Functions of hyaluronan in wound repair. *Wound Repair Regen* 7, 79–89. <https://doi.org/10.1046/j.1524-475x.1999.00079.x>

Chuang, S.-Y., Lin, C.-H., Huang, T.-H., Fang, J.-Y., 2018. Lipid-Based Nanoparticles as a Potential Delivery Approach in the Treatment of Rheumatoid Arthritis. *Nanomaterials* 8, 42. <https://doi.org/10.3390/nano8010042>

Clément, P., Laugel, C., Marty, J.-P., 2000. Influence of three synthetic membranes on the release of caffeine from concentrated W/O emulsions. *Journal of Controlled Release* 66, 243–254. [https://doi.org/10.1016/S0168-3659\(99\)00276-X](https://doi.org/10.1016/S0168-3659(99)00276-X)

Cortesi, R., Esposito, E., Luca, G., Nastruzzi, C., 2002. Production of lipospheres as carriers for bioactive compounds. *Biomaterials* 23, 2283–2294. [https://doi.org/10.1016/S0142-9612\(01\)00362-3](https://doi.org/10.1016/S0142-9612(01)00362-3)

D'Agostino, A., Stellavato, A., Busico, T., Papa, A., Tirino, V., Papaccio, G., La Gatta, A., De Rosa, M., Schiraldi, C., 2015. In vitro analysis of the effects on wound healing of high- and low-molecular weight chains of hyaluronan and their hybrid H-HA/L-HA complexes. *BMC Cell Biol.* 16, 19. <https://doi.org/10.1186/s12860-015-0064-6>

das Neves, J., Bahia, M.F., 2006. Gels as vaginal drug delivery systems. *International Journal of Pharmaceutics* 318, 1–14. <https://doi.org/10.1016/j.ijpharm.2006.03.012>

Das, S., Chaudhury, A., 2011. Recent Advances in Lipid Nanoparticle Formulations with Solid Matrix for Oral Drug Delivery. *AAPS PharmSciTech* 12, 62–76. <https://doi.org/10.1208/s12249-010-9563-0>

De Felice, C., Ciccoli, L., Leoncini, S., Signorini, C., Rossi, M., Vannuccini, L., Guazzi, G., Latini, G., Comporti, M., Valacchi, G., Hayek, J., 2009. Systemic oxidative stress in classic Rett syndrome. *Free Radical Biology and Medicine* 47, 440–448. <https://doi.org/10.1016/j.freeradbiomed.2009.05.016>

Dietrich, M., Block, G., Norkus, E.P., Hudes, M., Traber, M.G., Cross, C.E., Packer, L., 2003. Smoking and exposure to environmental tobacco smoke decrease some plasma antioxidants and increase γ -tocopherol in vivo after adjustment for dietary antioxidant intakes. *The American Journal of Clinical Nutrition* 77, 160–166. <https://doi.org/10.1093/ajcn/77.1.160>

- Dingler, A., Gohla, S., 2002. Production of solid lipid nanoparticles (SLN): scaling up feasibilities. *J Microencapsul* 19, 11–16. <https://doi.org/10.1080/02652040010018056>
- Dumortier, G., Grossiord, J.L., Agnely, F., Chaumeil, J.C., 2006. A Review of Poloxamer 407 Pharmaceutical and Pharmacological Characteristics. *Pharm Res* 23, 2709–2728. <https://doi.org/10.1007/s11095-006-9104-4>
- Eiras, F., Amaral, M.H., Silva, R., Martins, E., Lobo, J.M.S., Silva, A.C., 2017. Characterization and biocompatibility evaluation of cutaneous formulations containing lipid nanoparticles. *International Journal of Pharmaceutics* 519, 373–380. <https://doi.org/10.1016/j.ijpharm.2017.01.045>
- Elsner, P., 2011. Anatomical and Physiological Basis of Topical Therapy of the Mucosa, in: Surber, C., Elsner, P., Farage, M.A. (Eds.), *Current Problems in Dermatology*. KARGER, Basel, pp. 1–8. <https://doi.org/10.1159/000321038>
- Esposito, E., Boschi, A., Ravani, L., Cortesi, R., Drechsler, M., Mariani, P., Moscatelli, S., Contado, C., Di Domenico, G., Nastruzzi, C., Giganti, M., Uccelli, L., 2015a. Biodistribution of nanostructured lipid carriers: A tomographic study. *European Journal of Pharmaceutics and Biopharmaceutics* 89, 145–156. <https://doi.org/10.1016/j.ejpb.2014.12.006>
- Esposito, E., Carotta, V., Scabbia, A., Trombelli, L., D'Antona, P., Menegatti, E., Nastruzzi, C., 1996. Comparative analysis of tetracycline-containing dental gels: Poloxamer- and monoglyceride-based formulations. *International Journal of Pharmaceutics* 142, 9–23. [https://doi.org/10.1016/0378-5173\(96\)04649-2](https://doi.org/10.1016/0378-5173(96)04649-2)
- Esposito, E., Cortesi, R., Drechsler, M., Fan, J., Fu, B.M., Calderan, L., Mannucci, S., Boschi, F., Nastruzzi, C., 2017a. Nanoformulations for dimethyl fumarate: Physicochemical characterization and in vitro / in vivo behavior. *European Journal of Pharmaceutics and Biopharmaceutics* 115, 285–296. <https://doi.org/10.1016/j.ejpb.2017.04.011>
- Esposito, E., Drechsler, M., Cortesi, R., Nastruzzi, C., 2016a. Encapsulation of cannabinoid drugs in nanostructured lipid carriers. *European Journal of Pharmaceutics and Biopharmaceutics* 102, 87–91. <https://doi.org/10.1016/j.ejpb.2016.03.005>
- Esposito, E., Drechsler, M., Huang, N., Pavoni, G., Cortesi, R., Santonocito, D., Puglia, C., 2016b. Ethosomes and organogels for cutaneous administration of crocin. *Biomed Microdevices* 18, 108. <https://doi.org/10.1007/s10544-016-0134-3>
- Esposito, E., Drechsler, M., Mariani, P., Carducci, F., Servadio, M., Melancia, F., Ratano, P., Campolongo, P., Trezza, V., Cortesi, R., Nastruzzi, C., 2017b. Lipid nanoparticles for administration of poorly water soluble neuroactive drugs. *Biomed Microdevices* 19, 44. <https://doi.org/10.1007/s10544-017-0188-x>
- Esposito, E., Drechsler, M., Mariani, P., Panico, A.M., Cardile, V., Crascì, L., Carducci, F., Graziano, A.C.E., Cortesi, R., Puglia, C., 2017c. Nanostructured lipid dispersions for topical administration of crocin, a potent antioxidant from saffron (*Crocus sativus* L.). *Materials Science and Engineering: C* 71, 669–677. <https://doi.org/10.1016/j.msec.2016.10.045>
- Esposito, E., Fantin, M., Marti, M., Drechsler, M., Paccamiccio, L., Mariani, P., Sivieri, E., Lain, F., Menegatti, E., Morari, M., Cortesi, R., 2008. Solid Lipid Nanoparticles as Delivery Systems for Bromocriptine. *Pharm Res* 25, 1521–1530. <https://doi.org/10.1007/s11095-007-9514-y>
- Esposito, E., Mariani, P., Drechsler, M., Cortesi, R., 2016c. Structural Studies of Lipid-Based Nanosystems for Drug Delivery: X-ray Diffraction (XRD) and Cryogenic Transmission Electron Microscopy (Cryo-TEM), in: Aliofkhaezraei, M. (Ed.), *Handbook of Nanoparticles*. Springer International Publishing, Cham, pp. 861–889. https://doi.org/10.1007/978-3-319-15338-4_39

Esposito, E., Menegatti, E., Cortesi, R., 2004. Ethosomes and liposomes as topical vehicles for azelaic acid: a preformulation study. *International Journal of Cosmetic Science* 26, 270–271. https://doi.org/10.1111/j.1467-2494.2004.00233_2.x

Esposito, E., Nastruzzi, C., Sguizzato, M., Cortesi, R., 2019. Nanomedicines to Treat Skin Pathologies with Natural Molecules. *CPD* 25, 2323–2337. <https://doi.org/10.2174/1381612825666190709210703>

Esposito, E., Pecorelli, A., Sguizzato, M., Drechsler, M., Mariani, P., Carducci, F., Cervellati, F., Nastruzzi, C., Cortesi, R., Valacchi, G., 2018a. Production and Characterization of Nanoparticle Based Hyaluronate Gel Containing Retinyl Palmitate for Wound Healing. *CDD* 15, 1172–1182. <https://doi.org/10.2174/1567201815666180518123926>

Esposito, E., Ravani, L., Contado, C., Costenaro, A., Drechsler, M., Rossi, D., Menegatti, E., Grandini, A., Cortesi, R., 2013. Clotrimazole nanoparticle gel for mucosal administration. *Materials Science and Engineering: C* 33, 411–418. <https://doi.org/10.1016/j.msec.2012.09.007>

Esposito, E., Ravani, L., Mariani, P., Huang, N., Boldrini, P., Drechsler, M., Valacchi, G., Cortesi, R., Puglia, C., 2014. Effect of nanostructured lipid vehicles on percutaneous absorption of curcumin. *European Journal of Pharmaceutics and Biopharmaceutics* 86, 121–132. <https://doi.org/10.1016/j.ejpb.2013.12.011>

Esposito, E., Sguizzato, M., Bories, C., Nastruzzi, C., Cortesi, R., 2018b. Production and Characterization of a Clotrimazole Liposphere Gel for Candidiasis Treatment. *Polymers* 10, 160. <https://doi.org/10.3390/polym10020160>

Esposito, E., Sguizzato, M., Drechsler, M., Mariani, P., Carducci, F., Nastruzzi, C., Cortesi, R., 2017d. Progesterone lipid nanoparticles: Scaling up and in vivo human study. *European Journal of Pharmaceutics and Biopharmaceutics* 119, 437–446. <https://doi.org/10.1016/j.ejpb.2017.07.015>

Esposito, E., Sticozzi, C., Ravani, L., Drechsler, M., Muresan, X.M., Cervellati, F., Cortesi, R., Valacchi, G., 2015b. Effect of new curcumin-containing nanostructured lipid dispersions on human keratinocytes proliferative responses. *Exp. Dermatol.* 24, 449–454. <https://doi.org/10.1111/exd.12696>

Fakhari, A., Berkland, C., 2013. Applications and emerging trends of hyaluronic acid in tissue engineering, as a dermal filler and in osteoarthritis treatment. *Acta Biomater* 9, 7081–7092. <https://doi.org/10.1016/j.actbio.2013.03.005>

FDA Guidance for Industry: SUPAC-SS: Nonsterile Semisolid Dosage Forms; Scale-Up and Post-Approval Changes: Chemistry, Manufacturing and Controls; In-Vitro Release Testing and In Vivo Bioequivalence Documentation - ECA Academy [WWW Document], n.d. URL <https://www.gmp-compliance.org/guidelines/gmp-guideline/fda-guidance-for-industry-supac-ss-nonsterile-semisolid-dosage-forms-scale-up-and-post-approval-changes-chemistry-manufacturing-> (accessed 11.23.19).

Ferrer, J., 2000. Vaginal candidosis: epidemiological and etiological factors. *International Journal of Gynecology & Obstetrics* 71, 21–27. [https://doi.org/10.1016/S0020-7292\(00\)00350-7](https://doi.org/10.1016/S0020-7292(00)00350-7)

Fouda, M.M.G., Abdel-Mohsen, A.M., Ebaid, H., Hassan, I., Al-Tamimi, J., Abdel-Rahman, R.M., Metwalli, A., Alhazza, I., Rady, A., El-Faham, A., Jancar, J., 2016. Wound healing of different molecular weight of hyaluronan; in-vivo study. *Int. J. Biol. Macromol.* 89, 582–591. <https://doi.org/10.1016/j.ijbiomac.2016.05.021>

Foxman, B., Muraglia, R., Dietz, J.-P., Sobel, J.D., Wagner, J., 2013. Prevalence of Recurrent Vulvovaginal Candidiasis in 5 European Countries and the United States: Results From an Internet Panel Survey. *Journal of Lower Genital Tract Disease* 17, 340–345.

<https://doi.org/10.1097/LGT.0b013e318273e8cf>

Frykberg, R.G., Banks, J., 2015. Challenges in the Treatment of Chronic Wounds. *Adv Wound Care (New Rochelle)* 4, 560–582. <https://doi.org/10.1089/wound.2015.0635>

Garcia-Bennett, A.E., 2011. Synthesis, toxicology and potential of ordered mesoporous materials in nanomedicine. *Nanomedicine* 6, 867–877. <https://doi.org/10.2217/nnm.11.82>

Garg, A., Aggarwal, D., Garg, S., Singla, A.K., 2002. Spreading of Semisolid Formulations An Update. *PHARMACEUTICAL TECHNOLOGY* 26, 84–105.

Geerligs, M., 2006. A literature review of the mechanical behavior of the stratum corneum, the living epidermis and the subcutaneous fat tissue. 2006, 39.

Gold, W.A., Williamson, S.L., Kaur, S., Hargreaves, I.P., Land, J.M., Pelka, G.J., Tam, P.P.L., Christodoulou, J., 2014. Mitochondrial dysfunction in the skeletal muscle of a mouse model of Rett syndrome (RTT): Implications for the disease phenotype. *Mitochondrion* 15, 10–17. <https://doi.org/10.1016/j.mito.2014.02.012>

Grada, A., Otero-Vinas, M., Prieto-Castrillo, F., Obagi, Z., Falanga, V., 2017. Research Techniques Made Simple: Analysis of Collective Cell Migration Using the Wound Healing Assay. *Journal of Investigative Dermatology* 137, e11–e16. <https://doi.org/10.1016/j.jid.2016.11.020>

Griffin, B.J., 2007. Variable pressure and environmental scanning electron microscopy: imaging of biological samples. *Methods Mol. Biol.* 369, 467–495. https://doi.org/10.1007/978-1-59745-294-6_23

Grinberg, V.Y., Senin, A.A., Grinberg, N.V., Burova, T.V., Dubovik, A.S., Potekhin, S.A., 2018. Energetics of poloxamer micellization at normal and high pressures. *Polymer* 138, 288–294. <https://doi.org/10.1016/j.polymer.2018.01.060>

Guo, S., Dipietro, L.A., 2010. Factors affecting wound healing. *J. Dent. Res.* 89, 219–229. <https://doi.org/10.1177/0022034509359125>

Gupta, M. (Ed.), 2020. *Novel drug delivery systems for phytoconstituents*. Taylor & Francis, Boca Raton.

Gupta, M., Agrawal, U., Vyas, S.P., 2012. Nanocarrier-based topical drug delivery for the treatment of skin diseases. *Expert Opinion on Drug Delivery* 9, 783–804. <https://doi.org/10.1517/17425247.2012.686490>

Haller, I., 1985. Mode of action of clotrimazole: Implications for therapy. *American Journal of Obstetrics and Gynecology* 152, 939–944. [https://doi.org/10.1016/S0002-9378\(85\)80005-3](https://doi.org/10.1016/S0002-9378(85)80005-3)

Handelman, G.J., Packer, L., Cross, C.E., 1996. Destruction of tocopherols, carotenoids, and retinol in human plasma by cigarette smoke. *The American Journal of Clinical Nutrition* 63, 559–565. <https://doi.org/10.1093/ajcn/63.4.559>

Haq, A., Goodyear, B., Ameen, D., Joshi, V., Michniak-Kohn, B., 2018. Strat-M® synthetic membrane: Permeability comparison to human cadaver skin. *International Journal of Pharmaceutics* 547, 432–437. <https://doi.org/10.1016/j.ijpharm.2018.06.012>

Hazama, Y., Maekawa, T., Miki, R., Oshima, S., Egawa, Y., Morimoto, K., Seki, T., 2016. Effect of Physiological Changes in the Skin on Systemic Absorption of Tacrolimus Following Topical Application in Rats. *Biological & Pharmaceutical Bulletin* 39, 343–352. <https://doi.org/10.1248/bpb.b15-00727>

Heng, M.C.Y., 2011. Wound healing in adult skin: aiming for perfect regeneration. *Int. J.*

Dermatol. 50, 1058–1066. <https://doi.org/10.1111/j.1365-4632.2011.04940.x>

Holzer, G., Riegler, E., Hönigsmann, H., Farokhnia, S., Schmidt, B., 2005. Effects and side-effects of 2% progesterone cream on the skin of peri- and postmenopausal women: results from a double-blind, vehicle-controlled, randomized study: Effects of progesterone cream on the skin. *British Journal of Dermatology* 153, 626–634. <https://doi.org/10.1111/j.1365-2133.2005.06685.x>

Hu, S.S., Neff, L., Agaku, I.T., Cox, S., Day, H.R., Holder-Hayes, E., King, B.A., 2016. Tobacco Product Use Among Adults — United States, 2013–2014. *MMWR Morb. Mortal. Wkly. Rep.* 65, 685–691. <https://doi.org/10.15585/mmwr.mm6527a1>

Iqbal, M.A., Md, S., Sahni, J.K., Baboota, S., Dang, S., Ali, J., 2012. Nanostructured lipid carriers system: Recent advances in drug delivery. *Journal of Drug Targeting* 20, 813–830. <https://doi.org/10.3109/1061186X.2012.716845>

Iqbal, Z., Dilnawaz, F., 2019. Nanocarriers For Vaginal Drug Delivery. *DDF* 13, 3–15. <https://doi.org/10.2174/1872211313666190215141507>

Jahn, B., Martin, E., Stueben, A., Bhakdi, S., 1995. Susceptibility testing of *Candida albicans* and *Aspergillus* species by a simple microtiter menadione-augmented 3-(4,5-dimethyl-2-thiazolyl)-2,5-diphenyl-2H-tetrazolium bromide assay. *J. Clin. Microbiol.* 33, 661–667.

Jenning, V., Thünemann, A.F., Gohla, S.H., 2000. Characterisation of a novel solid lipid nanoparticle carrier system based on binary mixtures of liquid and solid lipids. *International Journal of Pharmaceutics* 199, 167–177. [https://doi.org/10.1016/S0378-5173\(00\)00378-1](https://doi.org/10.1016/S0378-5173(00)00378-1)

Jores, K., Mehnert, W., Drechsler, M., Bunjes, H., Johann, C., Mäder, K., 2004. Investigations on the structure of solid lipid nanoparticles (SLN) and oil-loaded solid lipid nanoparticles by photon correlation spectroscopy, field-flow fractionation and transmission electron microscopy. *Journal of Controlled Release* 95, 217–227. <https://doi.org/10.1016/j.jconrel.2003.11.012>

Jung, Y., Park, W., Park, H., Lee, D.-K., Na, K., 2017. Thermo-sensitive injectable hydrogel based on the physical mixing of hyaluronic acid and Pluronic F-127 for sustained NSAID delivery. *Carbohydrate Polymers* 156, 403–408. <https://doi.org/10.1016/j.carbpol.2016.08.068>

Takehi, K., Kinoshita, M., Yasueda, S., 2003. Hyaluronic acid: separation and biological implications. *J. Chromatogr. B Analyt. Technol. Biomed. Life Sci.* 797, 347–355. [https://doi.org/10.1016/s1570-0232\(03\)00479-3](https://doi.org/10.1016/s1570-0232(03)00479-3)

Kapoor, M.S., GuhaSarkar, S., Banerjee, R., 2017. Stratum corneum modulation by chemical enhancers and lipid nanostructures: implications for transdermal drug delivery. *Therapeutic Delivery* 8, 701–718. <https://doi.org/10.4155/tde-2017-0045>

Karadzovska, D., Brooks, J.D., Monteiro-Riviere, N.A., Riviere, J.E., 2013. Predicting skin permeability from complex vehicles. *Advanced Drug Delivery Reviews* 65, 265–277. <https://doi.org/10.1016/j.addr.2012.01.019>

Karadzovska, D., Riviere, J.E., 2013. Assessing vehicle effects on skin absorption using artificial membrane assays. *European Journal of Pharmaceutical Sciences* 50, 569–576. <https://doi.org/10.1016/j.ejps.2013.02.020>

Kennedy, C., Bastiaens, M.T., Willemze, R., Bouwes Bavinck, J.N., Bajdik, C.D., Westendorp, R.G.J., 2003. Effect of Smoking and Sun on the Aging Skin. *Journal of Investigative Dermatology* 120, 548–554. <https://doi.org/10.1046/j.1523-1747.2003.12092.x>

- Khurana, S., Bedi, P.M.S., Jain, N.K., 2013. Preparation and evaluation of solid lipid nanoparticles based nanogel for dermal delivery of meloxicam. *Chemistry and Physics of Lipids* 175–176, 65–72. <https://doi.org/10.1016/j.chemphyslip.2013.07.010>
- Kim, K.E., Cho, D., Park, H.J., 2016. Air pollution and skin diseases: Adverse effects of airborne particulate matter on various skin diseases. *Life Sciences* 152, 126–134. <https://doi.org/10.1016/j.lfs.2016.03.039>
- Koffi, A.A., Agnely, F., Ponchel, G., Grossiord, J.L., 2006. Modulation of the rheological and mucoadhesive properties of thermosensitive poloxamer-based hydrogels intended for the rectal administration of quinine. *European Journal of Pharmaceutical Sciences* 27, 328–335. <https://doi.org/10.1016/j.ejps.2005.11.001>
- Krutmann, J., Bouloc, A., Sore, G., Bernard, B.A., Passeron, T., 2017. The skin aging exposome. *Journal of Dermatological Science* 85, 152–161. <https://doi.org/10.1016/j.jdermsci.2016.09.015>
- Küchler, S., Radowski, M.R., Blaschke, T., Dathe, M., Plendl, J., Haag, R., Schäfer-Korting, M., Kramer, K.D., 2009. Nanoparticles for skin penetration enhancement – A comparison of a dendritic core-multishell-nanotransporter and solid lipid nanoparticles. *European Journal of Pharmaceutics and Biopharmaceutics* 71, 243–250. <https://doi.org/10.1016/j.ejpb.2008.08.019>
- Kulkarni, C.V., 2012. Lipid crystallization: from self-assembly to hierarchical and biological ordering. *Nanoscale* 4, 5779. <https://doi.org/10.1039/c2nr31465g>
- Kyle, A.A., Dahl, M.V., 2004. Topical Therapy for Fungal Infections: *American Journal of Clinical Dermatology* 5, 443–451. <https://doi.org/10.2165/00128071-200405060-00009>
- Leonardi, G., Falzone, L., Salemi, R., Zanghì, A., Spandidos, D., Mccubrey, J., Candido, S., Libra, M., 2018. Cutaneous melanoma: From pathogenesis to therapy (Review). *Int J Oncol*. <https://doi.org/10.3892/ijo.2018.4287>
- Lin, 2010. Gallic acid induces apoptosis in A375.S2 human melanoma cells through caspase-dependent and -independent pathways. *Int J Oncol* 37. https://doi.org/10.3892/ijo_00000686
- Lind, H., Jonsson, H., Schnürer, J., 2005. Antifungal effect of dairy propionibacteria—contribution of organic acids. *International Journal of Food Microbiology* 98, 157–165. <https://doi.org/10.1016/j.ijfoodmicro.2004.05.020>
- Lippacher, A., Müller, R.H., Mäder, K., 2002. Semisolid SLNTM dispersions for topical application: influence of formulation and production parameters on viscoelastic properties. *European Journal of Pharmaceutics and Biopharmaceutics* 53, 155–160. [https://doi.org/10.1016/S0939-6411\(01\)00233-8](https://doi.org/10.1016/S0939-6411(01)00233-8)
- Lockwood, G., Griesinger, G., Cometti, B., 13 European Centers, 2014. Subcutaneous progesterone versus vaginal progesterone gel for luteal phase support in in vitro fertilization: a noninferiority randomized controlled study. *Fertil. Steril.* 101, 112–119.e3. <https://doi.org/10.1016/j.fertnstert.2013.09.010>
- Luzzati, V., Delacroix, H., Gulik, A., Gulik-Krzywicki, T., Mariani, P., Vargas, R., 1997. Chapter 1 The Cubic Phases of Lipids, in: *Current Topics in Membranes*. Elsevier, pp. 3–24. [https://doi.org/10.1016/S0070-2161\(08\)60205-1](https://doi.org/10.1016/S0070-2161(08)60205-1)
- MacGregor, J.L., Maibach, H.I., 2002. The Specificity of Retinoid-Induced Irritation and Its Role in Clinical Efficacy. *Exog Dermatol* 1, 68–73. <https://doi.org/10.1159/000058335>
- Magnani, C., Isaac, V.L.B., Correa, M.A., Salgado, H.R.N., 2014. Caffeic acid: a review of its potential use in medications and cosmetics. *Anal. Methods* 6, 3203–3210.

<https://doi.org/10.1039/C3AY41807C>

Martin, P., Nunan, R., 2015. Cellular and molecular mechanisms of repair in acute and chronic wound healing. *Br. J. Dermatol.* 173, 370–378. <https://doi.org/10.1111/bjd.13954>

Masotta, N.E., Martinefski, M.R., Lucangioli, S., Rojas, A.M., Tripodi, V.P., 2019. High-dose coenzyme Q10-loaded oleogels for oral therapeutic supplementation. *International Journal of Pharmaceutics* 556, 9–20. <https://doi.org/10.1016/j.ijpharm.2018.12.003>

Mayol, L., Quaglia, F., Borzacchiello, A., Ambrosio, L., Rotonda, M., 2008. A novel poloxamers/hyaluronic acid in situ forming hydrogel for drug delivery: Rheological, mucoadhesive and in vitro release properties. *European Journal of Pharmaceutics and Biopharmaceutics* 70, 199–206. <https://doi.org/10.1016/j.ejpb.2008.04.025>

Mistry, N., 2017. Guidelines for Formulating Anti-Pollution Products. *Cosmetics* 4, 57. <https://doi.org/10.3390/cosmetics4040057>

Mukaremera, L., Lee, K.K., Mora-Montes, H.M., Gow, N.A.R., 2017. Candida albicans Yeast, Pseudohyphal, and Hyphal Morphogenesis Differentially Affects Immune Recognition. *Front Immunol* 8, 629. <https://doi.org/10.3389/fimmu.2017.00629>

Müller, R.H., Mäder, K., Gohla, S., 2000. Solid lipid nanoparticles (SLN) for controlled drug delivery – a review of the state of the art. *European Journal of Pharmaceutics and Biopharmaceutics* 50, 161–177. [https://doi.org/10.1016/S0939-6411\(00\)00087-4](https://doi.org/10.1016/S0939-6411(00)00087-4)

Muresan, Ximena M., Sticozzi, C., Belmonte, G., Cervellati, F., Ferrara, F., Lila, M.A., Valacchi, G., 2018a. SR-B1 involvement in keratinocytes in vitro wound closure. *Archives of Biochemistry and Biophysics* 658, 1–6. <https://doi.org/10.1016/j.abb.2018.09.014>

Muresan, Ximena M., Sticozzi, C., Belmonte, G., Cervellati, F., Ferrara, F., Lila, M.A., Valacchi, G., 2018b. SR-B1 involvement in keratinocytes in vitro wound closure. *Archives of Biochemistry and Biophysics* 658, 1–6. <https://doi.org/10.1016/j.abb.2018.09.014>

Muresan, Ximena Maria, Sticozzi, C., Belmonte, G., Savelli, V., Evelson, P., Valacchi, G., 2018. Modulation of cutaneous scavenger receptor B1 levels by exogenous stressors impairs “in vitro” wound closure. *Mechanisms of Ageing and Development* 172, 78–85. <https://doi.org/10.1016/j.mad.2017.11.006>

Murgia, S., Falchi, A.M., Mano, M., Lampis, S., Angius, R., Carnerup, A.M., Schmidt, J., Diaz, G., Giacca, M., Talmon, Y., Monduzzi, M., 2010. Nanoparticles from Lipid-Based Liquid Crystals: Emulsifier Influence on Morphology and Cytotoxicity. *J. Phys. Chem. B* 114, 3518–3525. <https://doi.org/10.1021/jp9098655>

Nastruzzi, C. (Ed.), 2005. *Lipospheres in drug targets and delivery: approaches, methods, and applications*. CRC Press, Boca Raton.

Ng, S.-F., Rouse, J., Sanderson, D., Eccleston, G., 2010a. A Comparative Study of Transmembrane Diffusion and Permeation of Ibuprofen across Synthetic Membranes Using Franz Diffusion Cells. *Pharmaceutics* 2, 209–223. <https://doi.org/10.3390/pharmaceutics2020209>

Ng, S.-F., Rouse, J.J., Sanderson, F.D., Meidan, V., Eccleston, G.M., 2010b. Validation of a Static Franz Diffusion Cell System for In Vitro Permeation Studies. *AAPS PharmSciTech* 11, 1432–1441. <https://doi.org/10.1208/s12249-010-9522-9>

Noverr, M.C., Huffnagle, G.B., 2004. Regulation of Candida albicans morphogenesis by fatty acid metabolites. *Infect. Immun.* 72, 6206–6210. <https://doi.org/10.1128/IAI.72.11.6206-6210.2004>

Oh, K.T., Bronich, T.K., Kabanov, A.V., 2004. Micellar formulations for drug delivery based

- on mixtures of hydrophobic and hydrophilic Pluronic block copolymers. *J Control Release* 94, 411–422. <https://doi.org/10.1016/j.jconrel.2003.10.018>
- Onor, I.O., Stirling, D.L., Williams, S.R., Bediako, D., Borghol, A., Harris, M.B., Darensburg, T.B., Clay, S.D., Okpechi, S.C., Sarpong, D.F., 2017. Clinical Effects of Cigarette Smoking: Epidemiologic Impact and Review of Pharmacotherapy Options. *IJERPH* 14, 1147. <https://doi.org/10.3390/ijerph14101147>
- Paliwal, R., Babu, R.J., Palakurthi, S., 2014. Nanomedicine Scale-up Technologies: Feasibilities and Challenges. *AAPS PharmSciTech* 15, 1527–1534. <https://doi.org/10.1208/s12249-014-0177-9>
- Palmer, B., DeLouise, L., 2016. Nanoparticle-Enabled Transdermal Drug Delivery Systems for Enhanced Dose Control and Tissue Targeting. *Molecules* 21, 1719. <https://doi.org/10.3390/molecules21121719>
- Pardeike, J., Hommoss, A., Müller, R.H., 2009. Lipid nanoparticles (SLN, NLC) in cosmetic and pharmaceutical dermal products. *International Journal of Pharmaceutics* 366, 170–184. <https://doi.org/10.1016/j.ijpharm.2008.10.003>
- Pecora, R., 2000. Dynamic Light Scattering Measurement of Nanometer Particles in Liquids. *Journal of Nanoparticle Research* 2, 123–131. <https://doi.org/10.1023/A:1010067107182>
- Pecorelli, A., Cervellati, C., Cortelazzo, A., Cervellati, F., Sticozzi, C., Mirasole, C., Guerranti, R., Trentini, A., Zolla, L., Savelli, V., Hayek, J., Valacchi, G., 2016a. Proteomic analysis of 4-hydroxynonenal and nitrotyrosine modified proteins in RTT fibroblasts. *The International Journal of Biochemistry & Cell Biology* 81, 236–245. <https://doi.org/10.1016/j.biocel.2016.08.001>
- Pecorelli, A., Cervellati, C., Hayek, J., Valacchi, G., 2016b. OxInflammation in Rett syndrome. *The International Journal of Biochemistry & Cell Biology* 81, 246–253. <https://doi.org/10.1016/j.biocel.2016.07.015>
- Pecorelli, A., Cervellati, F., Belmonte, G., Montagner, G., Waldon, P., Hayek, J., Gambari, R., Valacchi, G., 2016c. Cytokines profile and peripheral blood mononuclear cells morphology in Rett and autistic patients. *Cytokine* 77, 180–188. <https://doi.org/10.1016/j.cyto.2015.10.002>
- Pecorelli, A., Ciccoli, L., Signorini, C., Leoncini, S., Giardini, A., D'Esposito, M., Filosa, S., Hayek, J., De Felice, C., Valacchi, G., 2011. Increased levels of 4HNE-protein plasma adducts in Rett syndrome. *Clinical Biochemistry* 44, 368–371. <https://doi.org/10.1016/j.clinbiochem.2011.01.007>
- Pelinson, L.P., Assmann, C.E., Palma, T.V., da Cruz, I.B.M., Pillat, M.M., Mânica, A., Stefanello, N., Weis, G.C.C., de Oliveira Alves, A., de Andrade, C.M., Ulrich, H., Morsch, V.M.M., Schetinger, M.R.C., Bagatini, M.D., 2019. Antiproliferative and apoptotic effects of caffeic acid on SK-Mel-28 human melanoma cancer cells. *Mol. Biol. Rep.* 46, 2085–2092. <https://doi.org/10.1007/s11033-019-04658-1>
- Pierard, G., Courtois, J., Ritacco, C., Humbert, P., Fanian, F., Piérard-Franchimont, C., 2015. From observational to analytical morphology of the stratum corneum: progress avoiding hazardous animal and human testings. *CCID* 113. <https://doi.org/10.2147/CCID.S77027>
- Pooja, D., Tunki, L., Kulhari, H., Reddy, B.B., Sistla, R., 2015. Characterization, biorecognitive activity and stability of WGA grafted lipid nanostructures for the controlled delivery of Rifampicin. *Chemistry and Physics of Lipids* 193, 11–17. <https://doi.org/10.1016/j.chemphyslip.2015.09.008>

- PubChem, n.d. Gallic acid [WWW Document]. URL <https://pubchem.ncbi.nlm.nih.gov/compound/370> (accessed 11.25.19).
- Puglia, C., Bonina, F., Rizza, L., Cortesi, R., Merlotti, E., Drechsler, M., Mariani, P., Contado, C., Ravani, L., Esposito, E., 2010. Evaluation of Percutaneous Absorption of Naproxen from Different Liposomal Formulations. *Journal of Pharmaceutical Sciences* 99, 2819–2829. <https://doi.org/10.1002/jps.22028>
- Ravani, L., Esposito, E., Bories, C., Moal, V.L.-L., Loiseau, P.M., Djabourov, M., Cortesi, R., Bouchemal, K., 2013. Clotrimazole-loaded nanostructured lipid carrier hydrogels: Thermal analysis and in vitro studies. *International Journal of Pharmaceutics, Targeted Drug Delivery* 454, 695–702. <https://doi.org/10.1016/j.ijpharm.2013.06.015>
- Rembiesa, J., Ruzgas, T., Engblom, J., Holfors, A., 2018. The Impact of Pollution on Skin and Proper Efficacy Testing for Anti-Pollution Claims. *Cosmetics* 5, 4. <https://doi.org/10.3390/cosmetics5010004>
- Rex, J.H., Clinical and Laboratory Standards Institute (Eds.), 2008. Reference method for broth dilution antifungal susceptibility testing of yeasts: approved standard, 3rd ed. ed, Documents / Clinical and Laboratory Standards Institute. National Committee for Clinical Laboratory Standards, Wayne, PA.
- Ricci, E.J., Lunardi, L.O., Nanclares, D.M.A., Marchetti, J.M., 2005. Sustained release of lidocaine from Poloxamer 407 gels. *International Journal of Pharmaceutics* 288, 235–244. <https://doi.org/10.1016/j.ijpharm.2004.09.028>
- Romanovsky, A.A., 2014. Skin temperature: its role in thermoregulation. *Acta Physiol* 210, 498–507. <https://doi.org/10.1111/apha.12231>
- Saez, V., Souza, I.D.L., Mansur, C.R.E., 2018. Lipid nanoparticles (SLN & NLC) for delivery of vitamin E: a comprehensive review. *Int J Cosmet Sci* 40, 103–116. <https://doi.org/10.1111/ics.12452>
- Saija, A., Tomaino, A., Proteggente, A., 1999. Ferulic and caffeic acids as potential protective agents against photooxidative skin damage. *J Sci Food Agric* 5.
- Sala, M., Diab, R., Elaissari, A., Fessi, H., 2018. Lipid nanocarriers as skin drug delivery systems: Properties, mechanisms of skin interactions and medical applications. *International Journal of Pharmaceutics* 535, 1–17. <https://doi.org/10.1016/j.ijpharm.2017.10.046>
- Salamanca, C., Barrera-Ocampo, A., Lasso, J., Camacho, N., Yarce, C., 2018. Franz Diffusion Cell Approach for Pre-Formulation Characterisation of Ketoprofen Semi-Solid Dosage Forms. *Pharmaceutics* 10, 148. <https://doi.org/10.3390/pharmaceutics10030148>
- Salwowska, N.M., Bebenek, K.A., Żądło, D.A., Wcisło-Dziadecka, D.L., 2016. Physicochemical properties and application of hyaluronic acid: a systematic review. *J Cosmet Dermatol* 15, 520–526. <https://doi.org/10.1111/jocd.12237>
- Santos, S.S., Lorenzoni, A., Ferreira, L.M., Mattiazzi, J., Adams, A.I.H., Denardi, L.B., Alves, S.H., Schaffazick, S.R., Cruz, L., 2013. Clotrimazole-loaded Eudragit® RS100 nanocapsules: Preparation, characterization and in vitro evaluation of antifungal activity against *Candida* species. *Materials Science and Engineering: C* 33, 1389–1394. <https://doi.org/10.1016/j.msec.2012.12.040>
- Sarkar, B., Ravi, V., Alexandridis, P., 2013. Micellization of amphiphilic block copolymers in binary and ternary solvent mixtures. *Journal of Colloid and Interface Science* 390, 137–146. <https://doi.org/10.1016/j.jcis.2012.09.028>
- Sguizzato, M., Valacchi, G., Pecorelli, A., Boldrini, P., Simelière, F., Huang, N., Cortesi, R.,

- Esposito, E., 2020. Gallic acid loaded poloxamer gel as new adjuvant strategy for melanoma: A preliminary study. *Colloids and Surfaces B: Biointerfaces* 185, 110613. <https://doi.org/10.1016/j.colsurfb.2019.110613>
- Sharma, A., Soliman, G.M., Al-Hajaj, N., Sharma, R., Maysinger, D., Kakkar, A., 2012. Design and Evaluation of Multifunctional Nanocarriers for Selective Delivery of Coenzyme Q10 to Mitochondria. *Biomacromolecules* 13, 239–252. <https://doi.org/10.1021/bm201538j>
- Shelke, S., Shahi, S., Jadhav, K., Dhamecha, D., Tiwari, R., Patil, H., 2016. Thermoreversible nanoethosomal gel for the intranasal delivery of Eletriptan hydrobromide. *J Mater Sci: Mater Med* 27, 103. <https://doi.org/10.1007/s10856-016-5713-6>
- Shidhaye, S.S., Vaidya, R., Sutar, S., Patwardhan, A., Kadam, V.J., 2008. Solid lipid nanoparticles and nanostructured lipid carriers--innovative generations of solid lipid carriers. *Curr Drug Deliv* 5, 324–331. <https://doi.org/10.2174/156720108785915087>
- Shubhra, Q.T.H., Tóth, J., Gyenis, J., Feczko, T., 2014. Poloxamers for Surface Modification of Hydrophobic Drug Carriers and Their Effects on Drug Delivery. *Polymer Reviews* 54, 112–138. <https://doi.org/10.1080/15583724.2013.862544>
- Siewert, M., Dressman, J., Brown, C.K., Shah, V.P., FIP, AAPS, 2003. FIP/AAPS guidelines to dissolution/in vitro release testing of novel/special dosage forms. *AAPS PharmSciTech* 4, E7. <https://doi.org/10.1208/pt040107>
- Simon, A., Amaro, M.I., Healy, A.M., Cabral, L.M., de Sousa, V.P., 2016. Comparative evaluation of rivastigmine permeation from a transdermal system in the Franz cell using synthetic membranes and pig ear skin with in vivo-in vitro correlation. *International Journal of Pharmaceutics* 512, 234–241. <https://doi.org/10.1016/j.ijpharm.2016.08.052>
- Sticozzi, C., Belmonte, G., Pecorelli, A., Cervellati, F., Leoncini, S., Signorini, C., Ciccoli, L., De Felice, C., Hayek, J., Valacchi, G., 2013. Scavenger receptor B1 post-translational modifications in Rett syndrome. *FEBS Letters* 587, 2199–2204. <https://doi.org/10.1016/j.febslet.2013.05.042>
- Stocks, D., Sundaram, H., Michaels, J., Durrani, M.J., Wortzman, M.S., Nelson, D.B., 2011. Rheological evaluation of the physical properties of hyaluronic acid dermal fillers. *J Drugs Dermatol* 10, 974–980.
- Ström, A., Larsson, A., Okay, O., 2015. Preparation and physical properties of hyaluronic acid-based cryogels. *J. Appl. Polym. Sci.* 132, n/a-n/a. <https://doi.org/10.1002/app.42194>
- Suehara, L.Y., Simone, K., Maia, M., 2006. Avaliação do envelhecimento facial relacionado ao tabagismo. *An. Bras. Dermatol.* 81, 34–39. <https://doi.org/10.1590/S0365-05962006000100004>
- Takahashi, M., Takahashi, K., 2019. Water-soluble CoQ10 as A Promising Anti-aging Agent for Neurological Dysfunction in Brain Mitochondria. *Antioxidants* 8, 61. <https://doi.org/10.3390/antiox8030061>
- Tapeinos, C., Battaglini, M., Ciofani, G., 2017. Advances in the design of solid lipid nanoparticles and nanostructured lipid carriers for targeting brain diseases. *J Control Release* 264, 306–332. <https://doi.org/10.1016/j.jconrel.2017.08.033>
- Tavaniotou, A., Smitz, J., Bourgain, C., Devroey, P., 2000. Comparison between different routes of progesterone administration as luteal phase support in infertility treatments. *Hum. Reprod. Update* 6, 139–148. <https://doi.org/10.1093/humupd/6.2.139>
- Teeranachaideekul, V., Souto, E.B., Müller, R.H., Junyaprasert, V.B., 2008. Physicochemical characterization and *in vitro* release studies of ascorbyl palmitate-loaded semi-solid nanostructured lipid carriers (NLC gels). *Journal of Microencapsulation*

25, 111–120. <https://doi.org/10.1080/02652040701817762>

Touitou, E., Dayan, N., Bergelson, L., Godin, B., Eliaz, M., 2000. Ethosomes — novel vesicular carriers for enhanced delivery: characterization and skin penetration properties. *Journal of Controlled Release* 65, 403–418. [https://doi.org/10.1016/S0168-3659\(99\)00222-9](https://doi.org/10.1016/S0168-3659(99)00222-9)

Touitou, E., Fabin, B., 1988. Altered skin permeation of a highly lipophilic molecule: tetrahydrocannabinol. *International Journal of Pharmaceutics* 43, 17–22. [https://doi.org/10.1016/0378-5173\(88\)90053-1](https://doi.org/10.1016/0378-5173(88)90053-1)

Uner, M., 2006. Preparation, characterization and physico-chemical properties of solid lipid nanoparticles (SLN) and nanostructured lipid carriers (NLC): their benefits as colloidal drug carrier systems. *Pharmazie* 61, 375–386.

Üner, M., Karaman, E., Aydoğmuş, Z., 2014. Solid Lipid Nanoparticles and Nanostructured Lipid Carriers of Loratadine for Topical Application: Physicochemical Stability and Drug Penetration through Rat Skin. *Trop. J. Pharm Res* 13, 653. <https://doi.org/10.4314/tjpr.v13i5.1>

Uner, M., Yener, G., 2007. Importance of solid lipid nanoparticles (SLN) in various administration routes and future perspectives. *Int J Nanomedicine* 2, 289–300.

Valacchi, G., Pecorelli, A., Belmonte, G., Pambianchi, E., Cervellati, F., Lynch, S., Krol, Y., Oresajo, C., 2017a. Protective Effects of Topical Vitamin C Compound Mixtures against Ozone-Induced Damage in Human Skin. *Journal of Investigative Dermatology* 137, 1373–1375. <https://doi.org/10.1016/j.jid.2017.01.034>

Valacchi, G., Pecorelli, A., Cervellati, C., Hayek, J., 2017b. 4-hydroxynonenal protein adducts: Key mediator in Rett syndrome oxinflammation. *Free Radical Biology and Medicine* 111, 270–280. <https://doi.org/10.1016/j.freeradbiomed.2016.12.045>

Valacchi, G., Pecorelli, A., Mencarelli, M., Carbotti, P., Fortino, V., Muscettola, M., Maioli, E., 2009. Rottlerin: a multifaced regulator of keratinocyte cell cycle. *Experimental Dermatology* 18, 516–521. <https://doi.org/10.1111/j.1600-0625.2008.00816.x>

Valacchi, G., Sticozzi, C., Belmonte, G., Cervellati, F., Demaude, J., Chen, N., Krol, Y., Oresajo, C., 2015. Vitamin C Compound Mixtures Prevent Ozone-Induced Oxidative Damage in Human Keratinocytes as Initial Assessment of Pollution Protection. *PLoS ONE* 10, e0131097. <https://doi.org/10.1371/journal.pone.0131097>

Vaz, S., Silva, R., Amaral, M.H., Martins, E., Sousa Lobo, J.M., Silva, A.C., 2019. Evaluation of the biocompatibility and skin hydration potential of vitamin E-loaded lipid nanosystems formulations: In vitro and human in vivo studies. *Colloids and Surfaces B: Biointerfaces* 179, 242–249. <https://doi.org/10.1016/j.colsurfb.2019.03.036>

Wells, J.I., 1988. *Pharmaceutical preformulation: the physicochemical properties of drug substances*, Ellis Horwood books in biological sciences. E. Horwood; Halsted Press, Chichester: New York.

Wissing, S., Lippacher, A., Müller, R., 2001. Investigations on the occlusive properties of solid lipid nanoparticles (SLN). *J Cosmet Sci* 52, 313–324.

Wissing, S.A., Müller, R.H., 2003. The influence of solid lipid nanoparticles on skin hydration and viscoelasticity—in vivo study. *Eur J Pharm Biopharm* 56, 67–72. [https://doi.org/10.1016/s0939-6411\(03\)00040-7](https://doi.org/10.1016/s0939-6411(03)00040-7)

Witczak, Z.J., 1997. *Polysaccharides in Medicinal Applications*. Edited by Severian Dumitriu, Marcel Dekker, Inc. New York, ISBN 0-8247-9540-7. 1996, 794 pp. \$195.00. *Journal of Carbohydrate Chemistry* 16, 245–247.

<https://doi.org/10.1080/07328309708006525>

Wolf, G., 2005. The Discovery of the Antioxidant Function of Vitamin E: the contribution of Henry A. Mattill. *The Journal of Nutrition* 135, 363–366. <https://doi.org/10.1093/jn/135.3.363>

Yalavarthi, P., Dudala, T., Mudumala, N., Pasupati, V., Thanniru, J., Vadlamudi, H., Yaga, G., 2014. A perspective overview on lipospheres as lipid carrier systems. *Int J Pharma Investig* 4, 149. <https://doi.org/10.4103/2230-973X.143112>

Yang, D., Moh, S., Son, D., You, S., Kinyua, A., Ko, C., Song, M., Yeo, J., Choi, Y.-H., Kim, K., 2016. Gallic Acid Promotes Wound Healing in Normal and Hyperglucidic Conditions. *Molecules* 21, 899. <https://doi.org/10.3390/molecules21070899>

Yu, G.-E., Deng, Y., Dalton, S., Wang, Q.-G., Attwood, D., Price, C., Booth, C., 1992. Micellisation and gelation of triblock copoly(oxyethylene/oxypropylene/oxyethylene), F127. *J. Chem. Soc., Faraday Trans.* 88, 2537–2544. <https://doi.org/10.1039/FT9928802537>

Yuan, H., Chen, J., Du, Y.-Z., Hu, F.-Q., Zeng, S., Zhao, H.-L., 2007. Studies on oral absorption of stearic acid SLN by a novel fluorometric method. *Colloids and Surfaces B: Biointerfaces* 58, 157–164. <https://doi.org/10.1016/j.colsurfb.2007.03.002>

Zhou, X., Hao, Y., Yuan, L., Pradhan, S., Shrestha, K., Pradhan, O., Liu, H., Li, W., 2018. Nano-formulations for transdermal drug delivery: A review. *Chinese Chemical Letters* 29, 1713–1724. <https://doi.org/10.1016/j.ccllet.2018.10.037>

Zhu, W., Filler, S.G., 2010. Interactions of *Candida albicans* with epithelial cells. *Cellular Microbiology* 12, 273–282. <https://doi.org/10.1111/j.1462-5822.2009.01412.x>